Observations and Modelling of Precipitation in the Southern Alps of New Zealand

by

Stephen John Stuart

A thesis
submitted to the Victoria University of Wellington
in fulfilment of the
requirements for the degree of
Master of Science
in Physical Geography.

Victoria University of Wellington
2011

Abstract

Precipitation in the central Southern Alps affects glaciation, river flows and key economic activities, yet there is still uncertainty about its spatial distribution and primary influences. Long-term and future patterns of New Zealand precipitation can be estimated by the HadRM3P regional climate model (RCM) — developed by the United Kingdom Met Office — but orographic rainfall in the steep and rugged topography of the Southern Alps is difficult to simulate accurately at the 30-km resolution of the RCM. To quantify empirical relationships, observations of surface rainfall were gathered from rain gauges covering a broad region of the South Island. In four transects of the Hokitika, Franz Josef and Haast regions, the mean annual precipitation maxima of objectively interpolated profiles are consistently located 7–11 km southeast of the New Zealand Alpine Fault. The magnitude and shape of the rainfall profile across the Southern Alps are strongly influenced by the 850-hPa wind direction to the north of the mountain range, as determined by comparing rain-gauge observations to wind vectors from NCEP/NCAR Reanalysis 1. The observed profile of orographically enhanced rainfall was incorporated into a trivariate spline in order to interpolate precipitation simulated by the RCM. This downscaling method significantly improved the RCM's estimates of mean annual rainfall at stations in the Southern Alps region from 1971 to 2000, and RCM projections of future rainfall in mountainous regions may be similarly refined via this technique. The improved understanding of the observed rainfall distribution in the Southern Alps, as gained from this analysis, has a range of other hydrological applications and is already being used in 'downstream' modelling of glaciers.

Acknowledgments

Contents

List of Figures

List of Tables

Symbols and abbreviations used in the text

ARC	Antarctic Research Centre
CliDB	National Climate Database
DEM	digital elevation model
EBM	energy-balance model
ECMWF	European Centre for Medium-Range Weather Forecasts
ENSO	El Niño Southern Oscillation
GCV	generalised cross validation
GCM	general circulation model
GPR	ground-penetrating radar
HadRM3P	a regional climate model developed by the Hadley Centre
LBC	lateral boundary condition
LGM	Last Glacial Maximum
NHD	National Hydrometric Database
NCAR	National Center for Atmospheric Research
NCEP	National Centers for Environmental Prediction
NIWA	National Institute of Water and Atmospheric Research
NOAA	National Oceanic and Atmospheric Administration
NWP	numerical weather prediction
NZLAM	New Zealand Limited Area Model
NZMG	New Zealand Map Grid
PISM	Parallel Ice Sheet Model
RCM	regional climate model
RMSE	root mean square error

UTC	Coordinated Universal Time
UKMO	United Kingdom Met Office
UM	Unified Model
VUW	Victoria University of Wellington
WRA	Water Resources Archive
WRF	Weather Research and Forecasting
$\text{Surf}_{\text{Obs.A}}$	Surface of interpolated observations of mean annual precipitation in the Southern Alps from 1971 to 2000
$\text{Surf}_{\text{Obs.BA}}$	Surface of mean annual precipitation in the Southern Alps, produced by Dr Brian Anderson of the ARC
$\text{Surf}_{\text{Obs.D}}$	Surface of interpolated observations of mean daily precipitation in the Southern Alps from 1971 to 2000
$\text{Surf}_{\text{Obs.D.NE}}$	Surface of interpolated observations of mean daily precipitation in the Southern Alps on northeasterly days from 1971 to 2000
$\text{Surf}_{\text{Obs.D.NW}}$	Surface of interpolated observations of mean daily precipitation in the Southern Alps on northwesterly days from 1971 to 2000
$\text{Surf}_{\text{Obs.D.SE}}$	Surface of interpolated observations of mean daily precipitation in the Southern Alps on southeasterly days from 1971 to 2000
$\text{Surf}_{\text{Obs.D.SW}}$	Surface of interpolated observations of mean daily precipitation in the Southern Alps on southwesterly days from 1971 to 2000
$\text{Surf}_{\text{Obs.TK.M}}$	Surface of mean annual measured precipitation in the Pukaki catchment from 1971 to 2000, produced by Kerr (2009)
$\text{Surf}_{\text{Obs.TK.T}}$	Surface of mean annual 'true' precipitation in the Pukaki catchment from 1971 to 2000, produced by Kerr (2009)
$\text{Surf}_{\text{Rcm.A.Ds}}$	Surface of mean annual precipitation in the Southern Alps from 1971 to 2000, simulated by the RCM and then

Chapter 1

Introduction

The Southern Alps are the most dominant topographic feature of New Zealand. These mountains strongly influence the South Island climate, and more precipitation falls here than in any other part of the country. This precipitation feeds glaciers and provides snow to ski fields. Rivers which flow from the Southern Alps generate almost half of New Zealand's electricity (Leyland and CAE 1998) and irrigate much of the South Island. Both the quantity and the distribution of precipitation in the Southern Alps are critical to key national industries such as energy, agriculture and tourism.

Observed changes in global climate during the last century are very likely to be at least partially due to anthropogenic emissions of greenhouse gases (Hegerl et al. 2007), and projected increases in the variability of precipitation have lead to regional concerns over water security (Kundzewicz et al. 2007). Scientists have developed sophisticated climate models in recent years, in an effort to improve our understanding of the physics that underlie such changes (Randall et al. 2007). Climate models can simulate the interaction of different atmospheric and oceanic processes at a range of spatial scales over both land and sea. One goal of present research is to accurately simulate and predict global and regional climatic variability.

Using an ensemble of general circulation models (GCMs), which simulate global climate, scientists have predicted further rises in global mean surface air temperature by the end of this century (Meehl et al. 2007). The amount of the projected increase is strongly related to the quantity of greenhouse

gases emitted by anthropogenic activity over the next few decades. Simulations run under the mid-range A1B emissions scenario have predicted a mean increase of 2.8 °C in global mean surface air temperature by 2100, relative to the period from 1980 to 1999 (Meehl et al. 2007). While such projections are only estimates, the use of GCMs has gained general acceptance among the scientific community as the most effective means of predicting future variations in global climate (Randall et al. 2007).

In the mid-latitudes, GCMs simulate a future poleward shift of the westerlies and primary storm tracks (Yin 2005). This is likely to increase rainfall in the southwest of the South Island of New Zealand and in the western Southern Alps, while reduced rainfall is expected in northeastern parts of the North Island (Christensen et al. 2007). However, precipitation in mountainous regions is not well represented by GCMs, partly due to their coarse representation of topography (Schmidli et al. 2006).

A regional climate model (RCM), nested within a GCM, provides a means of downscaling global climatic projections. This downscaling provides finer meteorological detail within a designated region of interest, usually measuring a few thousand kilometres in both length and breadth (Jones et al. 2004). To date, the main application of RCMs has been to estimate the likely impacts of global increases in greenhouse gases upon regional climates. HadRM3P is a regional climate model that has been developed by the United Kingdom Met Office (UKMO) (Jones et al. 2004). This model is currently being adapted by the National Institute of Water and Atmospheric Research (NIWA) for use in New Zealand (Drost et al. 2007). The NIWA RCM will be used to quantify potential changes to the New Zealand climate during the next century. It can also be used to drive models of other environmental processes, such as river flows, snow accumulation and glaciation.

The two strongest climatic influences upon the behaviour of glaciers are temperature and precipitation. Anderson and Mackintosh (2006) found temperature to be the dominant influence in the Southern Alps, but South Island glacial advance has also been linked to the higher levels of precipitation associated with increased westerly circulation (Hessell 1983; Hay and Fitzharris 1988; Fitzharris et al. 1992). High rates of accumulation and ablation make

Figure 1.1 A crevasse field on the upper regions of the Franz Josef Glacier in the Southern Alps. Photograph taken by S. Stuart in March 2009.

temperate maritime glaciers particularly sensitive to climatic fluctuations (Oerlemans 1997), and debris-free glaciers in the Southern Alps, such as the Franz Josef Glacier (Figure 1.1), are important indicators of climate change (Chinn 1996; Anderson et al. 2008). The accumulation and melt of glacial ice and snow also affect the water balance of downstream catchments in the South Island.

Researchers from the Antarctic Research Centre (ARC), based at the Victoria University of Wellington (VUW), aim to gain a greater understanding of the past, present and future behaviour of glaciers in New Zealand. Various glacial mass-balance and ice-flow models are in development, including an energy-balance model (EBM) of glaciers in the central Southern Alps (Anderson et al. 2010). A key motivation for the research in this thesis was to aid the coupling of NIWA's RCM to this EBM. Linking these two models will provide insight into New Zealand glacial processes and help scientists predict future changes to glacial volumes, runoff and water availability in South Island alpine catchments. ARC researchers also aim to link the EBM to an instance of the Parallel Ice Sheet Model (PISM) (Bueler et al. 2010), in order to simulate the flow and extent of glaciers in the Southern Alps during the last 40,000 years. The PISM requires a surface of precipitation across

the area being modelled. One of the results of this thesis was a surface of ob-
served mean annual precipitation in the central Southern Alps from 1971 to
2000, which was subsequently used to drive glacial simulations by the PISM
(Section 5.3.1).

The current horizontal resolution of NIWA's RCM is around 30 km, but
downstream environmental models often require meteorological data, such
as temperature and precipitation, at a much finer spatial resolution. For
example, the EBM operates on a grid which has a resolution of just over
100 m. Since air temperature has a strongly negative correlation with alti-
tude, mesoscale temperatures simulated by the RCM can be approximated
at smaller scales via a fine representation of topography, such as a high-
resolution digital elevation model (DEM) (Barry 2008).

Topography also strongly influences the spatial distribution of precipita-
tion in the Southern Alps. The upward forcing of saturated air by these high
mountains — described in more detail in Section 2.3.1 — produces extremely
steep rainfall gradients at the surface (Chinn 1979; Griffiths and McSaveney
1983; Henderson and Thompson 1999). However, the steep and rugged to-
pography of the Southern Alps is smoothed at the 30-km resolution of the
RCM, and this impairs the simulation of orographic precipitation at finer
spatial scales (Drost et al. 2007). A suitable method of downscaling the sim-
ulated precipitation needs to somehow incorporate orographic processes at a
scale below that of the RCM's 30-km grid.

Observations in highly elevated regions of the Southern Alps are sparse.
This makes it difficult to ascertain the actual distribution of rainfall in the
central Southern Alps, and hinders the development of downscaling tech-
niques. Previous research has shown that the direct correlation between local
topographic elevation and precipitation is not strong in this region (Wratt
et al. 2000), and employing a direct dependence upon elevation is not an
accurate method of downscaling rainfall in New Zealand (Tait et al. 2006).
However, a two-dimensional approach to the modelling of precipitation may
be appropriate in the Southern Alps, since the orographic forcing of air mov-
ing across the mountain range produces a distinctly shaped profile of rainfall
(Chinn 1979; Griffiths and McSaveney 1983; Henderson and Thompson 1999;
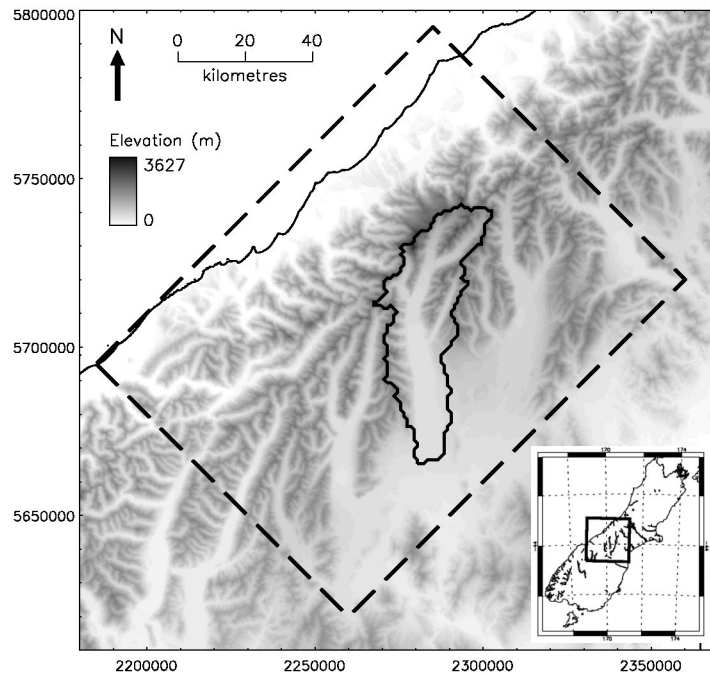
Figure 1.2 The topography of the central Southern Alps, as represented by a digital elevation model. The dashed line outlines the domain of the ARC energy-balance glacial model, which is the primary study region for this thesis. The Pukaki catchment is outlined by a thick solid line within the primary study region.

Wratt et al. 2000).

In this thesis, I ask the research question:

- What is the spatial distribution of precipitation in the central Southern Alps, and how is it influenced by topography and wind direction?

The domain of the ARC energy-balance model was designated the primary region of study (Figure 1.2). This is the most highly elevated and heavily glaciated region of New Zealand, and occupies approximately 14,000 km^2 of land. My objectives in this thesis are to:

1. derive profiles of historical rainfall across the Southern Alps, using observations from rain gauges;

2. identify the strongest influences upon the spatial distribution of precipitation in the central Southern Alps;

3. incorporate observed profiles of rainfall into the downscaling of precipitation simulated in the central Southern Alps by the NIWA regional climate model;

4. validate the simulated and downscaled precipitation by comparisons with observations of rainfall.

An improved correlation between observed and simulated precipitation, after downscaling, will help identify the primary determinants of rainfall distribution in the Southern Alps. In addition, the accurate simulation of historical climate instils greater confidence in future projections from both the RCM and other environmental models to which it is linked.

The next chapter describes the topography of the central Southern Alps, and reviews existing literature relating to orographic rainfall, dynamic atmospheric models and the estimation of precipitation. The observational data used in this thesis, including rain gauges in the Southern Alps and atmospheric properties from historical reanalyses, are described in Chapter 3. Many of these data have not been previously been included in such an analysis. Chapter 4 details the methods used to interpolate observations and downscale the simulated rainfall. The results of the analysis, including profiles and surfaces of observed and simulated precipitation, are presented in Chapter 5. These results are discussed within a wider research context in Chapter 6, before conclusions are presented in Chapter 7. Rain gauges in the Southern Alps from 1971 to 2000 are catalogued in Appendix A, and comparisons between individual rain gauges and the RCM are listed in Appendix B.

Chapter 2

Background

The predominantly westerly airflow of the mid-latitudes may be vertically displaced in the lower troposphere by local topographic variations, such as the steep mountains in the South Island of New Zealand. The orographically enhanced rainfall which arises from these effects has been studied in the Southern Alps and in a number of other mid-latitude mountain ranges around the world. The underlying physics of atmospheric motion and rainfall processes may be approximated by numerical equations, which are integrated in time within dynamic models. The distribution and influences of precipitation can also be modelled using interpolative and statistical techniques, in order to produce continuous rainfall surfaces, but empirical methods may be hindered in remote regions by a shortage of observational data. This chapter provides background information about alpine precipitation in the South Island, and documents previous work in related regions of study.

2.1 Topography of the central Southern Alps

The Southern Alps extend over 500 km along the west side of the South Island of New Zealand, with latitudes of 42–45° S and longitudes of 167–173° E. Figure 2.1 shows the South Island after a heavy blizzard in July 2003; the major mountain ranges are marked out by snow, though significant snow cover is also present in some catchments east of the mountains. The main orographic axis of the Southern Alps runs northeast-to-southwest, approxi-

Figure 2.1   The South Island of New Zealand after a heavy blizzard. Image taken on 11 Jul 2003 by the Moderate Resolution Imaging Spectroradiometer (MODIS), Terra Satellite, NASA.

mately parallel to the New Zealand Alpine Fault (Figure 2.2). The Southern Alps have formed at the boundary of the Pacific and Indo-Australian plates, where oblique convergence has caused tectonic uplift during the last 5–6 million years (Walcott 1998; Batt et al. 2000). The Main Divide of the Southern Alps generally lies 15–30 km southeast of the Alpine Fault. The Southern Alps culminate at Aoraki Mount Cook (3754 m, 43.6° S), which lies just south of the Main Divide. Mount Tasman (3491 m) is 4 km north of Aoraki and many other peaks also exceed 2500 m. Aoraki Mount Cook National Park and Tai Poutini Westland National Park occupy the most highly elevated region of the central Southern Alps, which contains all but one of New Zealand's peaks higher than 3000 m a.s.l.

Southwest of Aoraki, toward Haast, the Main Divide deviates further southeast of the Alpine Fault and reduces in height. Northwest of the Main Divide in this region, the Hooker Range lies on the northwest flank of the
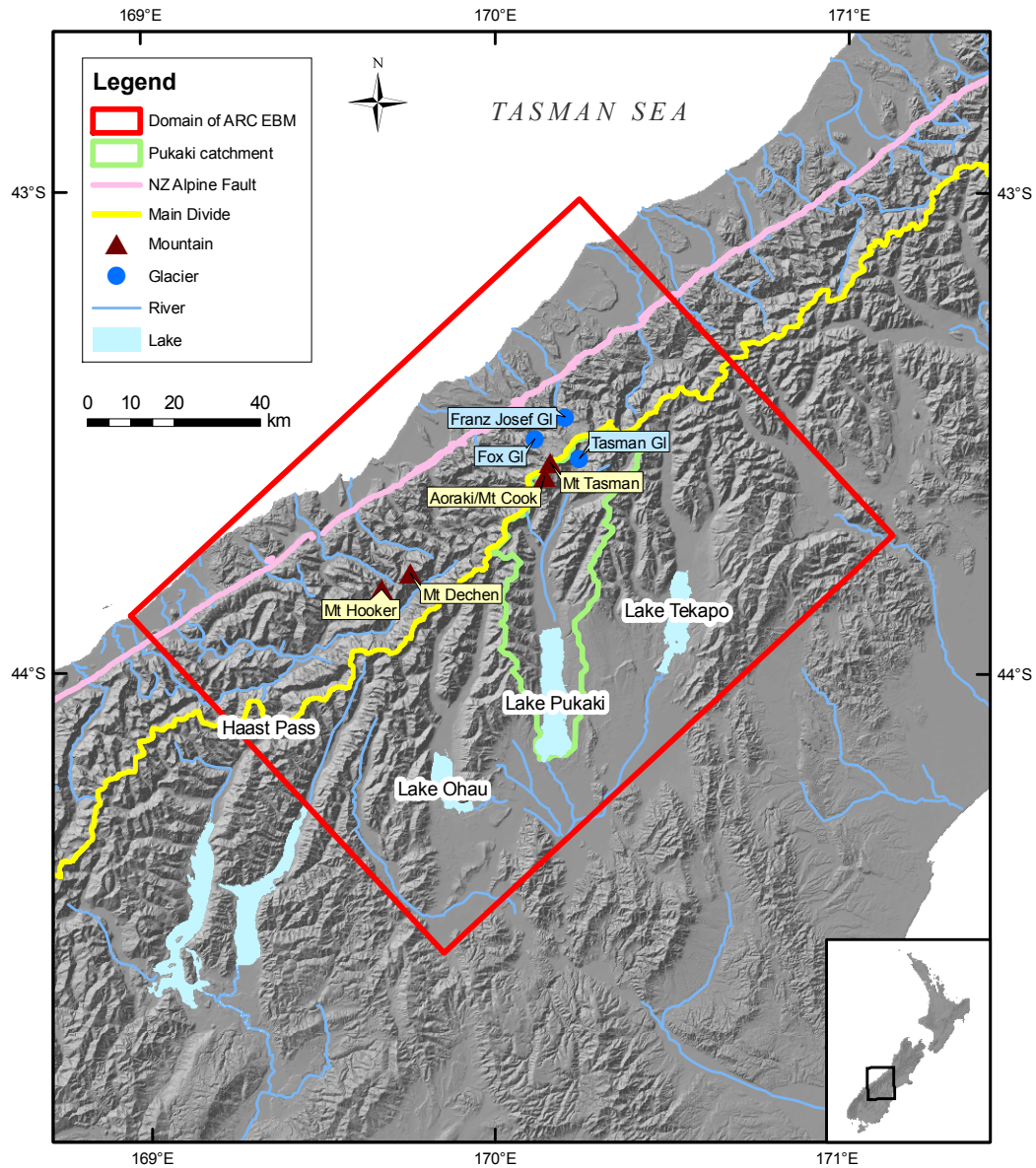
Figure 2.2 The topography of the central Southern Alps. Also shown on this map are the New Zealand Alpine Fault, the Main Divide, the domain of the ARC energy-balance glacial model, the Pukaki catchment and other geographic features mentioned in the text.

Landsborough Valley. This range contains significant peaks such as Mount Hooker (2640 m) and Mount Dechen (2643 m).

Glacial erosion has carved steep troughs and valleys through the landscape during multiple glaciations since the late Pleistocene (Suggate 1990), and the Southern Alps currently contain over 3000 glaciers (Chinn 1995). The Fox and Franz Josef glaciers are located on the western slopes north of Aoraki Mount Cook. The length of the Franz Josef Glacier is around 11 km and its elevation ranges from 2900 m a.s.l. near the Main Divide (Anderson et al. 2008) to less than 300 m a.s.l. at the glacial terminus. The upper regions of the glacier consist of wide, shallow snowfields which funnel down through the valley, in a northwest direction, to the steep tongue. The Franz Josef Glacier drains into the Waiho River in the Waiho Valley.

The Pukaki catchment lies southeast of the Main Divide in the Aoraki Mount Cook region, and has an area of 1359 km^2. The upper catchment contains 133 glaciers (Chinn 2001), including the largest glacier in New Zealand — the Tasman Glacier — which is currently 23 km long (Dykes and Brook 2010). Tasman Saddle is located in the upper regions of the glacier at an altitude of 2435 m a.s.l. The glacial tongue extends southwest into the Tasman Valley, where a proglacial lake drains into the Tasman River. This river flows south into Lake Pukaki, which covers an area of 168 km^2. Other large glaciers in the Pukaki catchment include the Murchison, Hooker and Mueller. The Ben Ohau and Sealy ranges form the steep west flank of the catchment, and the Jollie River flows through a subcatchment to the east. East of the Pukaki catchment, the Godley and Macaulay rivers flow into Lake Tekapo. Southwest of the Pukaki catchment, the Dobson and Hopkins rivers feed Lake Ohau.

2.2   Formation of precipitation

In this section, the basic physical processes that lead to precipitation are described. The two major constituent gases of the homosphere are nitrogen and oxygen; these gases are well mixed within the homosphere. The atmospheric concentration of water vapour, however, is variable, since cooler air has a

reduced capacity to hold water vapour in its gaseous state. Water vapour constitutes up to 4% of the volume of the homosphere (Sturman and Tapper 2006).

Within the troposphere, the pressure of air decreases logarithmically with height, as the accumulated weight of the compressed atmosphere decreases. This reduction in atmospheric pressure causes the temperature of air to also decrease with height — as air rises, it decompresses and becomes cooler (Barry and Chorley 2003). Rising air cools at the dry adiabatic lapse rate of 9.8 °C km^{-1} if no condensation of water takes place. Given a sufficient increase in altitude, rising moist air will eventually cool to the extent that its water vapour condenses to become particles of liquid water or ice (Barry and Chorley 2003).

If condensation of water vapour does occur, then latent heat is released. This latent heat partially counters the cooling of the rising air, causing the temperature of the air to decrease at a lower rate. This reduced rate is the saturated adiabatic lapse rate, which is usually 4–7 °C km^{-1} (Wallace and Hobbs 2006). If condensation continues, then cloud may form. Once the droplets or ice particles reach a certain size, the weight of their mass is sufficient to counter the upward force caused by the vertical pressure gradient. The water particles are then no longer in hydrostatic balance and gravity forces them to fall down toward the Earth as hydrometeors.

As the hydrometeors fall downward, the ambient atmospheric temperature usually rises, which may cause them to evaporate. Water droplets or ice particles that fall at least 100 m below the cloud base are regarded as precipitation (Sturman and Tapper 2006). If the precipitation lands in the phase of liquid water, then rain occurs. The presence of ice in the hydrometeors results in the precipitation falling in the form of snow, sleet or hail.

Precipitation is typically caused by some form of upward atmospheric motion. The three main drivers of upward atmospheric motion that leads to precipitation are convection, cyclonic lifting and orographic forcing. Convection is caused by the thermodynamic transfer of heat within the atmosphere, resulting in the vertical movement of air parcels. Convective precipitation can occur when a warm surface heats the lower troposphere and destabilises

the atmosphere, or within tropical cyclones as warm air rises near the centre of the depression.

Cyclonic precipitation forms as air is forced upward by the convergence of air masses in a region of low pressure. Along warm and cold fronts in the mid-latitudes, this causes the uplift of the warmer and more buoyant of the two air masses (Barry and Chorley 2003).

Orographic precipitation occurs as moist air travelling horizontally is forced upward by mountains. The amount of orographic precipitation that is experienced by a particular point on land is influenced by a number of factors. These include the humidity and temperature of the atmosphere upwind of the mountains (Wratt et al. 2000). Warmer air can hold more precipitable water, and a steep environmental lapse rate leads to atmospheric instability and more vigorous vertical movement of air parcels. A steep horizontal pressure gradient is associated with an increase in horizontal wind speed, leading to enhanced orographic uplift of air. The slope and height of the topography affect the rate and extent of atmospheric ascent. Land exposed to the direction of the wind is likely to receive more orographic precipitation (Barry 2008).

2.3   Precipitation in mountainous regions

2.3.1   Southern Alps of New Zealand

The Southern Alps lie on the northern edge of the zone of mid-latitude westerlies, which predominate between the subtropic belt of high pressure to the north and the polar trough to the south (Sturman and Tapper 2006). The proximity of the Southern Alps to the west coast of the South Island exposes these mountains to weather systems approaching from the Tasman Sea (Figures 2.3 and 5.21). The combination of westerly winds, moist oceanic air and orographic forcing typically causes annual precipitation on the upper west flank of the Southern Alps to exceed 10 m (Henderson and Thompson 1999). Lee side warming regularly causes a föhn effect over the eastern plains of the South Island, where precipitation drops to around 0.5 m a^{-1}.
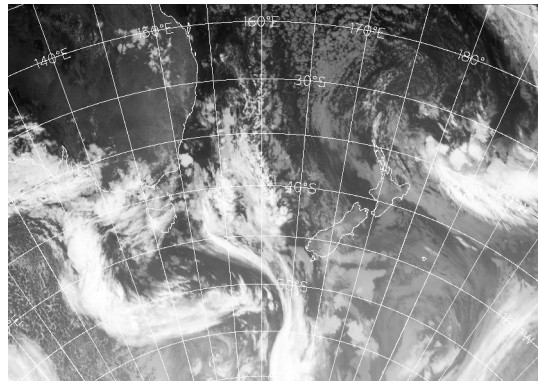
Figure 2.3 A front approaches New Zealand from the Tasman Sea on 21 Aug 2009. Image taken by the MTSAT-1R satellite and provided courtesy of the Japanese Meteorological Agency, the New Zealand Meteorological Service and MetVUW.com.

The observed distribution of precipitation exhibits a distinct profile across the Southern Alps (Chinn 1979; Griffiths and McSaveney 1983; Henderson 1993; Henderson and Thompson 1999), though the direct correlation between elevation and precipitation is not strong (Wratt et al. 2000). Henderson and Thompson (1999) analysed observations from rain gauges, which were arranged into four transects across the Southern Alps. They concluded that storm rainfall along the Southern Alps peaks within a slender zone, approximately 10 km southeast of the Alpine Fault and 10–20 km northwest of the highest ground. Additionally, across each section of the Southern Alps, the magnitude of the precipitation maxima and the height of the Main Divide showed some correlation (Henderson and Thompson 1999).

The Main Divide is not always the line of maximum elevation in the Southern Alps; subranges form the major windward barrier along some sections. At and around Aoraki Mount Cook, however, the Main Divide is at its highest and is also only around 30 km southeast of the western coastline, with little intervening topography. Precipitation in the Southern Alps may peak just upwind of the Main Divide in the vicinity of Aoraki Mount Cook (Griffiths and McSaveney 1983; Henderson and Thompson 1999).

The Franz Josef Glacier lies 13 km to the northeast of Aoraki Mount Cook and less than 20 km from the western coastline. The upper catchment of the glacier experiences up to 12 m of precipitation each year (Anderson

et al. 2008). However, it is difficult to maintain observational instruments
at high altitude in such steep and icy terrain, and in such a harsh climate.
A shortage of observations at high elevation makes it difficult to ascertain
whether mean annual precipitation does indeed peak in this region.

Precipitation in the Southern Alps is particularly intense during north-
westerly storms (Chinn 1979). Air from lower latitudes tends to be warmer
and therefore can usually hold more moisture. Warm air to the northwest of
New Zealand often becomes saturated as it travels southeastward over the
Tasman Sea. Moreover, northwesterly airflow approaches the Southern Alps
at an angle perpendicular to their axis, which enhances orographic uplift
(Chater and Sturman 1998; Wratt et al. 2000).

The influence of atmospheric variables upon the distribution of precipi-
tation in the Southern Alps has been investigated in a number of previous
studies, such as the Southern Alps Experiment (SALPEX) (Wratt et al. 1996;
Sinclair et al. 1997; Wratt et al. 2000), Chater and Sturman (1998) and Kerr
(2009). Among the atmospheric properties analysed in these studies were
wind direction, wind magnitude, temperature and humidity, at various alti-
tudes of the atmosphere. Wratt et al. (2000) constrained their analysis of the
relationship between air mass properties and rainfall in the Southern Alps
to times at which wind direction, in the horizontal plane and at the 850 hPa
pressure level, blew from between the bearings of 245° and 25°, that is, from
a northwestern segment of the compass. The average height of the 850 hPa
pressure level is around 1460 m a.s.l (NOAA et al. 1976), though the actual
height depends upon the current atmospheric temperature and pressure. Air
that displays a strong vertical temperature gradient upwind of the Southern
Alps is more easily destabilised as it encounters the first windward ranges,
encouraging upward motion (Wratt et al. 2000).

Sinclair et al. (1997) studied a long, intense northwesterly storm in the
Southern Alps from 4 to 9 November 1994. This was nicknamed the 'Guy
Fawkes storm', in recognition of the anniversary of the 'Gunpowder plot' to
blow up the English House of Lords on 5 November 1605. As this storm pro-
gressed, the profile of precipitation moved southeastward across the moun-
tains. A comparison to rawinsonde observations indicated that this move-

ment was associated with stronger wind speeds and a reduction in atmospheric stability during the latter periods of the storm (Sinclair et al. 1997).

Precipitation that falls east of the Main Divide during westerlies and northwesterlies is often termed 'spillover'. Past studies have noted a negative — though not always strong — correlation between air temperature and spillover (Sinclair et al. 1997; Chater and Sturman 1998; Wratt et al. 2000). Cool air is often associated with a reduction in the height of the freezing level, which can increase the amount of ice in the lower atmosphere. As hydrometeors, ice crystals fall more slowly than raindrops and thus travel further downwind, leading to more precipitation east of the Main Divide (Wratt et al. 1996; Sinclair et al. 1997; Chater and Sturman 1998; Wratt et al. 2000). Additionally, cool air masses can be destabilised by surface heating, which in turn reduces the blocking effect of the mountains and leads to increased spillover of precipitation. Kerr (2009) found that the distribution of precipitation in the Pukaki catchment was most strongly affected by distance from the axis of maximum orographic uplift and synoptic wind direction.

Annually, snowfall forms only 10–20% of the precipitation in the Southern Alps (Barry 2008), though this proportion increases during winter and early spring. Overall volumes of precipitation in the vicinity of the Main Divide show relatively little seasonal or annual variation (Hessell 1982; Henderson and Thompson 1999), but are influenced by changes in synoptic circulation. Annual precipitation in the south and west of the South Island correlates positively with the Trenberth (1976) Z1 index of westerly flow (Salinger 1982). The correlation between seasonal precipitation in the southwest South Island and the Southern Annular Mode (SAM) index is negative during summer and positive during winter (Kidston et al. 2009). During the El Niño (negative) phase of the El Niño Southern Oscillation (ENSO), cooler sea surface temperatures in the west Pacific introduce anomalous southwesterly airflow to New Zealand. This leads to cooler temperatures and a seasonally varying effect upon precipitation in the south and west of the South Island (Gordon 1986). The advance of reactive glaciers in the Southern Alps, such as the Franz Josef Glacier, is negatively correlated with the Southern Oscillation Index (SOI) and positively correlated with westerly circulation (Fitzharris

et al. 1992, 1997; Hooker and Fitzharris 1999).

2.3.2   International studies of orographic precipitation

Climatic conditions similar to those of the Southern Alps are to some extent encountered in other mountain ranges that also trend north-to-south and intersect the westerlies. Such ranges include the Patagonian Andes, the Scandinavian Mountains, and the Cascade Range and Sierra Nevada in the United States. The European Alps differ from these other ranges in some aspects of geography, but they have been the subject of much research into processes of orographic precipitation.

The Patagonian Andes are aligned approximately north-to-south, lie in the southern mid-latitude westerlies and are exposed on their windward side to the Pacific Ocean. High precipitation rates and the low temperatures associated with high latitudes and topographic elevation lead to significant glacierization in the Patagonian icefields. Fujiyoshi et al. (1987) studied precipitation over San Rafael Glacier in Chile, at around 47° S. At the glacial terminus, which lies at sea level on the western coastline, mean annual rainfall over 4 years was 3.7 m a^{-1}. From 5 months of observations during the austral summer, Fujiyoshi et al. (1987) estimated that in the middle of the Northern Patagonia Icefield, 12 km east of the San Rafael terminus and at an altitude of 640 m a.s.l., mean annual precipitation was around 10 m a^{-1}. To the south, Schneider et al. (2003) analysed 3 years of observations of precipitation across a mountainous section of the Patagonian archipelago at 53° S, in which elevation climbed to a maximum of around 1500 m a.s.l. Mean annual precipitation was estimated to be 4.4 m a^{-1} at sea level west of the main divide, and 10.9 m a^{-1} at a station toward the middle of the profile. At the leeward site of Punta Arenas, mean annual precipitation at sea level dropped to around 0.5 m a^{-1} (Schneider et al. 2003). The west-to-east profile of precipitation in the Patagonian Andes thus shows some similarities to that of the Southern Alps.

The Scandinavian Mountains run approximately southwest to northeast along the length of Norway from 58–71° N. The maximum elevation of this mountain range is 2469 m a.s.l. Over the North Atlantic Ocean, westerlies

and southwesterlies form between the subtropical Azores High to the south and the Icelandic Low to the north. Moist air blowing in from the North Atlantic Ocean and Norwegian Sea leads to around 3.5 m of precipitation on the western Norwegian coastline each year, while orographic forcing contributes to over 5 m a^{-1} in elevated and glaciated regions further inland (Chinn et al. 2005). Some valleys in the lee of the Scandinavian Mountains receive less than 0.5 m of precipitation each year (Barry and Chorley 2003).

The European Alps lie at 43–48° N and are somewhat less exposed to westerly winds. This is due to the lower latitude of the mountain range, a more inland location and the variable orientation of the main orographic axis. Certain situations of surface pressure occasionally force air from the Mediterranean northward over the Swiss Alps, causing a föhn wind to develop north of the main Alpine Ridge. The relationship between elevation and precipitation varies within the European Alps. South of the main Alpine Ridge in Switzerland, no correlation exists between precipitation and elevation, while north of the ridge the correlation is strong (Sevruk 1997). Although the highest regions of the Swiss Alps are over 4000 m a.s.l., precipitation reaches only around 2.3 m each year (Frei and Schär 1998; Weingartner and Pearson 2001). Snowfall typically constitutes 60–80% of total precipitation in the European Alps (Barry 2008).

Panziera and Germann (2010) used weather radar to analyse orographic precipitation in the southern European Alps, between Switzerland and Italy. The dominant factor in determining the intensity and frequency of orographic precipitation was wind velocity upstream of the Alps. Instability in the lower atmosphere was also correlated with more intense rainfall, though to a lesser extent than wind velocity. Wind direction was the primary determinant of the location of the maximum accumulations of precipitation. These atmospheric properties were found to be most influential at around 1000 m a.s.l. upwind of the Alps and 3000 m above the first windward mountains (Panziera and Germann 2010).

2.4   Dynamic modelling of the atmosphere

Dynamic numerical models of the atmosphere are based on the physical laws which govern the thermodynamics, pressure and movement of fluid, such as the equations of motion and state (Holton 1992). Improvements in our understanding of the atmosphere and the advent of high-speed computing in recent decades have led to the development of increasingly complex and realistic models. Simulations can be performed over a range of spatial and temporal scales, in order to provide weather forecasts, reproduce palaeoclimate and make predictions about future climate (Randall et al. 2007).

2.4.1   Numerical weather prediction

Numerical weather prediction (NWP) models assimilate output from a global or regional model with a range of observational data, in order to produce an approximation of the state of the atmosphere at a particular point in time. These observational data may include imagery from geostationary and polar-orbiting satellites, as well as meteorological measurements from aircraft, ships, radiosondes and surface climate stations. The assimilated data are then used as the starting point for the next run of the model, from which a prognosis and forecast are produced, usually for a period of up to 10 days (Kalnay 2003). Sophisticated NWP models have been developed by organisations such as the European Centre for Medium-Range Weather Forecasts (ECMWF), the UKMO and the US National Center for Atmospheric Research (NCAR).

The Hadley Centre of the UKMO has developed a suite of atmospheric and oceanic numerical modelling software called the Unified Model (UM). The UM can be run in a number of different configurations: as a global NWP model, regional NWP model (Uddstrom et al. 2007), general circulation model (Johns et al. 2006), or regional climate model (Jones et al. 2004). The UM was first introduced into operation in 1991 and was originally written in the Fortran 77 programming language (United Kingdom Met Office 1998), but much of the model has subsequently been rewritten in Fortran 90. For numerical weather prediction in the United Kingdom, the UKMO runs

the UM at a resolution of 4 km (United Kingdom Met Office 2009).

The Weather Research and Forecasting (WRF) Model is a freely available mesoscale NWP model. WRF has been developed via a collaborative partnership between many organisations, including NCAR and the National Oceanic and Atmospheric Administration (NOAA) in the United States. The WRF model can be used for both weather prediction and atmospheric research. Dravitzki (2009) used WRF to simulate three heavy precipitation events in the Waikato River catchment between 2005 and 2007, with the spatial resolution of the innermost domain of the model set to 3 km. WRF consistently underestimated the magnitude of precipitation during these events. During a continuous two-year simulation of precipitation across New Zealand from 2005 to 2007, run at 12-km resolution, WRF displayed a common tendency of NWP models to underestimate heavy precipitation and overestimate light precipitation (Dravitzki 2009).

The New Zealand Limited Area Model (NZLAM) is an instance of the UM used at NIWA for numerical weather prediction (Uddstrom et al. 2007). In a case study, NZLAM simulated a severe weather event over the South Island of New Zealand at a spatial resolution of up to 1 km and with time steps as short as 15 seconds (Webster et al. 2008). At this resolution, NZLAM simulated up to 500 mm of precipitation in the Southern Alps during a 24-hour period. However, NZLAM is currently run operationally at a resolution of 12 km. NZLAM, WRF and other NWP models are designed for relatively short-term weather prediction; excessive computational requirements currently make NWP unsuitable for the approximation of long-term spatial patterns of precipitation (Tait et al. 2006).

2.4.2 Reanalyses

Reanalyses are descriptions of the past state of the atmosphere that have been produced by specialised dynamic atmospheric models that are genetically related to NWP models. Reanalysis models assimilate historical meteorological observations from aircraft, ships, satellites, ground stations and rawindondes around the world. Guided by the observational data, the models simulate atmospheric processes and produce meteorological diagnostics at regular time

intervals on a regular spatial grid. These diagnostics include atmospheric pressure, wind velocity, air temperature, specific humidity, relative humidity and precipitation. Global reanalyses have been produced by the National Centers for Environmental Prediction (NCEP) and NCAR (Kalnay et al. 1996), as well as the ECMWF (Uppala et al. 2005).

2.4.3 Global climate models

Climate models simulate atmospheric processes over much longer periods of time than NWP models — typically decades, and sometimes centuries or even millennia (Eby et al. 2009). Over longer time scales, the atmosphere is significantly influenced by its interaction with other geophysical components, such as the ocean, cryosphere and biosphere. Climate models are therefore often coupled with models of these other processes in order to simulate climate more realistically (Weaver et al. 2007).

Given finite computing power, global climate models must be simplified in some way to make long-term simulations feasible. General circulation models usually have considerably coarser spatial and temporal resolution than NWP models, which significantly reduces the amount of computing power required to simulate atmospheric processes over any given length of time. The spatial resolution of current GCMs is typically in the order of hundreds of kilometres (Randall et al. 2007). At this resolution, GCMs provide little detail of regional climatic variations, especially within a topographically diverse country such as New Zealand. In Earth System Models of Intermediate Complexity (EMICs), the model physics are simplified. For example, in the University of Victoria (UVic) Earth System Climate Model (Weaver et al. 2001), the atmosphere is simplified to an energy-moisture balance model, while the ocean retains a high degree of complexity.

2.4.4 Regional climate models

Regional climate models run at a higher spatial resolution than GCMs, typically 30–50 km (Christensen et al. 2007). RCMs are essentially limited-area GCMs, but usually do not have an ocean component. An RCM receives its

lateral boundary conditions (LBCs) from the GCM or reanalyses in which it is embedded. LBCs include atmospheric pressure, temperature and humidity. From these, an RCM simulates atmospheric circulation and climatic processes within its domain. The LBCs of an RCM are usually updated by the GCM or reanalysis at regular intervals, such as every 6 hours.

HadRM3P regional climate model of New Zealand

HadRM3P is an RCM configuration of the Unified Model. NIWA is currently adapting HadRM3P for use in New Zealand. The NIWA version of HadRM3P uses the existing UM Fortran code, but the execution of the model over the New Zealand domain necessitates the development of new input data and parameterisations appropriate for the region. In order to downscale global climatic projections for New Zealand, HadRM3P is nested within a GCM version of the Unified Model known as HadAM3P (Anagnostopoulou et al. 2008). HadRM3P has already simulated New Zealand climate from 2070 to 2100 under the A2 and B2 emissions scenarios (Meehl et al. 2007). Alternatively, the RCM can be tested and calibrated via the use of control runs, during which the LBCs are provided by historical reanalyses such as ERA-40 (Uppala et al. 2005) or NCEP/NCAR (Kalnay et al. 1996). Past control runs of the RCM have simulated New Zealand climate from 1970 to 2000.

During RCM simulations, the geographic coordinates of the model are rotated so as to straddle the equator. This minimises the convergence of the meridians and allows the model to operate within grid cells that are almost square. To analyse output from the RCM in true geographic coordinates, the longitudes and latitudes first need to be rotated back to the mid-latitudes.

HadRM3P contains 19 vertical levels and has a horizontal spatial resolution of around 30 km. The increase in spatial resolution, relative to that of a typical GCM, greatly improves the representation of New Zealand topography, as illustrated in Figure 2.4. Different orographic surfaces can be used in each simulation. Figure 2.5 shows the orography of HadRM3P in the central Southern Alps during the simulations used this thesis. In this image, the RCM elevations overlay a 500 m digital elevation model of the area. To
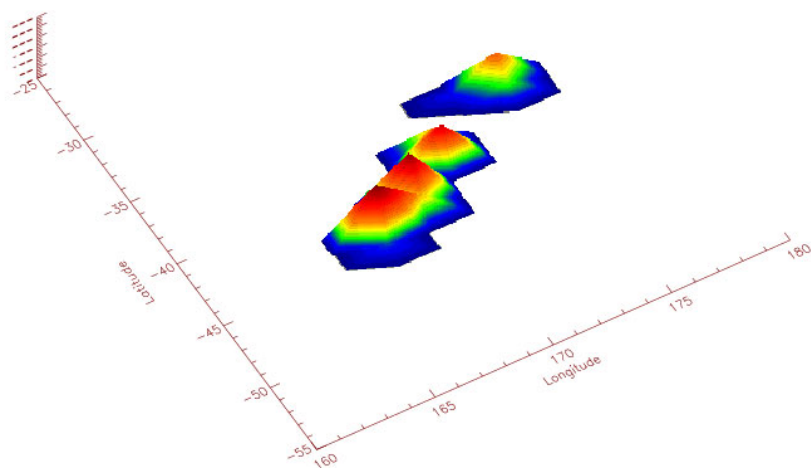
(a) General circulation model, resolution: ~140 km
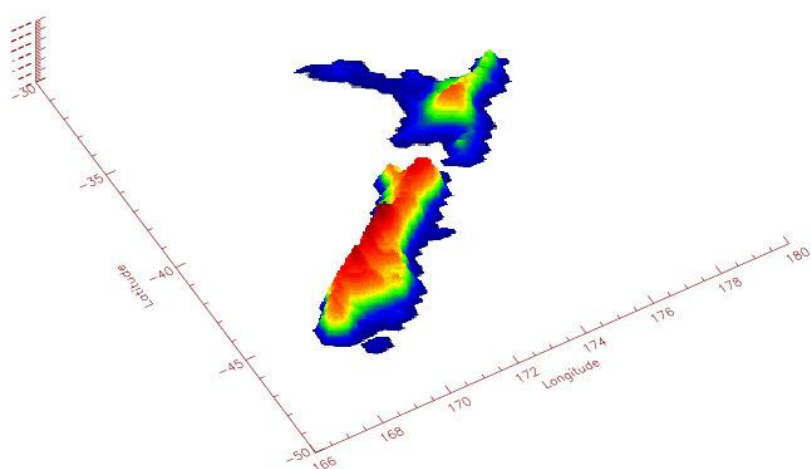
(b) Regional climate model, resolution: ~30 km

Figure 2.4   Orography of New Zealand, as represented by a general circulation model (upper image) and the HadRM3P regional climate model (lower image). Images produced by Dr Sam Dean of NIWA in Wellington, New Zealand.
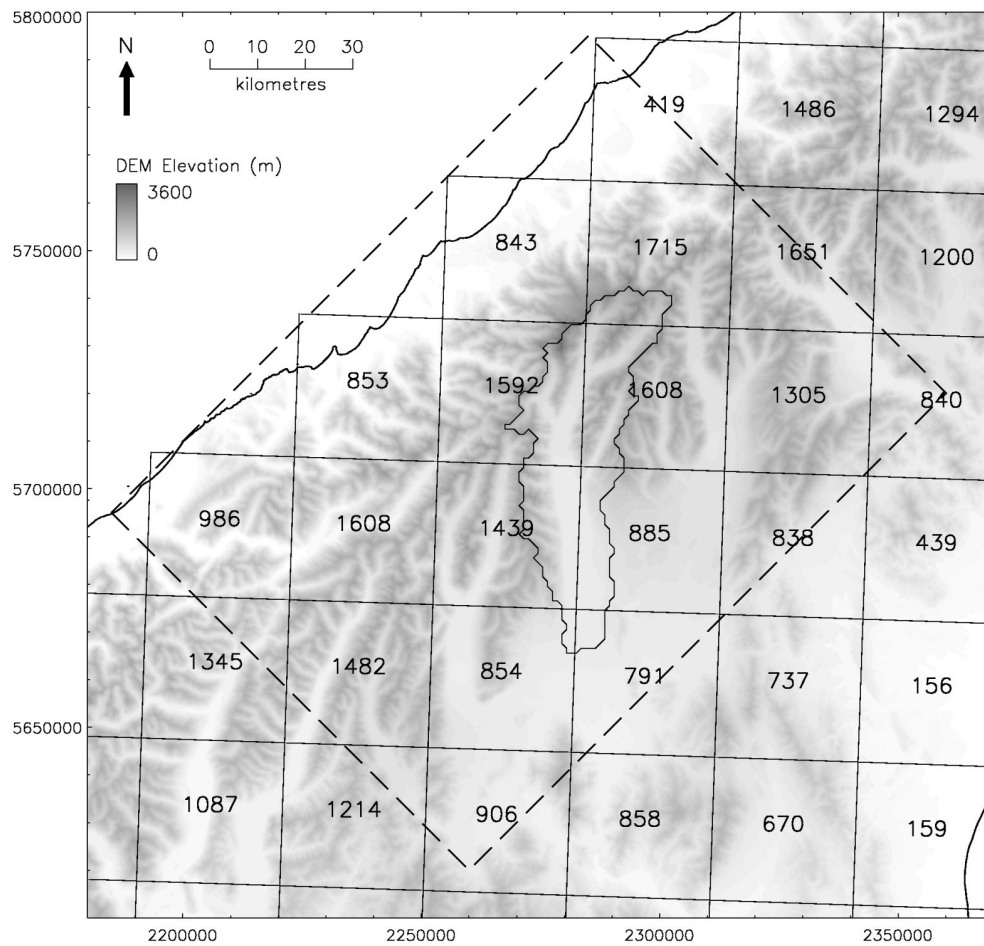
Figure 2.5 Topographic elevations of HadRM3P grid cells (m a.s.l.) in the central Southern Alps. Squares outline the HadRM3P grid cells within the land mask of the model. The dashed line outlines the primary study region, within which Pukaki catchment is outlined. Shading indicates topographic elevations from a 500 m digital elevation model.

produce the orography for the RCM, the topographic elevation of each RCM grid cell is estimated from a DEM of similarly high resolution. However, regions of steep and rugged topographic relief, such as the Southern Alps, cannot be accurately represented at the 30-km resolution of the RCM. For example, at the boundary between the Tasman Sea and the West Coast of the South Island, the orography of the RCM rises sharply and unrealistically from sea level to almost 1000 m a.s.l.

Figure 2.6 represents a single grid cell of the HadRM3P model. The thermodynamic variables of atmospheric pressure, temperature and water content are calculated at a point in the centre of the cell: point 'P'. Zonal and meridional wind vectors (u and v) are calculated at the cell vertices. The model has two precipitation schemes: large-scale and convective. The large-scale scheme resolves precipitation at the 30-km scale of the model grid, and briefly described here is the implementation of this scheme during the RCM simulations used in this thesis (see Sections 5.4 and 5.5). The amount of liquid or ice precipitation within the whole of each grid cell — centred at point P in Figure 2.6 — is diagnosed from the cell's water content, temperature and saturation vapour pressure (Jones et al. 2004). The precipitation subsequently falls at a parameterised fall speed (United Kingdom Met Office 1998). While the simulated rainfall analysed in this thesis is the sum of both large-scale and convective rainfall, large-scale rainfall is dominant in the Southern Alps.

In order to provide a 'faithful' visual representation, the simulated precipitation is often presented as a map containing 30-km squares, with each square cell containing uniform precipitation. However, due to the relatively coarse resolution of the model, this cannot be regarded as an accurate representation of precipitation in the real world.

Previous regional climate models of New Zealand

Renwick et al. (1998) embedded the Division of Atmospheric Research limited-area model (DARLAM) RCM within the output of the 'Mark 2' Commonwealth Scientific and Industrial Research Organisation nine-level atmosphere (CSIRO9) GCM. In this study, an RCM of New Zealand at 50-km resolu-
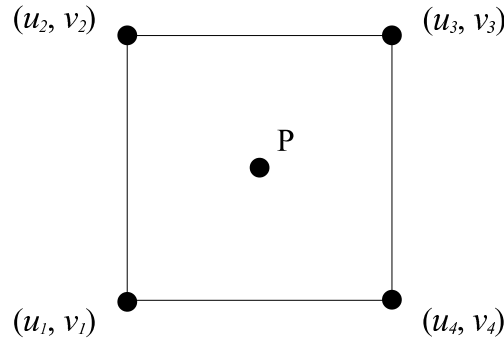
Figure 2.6 A grid cell in the HadRM3P regional climate model. 'P' is the centre of the cell, where atmospheric pressure, temperature and water content are calculated. Zonal and meridional wind vectors (u and v) are calculated at the cell vertices.

tion (RCM50) was driven by an RCM of the Australasian region at 125-km resolution (RCM125), which in turn was nested within the GCM. The RCMs simulated 10-year periods within multidecadal GCM simulations under both present-day (control) and doubled CO_2 conditions. The output of the control simulation was compared to observations of temperature and precipitation at 60 climate stations around the country. However, most of these stations were either coastal or located in relatively low terrain; little data from the Southern Alps was used. The increased horizontal resolution of RCM50 allowed orography to be modelled more accurately. This led to significantly more accurate spatial patterns of mean simulated surface temperature and precipitation. There was a general bias towards excess precipitation at 50-km resolution, though RCM50 performed better than RCM125 at estimating daily variations in rainfall. RCM50 also provided better resolution of the west-east precipitation gradient in the South Island. The doubling of CO_2 resulted in slight changes to the frequency of precipitation extremes in most locations.

Drost et al. (2007) simulated 20-year periods of New Zealand's climate by embedding a previous version of the Unified Model RCM, HadRM3H, within the global HadAM3H model, also based on the Met Office UM. The tropospheric chemistry of each model was fixed at pre-industrial levels. Each model operated using similar dynamics and physics settings, except for some

parameters of the regional model which were altered to suit its higher spatial resolution of 40 km.

HadRM3H adequately simulated major components of regional and seasonal climatic variation around the country. However, anomalous initial and lateral boundary conditions provided by the GCM, such as excessively strong mid-latitude westerlies, lead to certain inaccuracies in the RCM. In parts of the east coasts of both the North and South Islands, this contributed to underestimates of precipitation and excessive temperatures. RCM estimates of precipitation were generally fairly accurate over regions with low or smooth orography. However, precipitation simulated in the west and south of the South Island was significantly different from that recorded in the National Climate Database (CliDB). In mountainous areas, the simulated precipitation was too high and temperatures too low, particularly in the Southern Alps. Drost et al. (2007) believed that the simulation of precipitation might be improved by tuning the RCM's parameterisations of precipitation to the steep orography of New Zealand. The spatial resolution of the model was expected to increase in the future, and this was also likely to help make the model more accurate. Despite the mismatches between simulated climate and observations, the researchers concluded that the overall results from the RCM were promising and that future work would produce increasingly accurate and useful climatic predictions.

Regional climate models in international studies

During research into scenarios of regional climatic change over the United States, Giorgi et al. (1994) found that an RCM provided better estimates of spatial and seasonal variation of precipitation than the GCM in which the RCM was embedded. However, the representation of mountainous terrain within the RCM, at its horizontal resolution of 60 km, lead to overestimates of orographic precipitation, particularly over the more mountainous western regions.

Jones et al. (1995) nested an RCM of Europe within a GCM. The RCM had a horizontal resolution of around 50 km, while the resolution of the GCM in the vicinity of Great Britain was around 270 km. Both models

were versions of the UKMO Unified Model. The RCM simulated a greater amount of precipitation than the GCM, and in mountainous regions this increase correlated strongly with orographic height. The finer resolution and topography of the RCM greatly improved the spatial correlation of simulated and observed precipitation in Great Britain. Regional climate models have also been employed in many other international studies (e.g. Hudson and Jones 2002; da Rocha et al. 2009; Saeed et al. 2011).

2.5 Statistical downscaling of simulated precipitation

Statistical techniques can be employed to increase the spatial resolution of precipitation simulated by dynamic climate models (Mullan et al. 2001; Haylock et al. 2006; Christensen et al. 2007; Ministry for the Environment 2008). During empirical statistical downscaling, observational data are first analysed in order to determine statistical relationships between large-scale predictors and local climatic variables, such as precipitation. The predictors are usually developed from synoptic-scale atmospheric variables such as pressure, wind direction, humidity and temperature. Synoptic situations can be classified using indices such as those developed by Trenberth (1976) or Kidson (2000) for New Zealand. Empirical orthogonal functions can be used to isolate and quantify the key factors which influence the distribution of precipitation in a given area.

Statistical methods are usually less computationally intensive than dynamic climate modelling (Wilby et al. 2004). GCM projections of future global climate have been downscaled for New Zealand using a bivariate linear regression model (Ministry for the Environment 2008). This statistical model is based on relationships between the Trenberth (1976) indices and interpolated grids of daily climate observations in New Zealand. However, statistical downscaling can suffer from insufficient data in isolated regions, and the daily grids can significantly underestimate precipitation in the Southern Alps (Tait et al. 2006).

Kidson and Thompson (1998) compared statistical regression and regional modelling techniques for downscaling GCM output over New Zealand. The RCM used in this study was the Regional Atmospheric Modeling System (RAMS) developed at Colorado State University (Pielke et al. 1992). While both methods had comparable skill in estimating regional anomalies in rainfall and temperature, statistical methods required considerably less computational effort and would therefore be the preferred method in many instances. Peak precipitation rates in the RCM were limited by the 50-km resolution of the model grid and orography. However, Kidson and Thompson (1998) found that convective model-based interpolation better simulated daily precipitation over parts of New Zealand, including the area west of the Southern Alps. The RCM was also inclined to provide estimates superior to those of statistical methods if climatic variations lay significantly beyond the 'normal' range of values from which the regression equations had been developed. Since future climate may be perturbed by increased greenhouse gases and other forcings, these findings suggest that dynamic modelling may be a preferable means of downscaling climatic projections for New Zealand.

2.6   Methods of estimating historical precipitation

The spatial distribution of historical precipitation over a particular area can be estimated via a number of different empirical techniques, some of which are described in this section. Such methods may be based on direct observations of precipitation by rain gauges, weather radar or satellites. Alternatively, the amount of rainfall within a catchment may be inferred from observations of river flows.

2.6.1   Spatial interpolation of observations

Observations from point-based rain gauges can be interpolated via a number of different techniques, in order to produce a surface of areal-average precipitation. Theissen polygons are a relatively simple method of interpola-

tion, but one which results in sharply stepped plateaux of rainfall. Another approach is for a meteorologist to draw, by hand, isoyets of equal rainfall, taking into account the available observations, as well as his or her expert knowledge of the weather patterns of the region. This technique is often more accurate than simpler methods but is also more time-consuming. The New Zealand Meteorological Service (1985) used this method to produce a map of mean annual rainfall over the whole of New Zealand for the 30-year period from 1951 to 1980. The interpolation was necessarily more subjective in regions where observational data were sparse, such as the Southern Alps (Tait et al. 2006).

Alternatively, observations from rain gauges can be interpolated via more mathematical techniques such as kriging and splines. While such methods still encounter problems resulting from a shortage of observations in remote regions, the subjectivity associated with hand-drawn contours can be removed. A spline comprises piecewise polynomial functions which connect a number of data points. The polynomial pieces have continuous derivatives at the data points, making the composite spline function smooth. The bending energy of the composite curve is minimised; the curvature of a spline is thus analogous to that of a rubber strip forced through certain breakpoints. As a function of a single independent variable, a spline forms a two-dimensional curve of the dependent variable; functions of two or more independent variables can produce a surface (de Boor 1978; Wahba 1990).

A thin-plate smoothing spline is fitted to a set of data points by minimising both the roughness and the residuals of the fitted function. The balance between smoothness and fidelity is controlled by a 'smoothing parameter' (ρ): a larger value of ρ results in more smoothing and a looser fit to the supplied data points. A common way to determine the optimum value of ρ is to minimise a measure of the predictive error of the fitted spline known as the generalised cross validation (GCV) (Craven and Wahba 1979). A useful diagnostic of a thin-plate smoothing spline model is the 'signal', which is the effective number of degrees of freedom of the fitted spline (Hutchinson and Gessler 1994). Minimising the GCV may result in very small values for both ρ and the residuals, accompanied by a signal equal to the number of

supplied data points. This indicates that the spline is effectively an exact interpolant and normally means that the value of ρ has not been genuinely optimised. A signal equal to more than half the number of data points can indicate that the thin-plate smoothing spline has been supplied with insufficient data to adequately represent the true surface (Hutchinson and Gessler 1994; Hutchinson 2000).

The frequency distribution of short-term precipitation is typically positively skewed, with fewer instances of high amounts of precipitation. A square-root transformation is often employed to decrease the skewness of daily precipitation, bringing its distribution more into line with the upper tail of a normal distribution (Hutchinson 1998a,b; Tait et al. 2006; Hutchinson et al. 2009). This can improve the accuracy of a thin-plate smoothing spline model. Using this transformation, the square roots of the dependent variable – that is, the precipitation — are interpolated; the fitted values are then squared to produce the final surface. The accuracy of the surface can be estimated by comparison to withheld data points. When interpolating observations of daily precipitation using a thin-plate smoothing spline, a square-root transformation has been shown to significantly improve estimates of withheld data points (Hutchinson 1998a; Tait et al. 2006).

In addition to the available observations, other predictors of the spatial distribution of precipitation can be mathematically incorporated into a spline interpolation (Hutchinson 1995). Such predictors may include grids of topographic elevation and aspect. These predictors may be used as independent variables or linear covariables within the interpolation. The inclusion of additional predictors can significantly improve the accuracy of the interpolated surfaces of precipitation (Hutchinson 1998b).

Daily and annual climatic surfaces for New Zealand from 1960 to 2010 have been produced by interpolating observations at stations using a trivariate thin-plate smoothing spline (Tait et al. 2006) (Figure 2.7). The precipitation surfaces formed by this interpolation have a relatively high spatial resolution of 0.05 degrees of latitude and longitude, which equates to around 4.2 km by 5.5 km, respectively. The trivariate spline employs the 1951–1980 mean annual rainfall surface — produced by the New Zealand Meteorologi-
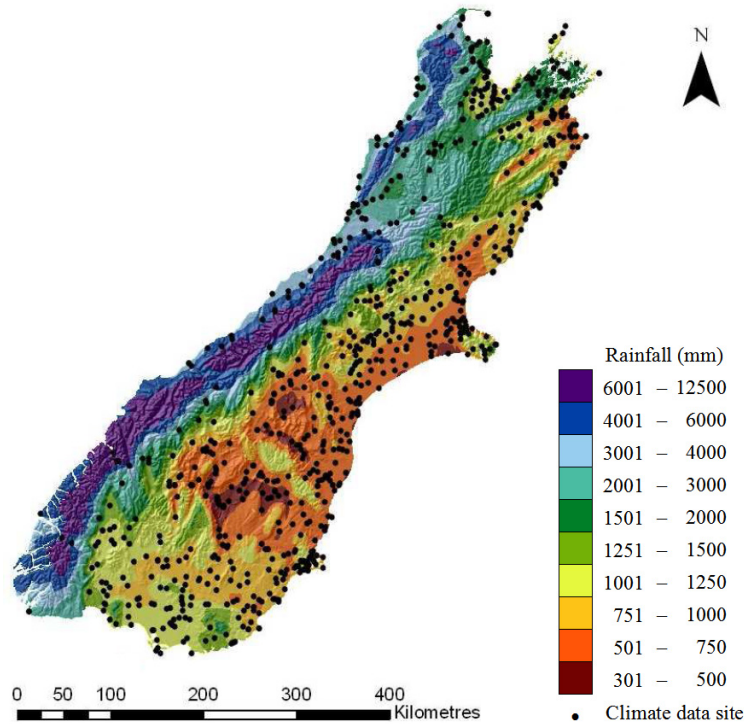
Figure 2.7 Median annual rainfall in the South Island of New Zealand from 1971 to 2000. Image reproduced from Tait and Zheng (2007).

cal Service (1985) — as a third independent variable, in addition to latitude and longitude. The assumption of this technique is that over the period for which the surface is being constructed, the precipitation experienced by a particular area is a function of both its horizontal location and the mean annual precipitation previously experienced at that location, as specified by the 1951–1980 rainfall surface. The inclusion of the mean annual rainfall surface helps guide the spline toward 'realistic' values in areas in which observational data is sparse.

A shortage of observations in mountainous areas can lead to significant uncertainty during the interpolation. When validated against observations from rain gauges during a 36-day period, the interpolated surface underestimated rainfall by up to 46% in some highly elevated regions of the Southern Alps (Tait et al. 2006). The locations of precipitation maxima in these climatic surfaces of the Southern Alps are known to have a bias toward the

crest of the Main Divide. Additionally, since a single map of mean annual precipitation is used in the interpolations, and westerlies predominate in New Zealand, interpolated precipitation during non-westerly days is likely to be biased toward a westerly climatology. Tait et al. (2006) suggested that the accuracy of the interpolated daily precipitation surfaces for New Zealand could be improved by incorporating, as a third independent variable, different mean precipitation surfaces, each tailored to a typical synoptic situation for the country. Tait and Turner (2005) improved estimates of rainfall in remote New Zealand catchments by integrating mesoscale weather simulations into a trivariate spline interpolation.

2.6.2   Weather radar and satellite observations

Reflectivity from weather radar can be used to estimate precipitation, but few weather radar sites operate in the South Island and radar is obstructed by mountains (New Zealand Meteorological Service 2010). This precludes the use of radar for the accurate estimation of precipitation in the Southern Alps. Microwave sensors in polar-orbiting satellites can directly estimate precipitation over very wide areas, but these satellites take snapshots over any given surface area only two or three times a day. Such low temporal sampling limits the amount of data available for accurate estimates of precipitation in any particular region (Tait et al. 2006).

2.6.3   Models of orographic precipitation

Models can be developed specifically for the estimation of orographic precipitation. Griffiths and McSaveney (1983) formulated equations which describe the logistic growth of precipitation across two-dimensional profiles of topography in mountainous regions of New Zealand. In their model, the precipitation estimated at a particular location within a transect is a function of both local elevation and the distance to the crest of the main topographic ridge. The model can be calibrated using observations from rain gauges, in order to improve the accuracy of isohyets of rainfall in remote mountainous catchments (Griffiths and McSaveney 1983).

Both short-term and long-term orographic precipitation have been estimated in parts of New Zealand using a diagnostic model developed by Sinclair (1994) and Thompson et al. (1997). This model is based on the wind velocity upstream of mountains, V, and the topographic gradient, ∇Z, and is thus known as VDEL. VDEL can be initialised with data from global reanalyses or local atmospheric soundings. The model was validated against precipitation estimated from catchment runoff in a mountainous region of the southern North Island, with errors generally lying between 5 and 10 per cent (Thompson et al. 1997).

2.6.4 Water balance within hydrological catchments

Precipitation can be estimated by quantifying the major downstream components of the overall water balance in a catchment: evapotranspiration and runoff. Rates of evapotranspiration can be estimated from the climate, vegetation and albedo of the catchment (Zhang et al. 2004), and runoff can be gauged from observations of river flows. Variations in groundwater are often treated as negligible over periods of a decade or more (Thompson et al. 1997; Tait et al. 2006). In elevated catchments of the central Southern Alps, such as Tekapo and Pukaki, changes in the volume of water stored in glaciers and snow also need to be taken into account (McKerchar et al. 1998). Tait et al. (2006) validated surfaces of interpolated daily precipitation in New Zealand against river flows. Kerr (2009) also used a water balance approach to validate surfaces of mean precipitation in the Pukaki catchment from 1971 to 2000.

2.7 Summary

- The Southern Alps are highly exposed to moist air carried across the Tasman Sea by the mid-latitude westerlies, and orographic forcing leads to extremely high levels of precipitation.

- A scarcity of observations at high elevations contributes to considerable uncertainty about the magnitudes and processes of precipitation in the

more remote regions of these mountains.

- The distribution of precipitation may be estimated via a number of different empirical methods, including interpolative and statistical techniques, though these approaches may be hindered if data are sparse.

- Dynamic atmospheric models, such as RCMs, can perform well in areas of low topographic relief, but precipitation is difficult to simulate accurately in mountainous regions of the South Island.

- While both interpolative and dynamic downscaling techniques have drawbacks when applied to remote mountainous regions, such modelling, combined with the available observational data, does offer a way to gain a better understanding of the distribution and influences of orographic precipitation.

Chapter 3

Observational data

To fulfil the objectives of this thesis — listed earlier in Chapter 1 — it is necessary to describe the spatial distribution of historical rainfall in the Southern Alps. With this aim, observations were compiled from several hundred rain gauges across a broad region of the South Island, as detailed in Section 3.1. These observations were used to construct profiles and surfaces of rainfall, and to validate precipitation simulated by the regional climate model. To help identify primary influences upon the spatial distribution of historical precipitation, the rainfall profiles were compared to reanalyses of atmospheric properties, which are described in Section 3.2. An independently developed surface of mean annual precipitation in the Pukaki catchment (Section 3.3) was used to further validate the simulated precipitation.

3.1 South Island rain gauges

Observations from rain gauges in the South Island were retrieved from the National Climate Database (CliDB) (NIWA 2010a). CliDB is administered by NIWA and includes observations of daily rainfall from over 3500 sites in or near New Zealand, the earliest of which date back to 1852. Most of these sites have since closed, but more than 700 CliDB stations recorded observations of rainfall during 2010. Rainfall is not recorded in many mountainous areas and observations at high elevations in the Southern Alps are particularly sparse.

During the past few decades, rain gauges have been have been installed

at a number of sites in the Southern Alps by local governmental organisa-
tions — such as the West Coast and Canterbury regional councils — and
hydroelectric companies, such as Meridian Energy. Both manual and auto-
matic gauges have been installed, and data from many of these sites are not
currently present in CliDB. Dr Martyn Clark, formerly of NIWA, extracted
these additional data from the Water Resources Archive (WRA) (Walter
2000; NIWA 2007) using the Tideda software package (NIWA 2010b). The
WRA is also managed by NIWA and includes rainfall data from the National
Hydrometric Database and regional archives.

3.1.1   Domain of rain gauges

The domain of rain gauges used in this thesis extends over much of the South
Island (Figure 3.1), and is based on the grid used by Henderson and Thomp-
son (1999). The domain's baseline is aligned with — and approximately
85 km southeast of — the New Zealand Alpine Fault. The baseline origi-
nates in Cape Providence at the southwestern tip of Fiordland, and extends
to its northeastern terminus near the town of Oxford in central Canterbury.
The line of the Main Divide has been significantly deformed by tectonic ac-
tivity, and ranges from 40 km northwest of the baseline in the Milford region,
to 70 km northwest of the baseline near Franz Josef. The domain itself mea-
sures 400 km from southwest to northeast, beginning 150 km northeast of
Cape Providence. From the baseline, the domain extends northwest over the
Southern Alps to the Tasman Sea. The domain shown in Figure 3.1 extends
20 km southeast of the baseline, so as to encompass the entire domain of the
ARC energy-balance glacial model.

The domain was further extended to 120 km southeast of the baseline
(Figure 3.2) to encompass 572 rain gauges and a greater number of RCM
grid points (Figure 4.2). The inclusion of the additional RCM grid points
aided the downscaling of precipitation simulated in the central Southern Alps,
as described in Section 4.2.

The domain was originally divided into four transects of the Southern
Alps, each 100 km wide: Hokitika, Franz Josef, Haast and Milford. This di-
vision facilitates the analysis of spatial variations in precipitation along the
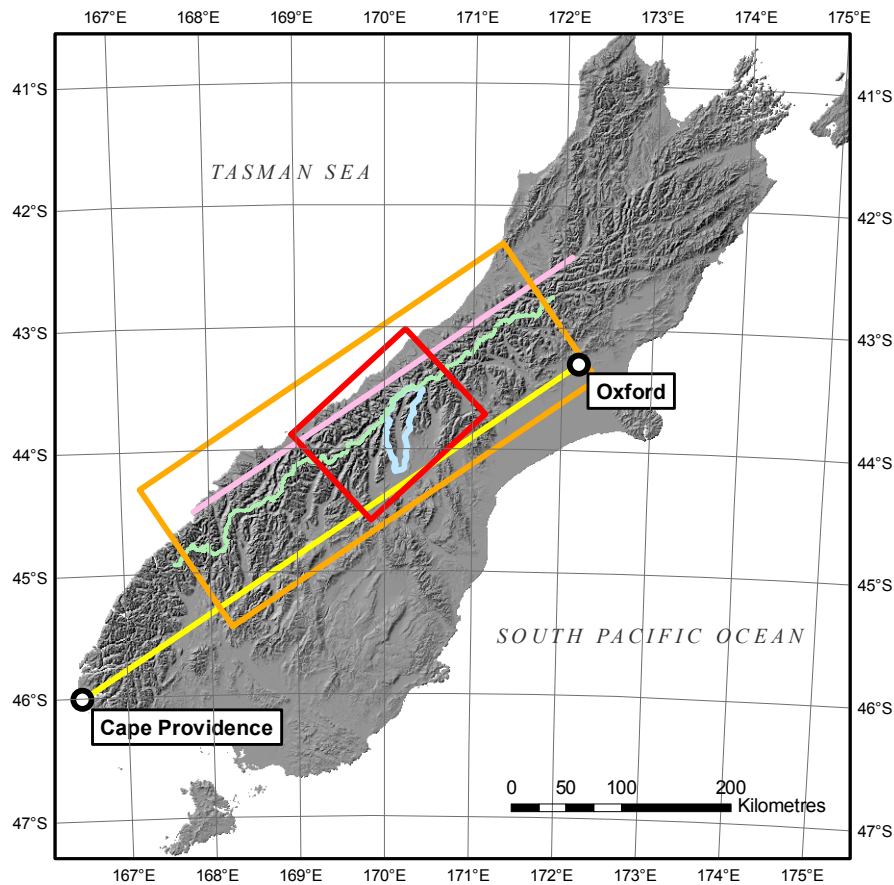
Figure 3.1 Topography of the South Island. The New Zealand Alpine Fault is approximated in the Southern Alps region by the pink line. The study baseline (yellow line) extends from Cape Providence northwest to near Oxford, in a line parallel to the Alpine Fault. The orange line outlines the domain of rain gauges from 20 km southeast of the baseline northwest to the Tasman Sea. The Main Divide of the Southern Alps within this domain is shown by the light green line. The red line outlines the primary study region. The light blue line outlines the Pukaki catchment.
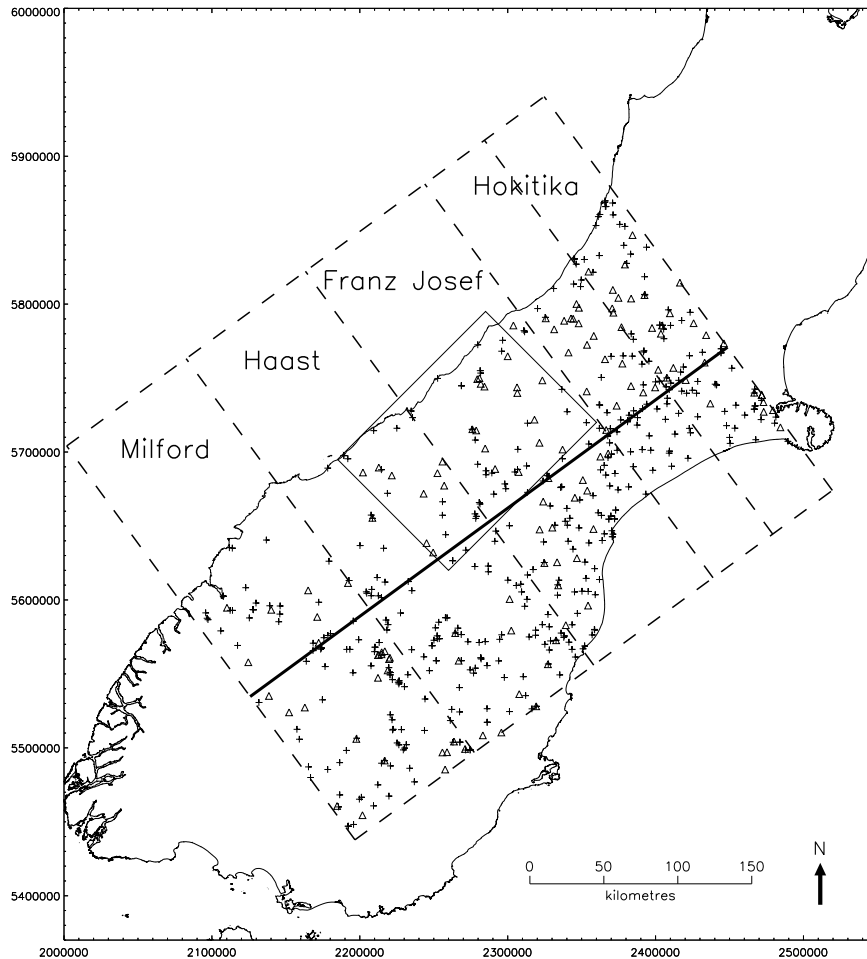
Figure 3.2 Transects and rain gauges in the South Island from 1971 to 2000. '+' symbols denote CliDB gauges, '△' symbols denote WRA gauges. The primary study region is within the rectangle outlined by a solid line in the centre of the map. The transects are delineated by dashed lines. The baseline is represented by the thick solid black line running from southwest to northeast. The domain is based on that used in Henderson and Thompson (1999).
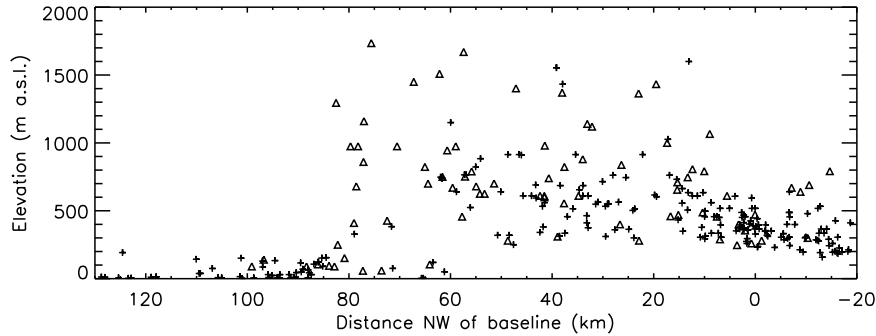
Figure 3.3 Elevation of rain gauges (m a.s.l.) versus distance northwest of baseline (km). '+' symbols denote CliDB gauges, '△' symbols denote WRA gauges.

northeast-to-southwest axis of the mountain range. The original Hokitika transect contained a large number of gauges (177), relative to the number of gauges in each of the other transects (Franz Josef: 137; Haast: 131; Milford: 127). Therefore in order to further resolve spatial variations in precipitation along the main axis of the Southern Alps, the Hokitika transect was divided into a northeast transect and a southwest transect, each of which was 50 km wide. Details of rain gauges in each of these transects of the Southern Alps, including the total precipitation recorded at each gauge from 1971 to 2000, are listed in Appendix A.

Figure 3.3 shows the elevation of rain gauges across the profile of the Southern Alps. Moving from northwest to southeast, the elevation of the gauges increases suddenly a few kilometres southeast of the New Zealand Alpine Fault, which is around 85 km northwest of the baseline. The WRA gauges are generally more elevated than those in CliDB. Within the extended domain, 29% of the WRA gauges, and only 4% of the CliDB gauges, are at elevations over 750 m a.s.l. (Table 3.1).

Undercatch of precipitation by rain gauges at high elevations in the Southern Alps has been estimated to be over 20% (Kerr 2009). However, given the difficulty of accounting for such errors in a large data set, no error corrections were applied to observations from rain gauges in this thesis.

Table 3.1   Number of rain gauges in each transect of the Southern Alps from 1971 to 2000. '> 750 m a.s.l.' refers to gauges located more than 750 m a.s.l. The domain of the rain gauges extends 120 km southeast of the baseline.

Transect	> 750 m a.s.l.			All Elevations		
	CliDB	WRA	Total	CliDB	WRA	Total
Northeast Hokitika	4	6	10	81	31	112
Southwest Hokitika	1	10	11	46	19	65
Franz Josef	5	12	17	104	33	137
Haast	1	4	5	111	20	131
Milford	7	6	13	99	28	127
All	18	38	56	441	131	572

3.1.2   Period of observation

The standard period of climatological normals is 30 years, usually beginning in the first year of a calendar decade (World Meteorological Organization 1983). Observations from rain gauges in the Southern Alps were compiled over the most recent 30-year period that conformed to this standard at the commencement of this thesis, that is, 1 January 1971 to 31 December 2000. The use of the 1971–2000 period also allowed the compiled observations to be directly compared to a 1970–2000 control run by the RCM, which is described in Section 4.2.

As stated in Chapter 1, one of the objectives of this research is to identify the strongest influences upon the spatial distribution of precipitation in the Southern Alps. To this end, observations from rain gauges were compared with atmospheric properties from NCEP/NCAR Reanalysis 1. The reanalyses and RCM data had both previously been aggregated into 24-hour periods from 00:00–00:00 Coordinated Universal Time (UTC), which is equivalent to the period from 12:00–12:00 New Zealand Standard Time (NZST).

Since the austral summer of 1974/75, daily rainfall at CliDB gauges has usually been measured over 24-hour periods from 08:00–08:00 NZST during New Zealand Daylight Saving, and 09:00–09:00 NZST at other times of the

year. This equates to observational periods of 20:00–20:00 UTC during the austral summer months, and 21:00–21:00 UTC during the austral winter months. The 24-hour periods covered by the daily reanalyses and RCM data were thus either 3 or 4 hours later than those of the daily CliDB observations (Table 3.2). This time lag could be resolved by the use of hourly observations of rainfall, but fewer CliDB sites provide hourly rainfall data. The temporal resolution of daily rainfall data poses no problem to the calculation of 30-year normals. Daily rainfall was therefore retrieved from the CliDB database. CliDB gauges were compared to the NCEP/NCAR reanalyses, but were not used to validate short-term precipitation simulated by the RCM. Rainfall at some CliDB stations is occasionally observed over a period of several days rather than a single day. Such observations were not compared with daily reanalyses, but were included in the calculation of 30-year normals.

The WRA data were received in hourly format and then aggregated into UTC days, that is, 24-hour periods from 00:00–00:00 UTC. The 24-hour periods of observation at WRA gauges and CliDB gauges were therefore slightly inconsistent, with the CliDB observation days being either 3 or 4 hours earlier than those of the WRA gauges. However, compiling the WRA observations into UTC days allowed the WRA gauges to be directly compared to both the NCEP/NCAR reanalyses and the HadRM3P-simulated precipitation. The inconsistency between the daily observation periods of the CliDB and WRA gauges was therefore considered acceptable. For the 30-year normals, the difference between the observation periods of the CliDB and WRA gauges equates to only 3 or 4 hours in a period of 30 years; the influence of this difference was considered negligible.

It must be noted that in the raw WRA data, successive hourly amounts of precipitation occasionally repeat for several hours or even days, which suggests that a multi-hour reading may have been split into equal hourly amounts. In one noted instance, the amount of precipitation observed at a particular WRA gauge recurs hourly for a period of 25 consecutive days. Such repetition is not common in this data set, but it must be acknowledged. In future analysis, it may be possible to reaggregate these data into their original periods of observation. In this thesis, however, all WRA observations were

Table 3.2 Time periods of rain gauges, NCEP/NCAR Reanalysis 1 and HadRM3P-simulated precipitation.

Name	Time Period (UTC)
Rain gauges, CliDB	21:00 - 21:00 (austral winter);
	20:00 - 20:00 (austral summer)
Rain gauges, WRA	00:00 - 00:00
NCEP/NCAR Reanalysis 1	00:00 - 00:00
HadRM3P-simulated precipitation	00:00 - 00:00

simply aggregated into 24-hour UTC days.

The mean daily precipitation observed at each gauge from 1971 to 2000 was calculated by dividing the total recorded precipitation by the total number of daily observations. Of the 306 gauges located in the domain from 20 km southeast of the baseline northwest to the Tasman Sea, only 14 had recorded less than 1 year of data. Due to the relatively small number of short-term sites, a minimum observational period was not enforced. Thus all daily precipitation recorded within the domain from 1971 to 2000 was used in the analysis. Mean annual precipitation observed at each rain gauge was calculated by multiplying the mean daily precipitation by the number of days in a Julian year: 365.25. Mean annual precipitation at short-term sites was not normalised to observations from long-term stations.

3.2   Atmospheric properties in global reanalyses

Mean daily wind velocity, air temperature and specific humidity were extracted from Reanalysis 1 of the NCEP/NCAR global reanalyses (Kalnay et al. 1996). NCEP/NCAR have interpolated these reanalyses on to a global regular grid at a horizontal resolution of 2.5° latitude and longitude. The locations of 6 reanalysis grid points in the region of the Southern Alps are shown in Figure 3.4. For simplicity, data from only one reanalysis grid point
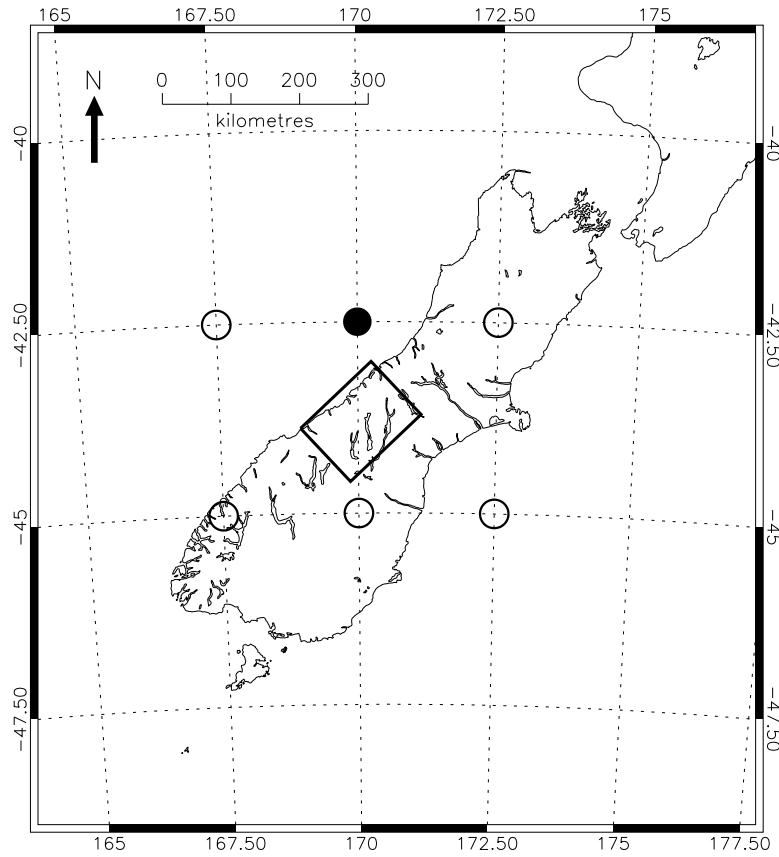
Figure 3.4   Grid points near the Southern Alps in NCEP/NCAR Reanalysis 1. '●' denotes the grid point at 42.5° S 170° E, which was used in this thesis; 'O' symbols denote unused additional grid points.

was used in this thesis. Data were retrieved from the grid point immediately to the north of the primary study region, at 42.5° S 170° E. Given the predominance of westerlies in the mid-latitudes, this is the grid point on the 'upwind' side of the Southern Alps that lies nearest to the central Southern Alps. Data was extracted from the single pressure level of 850 hPa. Reanalyses from 1 January 1971 to 31 December 2000 were used in this thesis.

Horizontal wind velocity in NCEP/NCAR Renalysis 1 is divided into zonal and meridional wind vectors. Figure 3.5 shows mean zonal wind velocity at the 850 hPa pressure level on 5 November 1994 UTC, the first day of the 'Guy Fawkes Storm' in the Southern Alps. The mid-latitude westerlies are clearly visible, and particularly so in the Southern Hemisphere where the
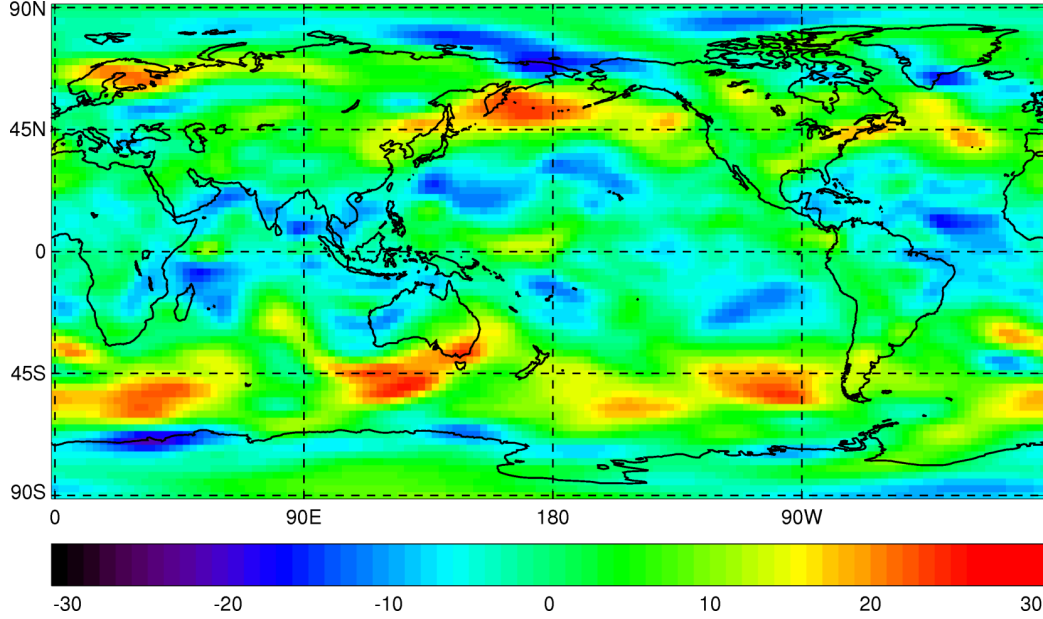
Figure 3.5   Mean daily zonal wind velocity (m s^{-1}) at 850 hPa on 5 Nov 1994 UTC, as represented in NCEP/NCAR Global Reanalysis 1. Westerly flow is positive and is indicated by warm colours.

zonal flow of air experiences less obstruction from land masses.

3.3   Mean annual precipitation in the Pukaki catchment

The Pukaki catchment occupies around 10% of the land within the primary study region. Kerr (2009) produced surfaces of mean annual precipitation in the Pukaki catchment from 1971 to 2000. These surfaces are shown in Figure 3.6. Surf$_{\text{Obs.TK.M}}$ (Figure 3.6a) is based on the amount of precipitation actually measured at rain gauges, while Surf$_{\text{Obs.TK.T}}$ (Figure 3.6b) represents the estimated 'true' precipitation by also taking into account the estimated undercatch at rain gauges. The horizontal precipitation gradient of both surfaces is very steep in the northern part of the catchment near the Main Divide, where it reaches 1 m a^{-1} km^{-1}. Precipitation in Surf$_{\text{Obs.TK.T}}$ peaks at over 13 m a^{-1} in this region.
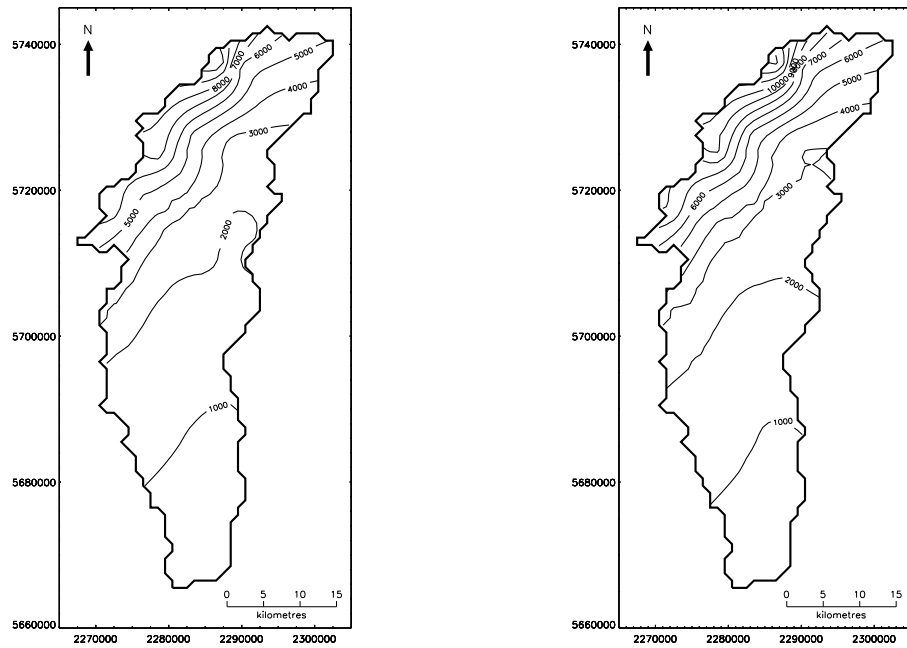
(a) Measured precip. (Surf$_{\mathrm{Obs.TK.M}}$)   (b) 'True' precip. (Surf$_{\mathrm{Obs.TK.T}}$)

Figure 3.6   Isohyets (mm a^{-1}) of estimated mean annual precipitation in the Pukaki catchment from 1971 to 2000, as determined via ordinary kriging of observations from rain gauges (Kerr 2009). The left surface (Surf$_{\mathrm{Obs.TK.M}}$) is based on measured precipitation, while the right surface (Surf$_{\mathrm{Obs.TK.T}}$) also takes into account the estimated undercatch at rain gauges.

As part of the research by Kerr (2009), new rain gauges were installed in highly elevated regions of the catchment. These additional rain gauges are not present among the CliDB and WRA gauges described in the previous section. The construction of these surfaces of precipitation in Pukaki was rigorous and independent of the present research. The surfaces produced by Kerr (2009) were therefore used to validate the precipitation simulated by the RCM in the Pukaki catchment. $Surf_{Obs.TK.M}$ and $Surf_{Obs.TK.T}$ were received in ESRI ASCII grid format at a spatial resolution of 1 km (Kerr 2010).

3.4 Summary

The observational data used in this thesis comprise:

- precipitation recorded by 572 rain gauges in the South Island during the 30-year period from 1971 to 2000, compiled from the New Zealand National Climate Database and the Water Resources Archive managed by NIWA.

- wind velocity, air temperature and specific humidity at 850 hPa 42.5° S 170° E, north of the central Southern Alps, from 1971 to 2000, extracted from NCEP/NCAR Reanalysis 1;

- surfaces of mean annual precipitation in the Pukaki catchment from 1971 to 2000, developed by Kerr (2009).

Many of these data have not previously been included in such an analysis.

Chapter 4

Methodology

As stated in Chapter 1, the focus of this thesis is the spatial distribution of precipitation in the central Southern Alps, and the manner in which it is influenced by topography and wind direction. A better understanding of the rainfall distribution in the central Southern Alps, and its primary determinants, has many potential applications. One such application is to help improve the spatial resolution of dynamically simulated precipitation in this region, which may in turn provide insight into glacial and hydrological processes. However, as mentioned in previous chapters, there is a shortage of observational data in elevated parts of the Southern Alps; this makes it difficult to produce an accurate surface of historical precipitation via a simple two-dimensional interpolation of the available point-source rain gauges. Adopted in this thesis is an alternative approach, which utilises the distinct cross-mountain profile of orographically enhanced precipitation, following and extending the work of Henderson and Thompson (1999). The construction of these profiles is described in Section 4.1.1. As noted in Chapter 1, one of the objectives of the present research is to incorporate the cross-mountain profile into the downscaling of precipitation simulated in the central Southern Alps by the HadRM3P regional climate model. This was achieved by first joining the rainfall profiles together to produce surfaces of observed precipitation in the Southern Alps (Section 4.1.2). The subsequent integration of the observed precipitation surfaces into the downscaling of simulated precipitation is described in Section 4.2.

4.1 Spatial interpolation of observations from rain gauges

4.1.1 Interpolated profiles of observed precipitation

In order to create profiles of observed precipitation across the Southern Alps, it was necessary to first define the position of each rain gauge on a coordinate grid aligned with the main axis of the mountain range. As described in Section 3.1.1, the domain used in this analysis is based on that used by Henderson and Thompson (1999). This domain runs approximately parallel to the New Zealand Alpine Fault, and the axes of the grid are shown in Figure 4.1. The y-axis of the grid forms the domain's baseline, which extends from Cape Providence in Fiordland, northeastward through the town of Oxford in Canterbury. The x-axis represents distance across the Southern Alps, which equates to the distance northwest of, and perpendicular to, the baseline.

The mean annual precipitation observed at each rain gauge from 1971 to 2000 was calculated, as described in Section 3.1.2, and then plotted against its distance northwest of the baseline. Examples of these profile plots are presented in Figure 5.2 of the Results chapter. Precipitation recorded across the transects can vary significantly between individual stations in the most mountainous regions, around 40–90 km northwest of the baseline (Figure 5.2a). In these areas, airflow may be modified by local topographic variations to produce localised peaks and troughs of rainfall. A form of approximation is necessary to produce a line of 'best fit' to the profile, but interpolative methods may ignore important local variations entirely if the data are too 'noisy'. Neither a cubic spline nor a B-spline (de Boor 1978, chap. 13) of the individual gauges produced, upon visual inspection, a good fit to the general trend of the profile. To help guide the spline toward observations from long-term stations — which ought to have lower standard errors of mean annual precipitation than short-term stations — each individual gauge was assigned a weighting proportional to the number of observation days at that gauge. The weighted gauges were then interpolated using a least-squares B-spline
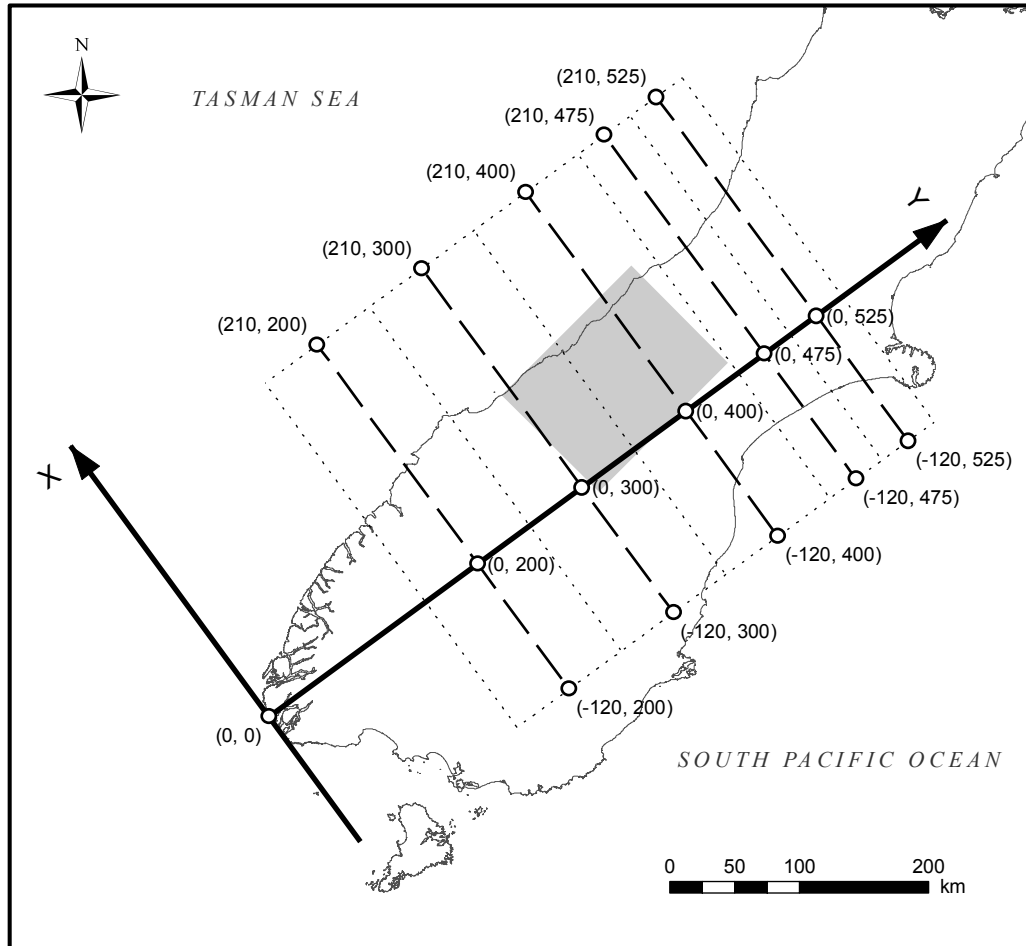
Figure 4.1 Coordinate grid aligned with the main axis of the Southern Alps. The thick solid lines, terminated by arrow-heads, represent the axes of the grid: Y is the baseline; X is the distance northwest of, and perpendicular to, the baseline. The dotted lines outline the domains of the five transects used in this analysis: (from northeast to southwest) northeast Hokitika, southwest Hokitika, Franz Josef, Haast and Milford. The dashed lines bisect the domain of each transect. 'o' symbols mark the grid origin, the end-points of each transect, and the intersections of each transect with the baseline. The coordinates of these points are indicated in (x, y) format. The grey shaded area is the primary study region.

(de Boor 1978, chap. 14). However, the use of weightings made no discernible improvement to the poor fit of the individual gauges.

The x-axis of each profile was therefore separated into 5-km divisions. The mean annual precipitation within each division was calculated by taking a simple average of the mean annual precipitation observed at all the individual stations within each division. The averages within each division were then interpolated across the Southern Alps using a one-dimensional cubic spline (de Boor 1978, chap. 4) to create the line of best fit. No weightings were applied. If no gauges were present in a particular division, then that division was omitted from the interpolation. This combination of averaged 5-km divisions and a cubic spline produced the precipitation profile that, upon visual inspection, best fitted the general trend of the observations from individual rain gauges. This method was therefore adopted for the construction of all precipitation profiles for the remainder of the analysis.

Profiles were constructed for the Southern Alps as a whole, and individually for the northeast Hokitika, southwest Hokitika, Franz Josef, Haast and Milford transects. To enable the profiles to be combined into a single surface, the lengths of the five profiles first needed to be made equal. This was achieved by extrapolating the profiles over the Tasman Sea and South Pacific Ocean. Extrapolated values were set to the mean annual precipitation in the 5-km divisions at the tails of each profile. The extrapolated values exerted little influence on the splined surface, other than to provide reasonable boundary conditions with which to constrain the spline.

4.1.2   Interpolated surfaces of observed precipitation

The domains of each of the five transects (northeast Hokitika, southwest Hokitika, Franz Josef, Haast and Milford) are outlined by the dotted lines in Figure 4.1. These domains were bisected, as indicated by the dashed lines in Figure 4.1, and the five corresponding interpolated profiles of precipitation were georeferenced to these bisecting lines. The profiles were then merged into a single three-dimensional surface using a two-dimensional, tensor-product B-spline (de Boor 1978, chap. 17). The spatial resolution of this interpolated surface was 100 m.

4.2 Downscaling of simulated precipitation

The downscaling method could be applied to precipitation simulated during an historical control run, or to precipitation simulated under a future climatic scenario. The analysis in this thesis focuses on precipitation simulated by HadRM3P during the period from 1971 to 2000. The use of this historical period allowed the skill of the downscaling method to be subsequently assessed via comparisons with observations. Dr Sam Dean of NIWA performed the simulation, which was executed on the Cray T3E1200e supercomputer at NIWA in Wellington, New Zealand. HadRM3P and its topography during this simulation are described in more detail in Section 2.4.4. The unrotated RCM domain has latitudes of 31–52° S, longitudes from 160° E to 168° W, and a spatial resolution of approximately 30 km. Lateral boundary conditions from 1970 to 2000 were provided at 6-hourly intervals from NCEP/NCAR Reanalysis 1 (Kalnay et al. 1996). Dr Dean aggregated the simulated precipitation into 24-hour periods from 00:00–00:00 UTC. These data were stored in netCDF format (Rew and Davis 1990).

A trivariate thin-plate smoothing spline was used to downscale the spatial resolution of the simulated precipitation from 30 km to 100 m. The trivariate interpolation was performed using version 4.36 of the ANUSPLIN software package (Hutchinson 2011). The first two independent variables of the spline were two horizontal spatial coordinates: NZMG easting and northing. The third independent variable was mean daily precipitation observed in the Southern Alps from 1971 to 2000. The dependent variable of the spline was precipitation simulated by HadRM3P between 1971 and 2000.

To perform the interpolation, the values of the three independent variables and the one dependent variable need to be known at each of the RCM grid points supplied to the spline. The values of the two spatial independent variables were determined by simply converting the unrotated longitudes and latitudes of the RCM grid points into NZMG eastings and northings. The third independent variable — observed mean daily precipitation from 1971 to 2000 — was determined from points on the surface described in Section 4.1.2. This required the cropping of the RCM domain to 57 grid points ('•' sym-

bols in Figure 4.2) within the domain of the mean daily precipitation surface (outlined by the dotted line in Figure 4.2). Fourteen of these RCM grid points lie over ocean, making it necessary to sample values from the extrapolated section of the observed precipitation surface at these locations. The inclusion of these ocean-based points helps to limit the dependent variable to reasonable values at the boundaries of the primary study region.

The interpolation itself involves two main steps. The first step is to calculate the coefficients of the polynomials that link the breakpoints of the spline. These coefficients were calculated by the ANUSPLIN SPLINA program, using the values of the independent and dependent variables at the grid points of the RCM. Once the coefficients of the splined surface are defined, the value of the dependent variable over the domain of the spline has been defined as a function of the three independent variables.

The second step of the interpolation is to create a surface of the dependent variable — the simulated precipitation — on a 100 m regular grid (outlined by the dashed line in Figure 4.2) using the ANUSPLIN LAPGRD program. To perform this step, each independent variable must first be defined at all points on this regular grid. Grids of the spatial independent variables of easting and northing are easily calculated by the software. The grid of the third independent variable — observed mean daily precipitation from 1971 to 2000 — was constructed as per the methodology described in Section 4.1. Once the grids of the three independent variables are defined, the LAPGRD program can calculate the values of the dependent variable at all points on the same grid. This results in a high-resolution surface of simulated precipitation in the central Southern Alps. The assumption of this technique is that the precipitation at any given point in the central Southern Alps is a function of both its horizontal spatial position and the mean daily precipitation previously experienced at that location. This issue is discussed in Chapter 6.

4.3 Software

Most of the spatial and numerical analysis in this thesis was performed within IDL (Interactive Data Language) Version 7.0, a product developed by ITT
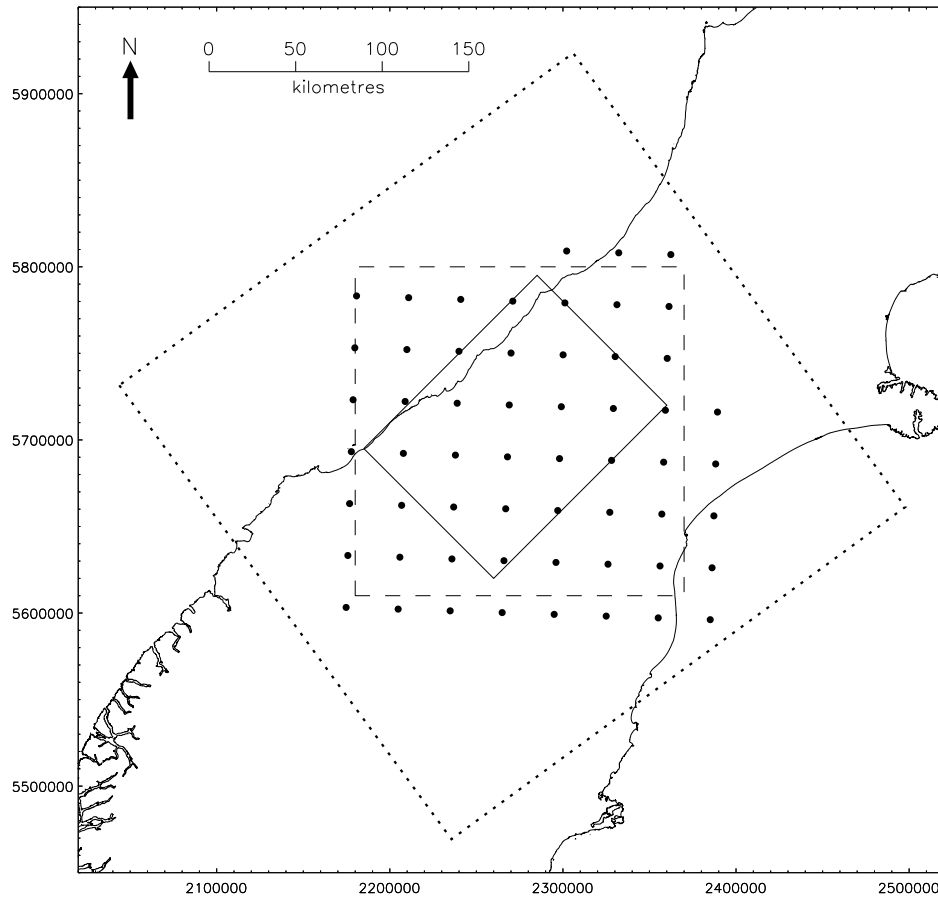
Figure 4.2 Domains and HadRM3P grid points used during the downscaling of simulated precipitation in the Southern Alps. The dotted line outlines the domain of the observed precipitation surface, which was produced by combining transects of observed precipitation from 1971 to 2000. '•' symbols denote HadRM3P grid points used during the downscaling. The region of downscaled HadRM3P precipitation is outlined by the dashed line. The primary study region is outlined by the tilted rectangle in the centre of the map.

Visual Information Solutions. The precipitation simulated by the HadRM3P regional climate model was interpolated and downscaled using version 4.36 of the ANUSPLIN software package (Hutchinson 2011). Some of the maps in this thesis were produced in ESRI© ArcGIS Version 9.3.1.

4.4   Summary

Observations from rain gauges across transects of the Southern Alps were interpolated to produce profiles of precipitation, which were subsequently combined into surfaces of observed precipitation. In order to downscale precipitation simulated by the HadRM3P regional climate model, these surfaces of observed precipitation were employed as independent variables within a trivariate thin-plate smoothing spline. The next chapter describes the results of this analysis.

Chapter 5

Results

A greater understanding of natural phenomena can be gained from both empirical analysis and dynamic modelling, but models cannot be developed without first observing physical interrelationships. This chapter initially focuses on the observed distribution of precipitation in the central Southern Alps, and its primary influences. Firstly, to assess the extent to which mean annual precipitation at any given location in the Southern Alps is directly correlated with the local topographic elevation, these two variables are very briefly compared. A two-dimensional approach is then adopted, in which profiles of observed precipitation are constructed, compared to atmospheric properties, and then combined to form surfaces of precipitation in the Southern Alps. In Sections 5.4 and 5.5, these surfaces are used as predictors of rainfall at fine spatial scales, via their employment as independent variables in the downscaling of precipitation simulated by the HadRM3P regional climate model. The downscaled surfaces are subsequently validated against observations, both during a 30-year period and on a single day.

5.1 Direct influence of topographic elevation upon precipitation

One of the initial objectives of this thesis is to identify the strongest influences upon the spatial distribution of precipitation in the Southern Alps. To
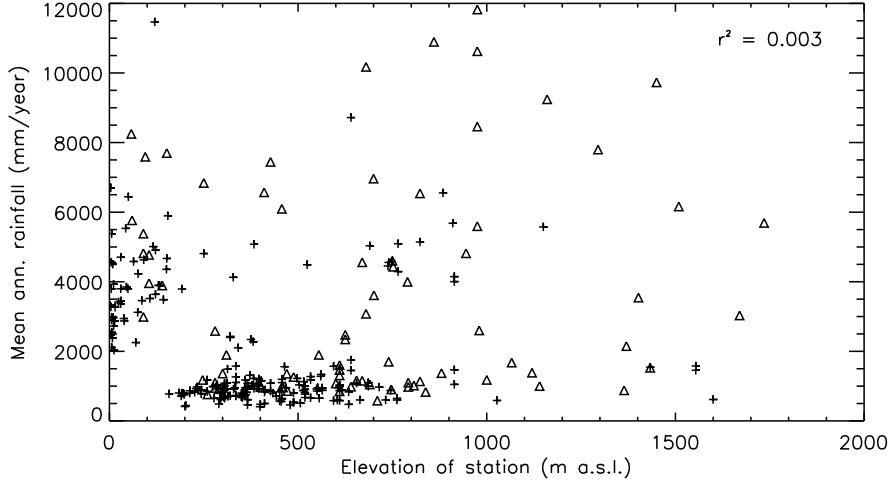
Figure 5.1 Mean annual precipitation (mm a^{-1}) observed at Southern Alps stations from 1971 to 2000, versus elevation of stations (m a.s.l.). '+' symbols denote CliDB gauges, '△' symbols denote WRA gauges.

this aim, the mean annual precipitation at each rain gauge was compared to its elevation above mean sea level (Figure 5.1). The spatial domain of this comparison was limited to the more mountainous area that extends from 20 km southeast of the study baseline, northwest to the Tasman Sea (Figure 3.1). One can see from Figure 5.1 that the WRA gauges ('△' symbols) have a wider range of both topographic elevation and recorded mean annual precipitation than the CliDB gauges ('+' symbols).

The direct correlation between local topographic elevation and precipitation observed by rain gauges is weak in the Southern Alps. The linear Pearson correlation coefficient (r) of observed mean annual precipitation versus elevation is 0.059 and the coefficient of determination (r^2) is only 0.003. Variations in the topographic elevation of rain gauges thus explain very little of the variation in mean annual precipitation observed at those gauges. It is therefore impossible to simply use local topographic elevation as an accurate means of downscaling long-term precipitation in the Southern Alps, and an alternative method is necessary.

5.2   Profiles of precipitation

This section describes two-dimensional profiles of mean annual precipitation observed in the Southern Alps during the 30-year period from 1971 to 2000. The profile of observed mean daily precipitation is subsequently compared to atmospheric properties and is classified by wind direction.

5.2.1   Mean annual profiles

Southern Alps transect

Figure 5.2a shows the mean annual precipitation observed at each gauge in the Southern Alps versus the distance of the gauge northwest of the study baseline. The curved line in Figure 5.2a is the line of 'best-fit', produced by the one-dimensional cubic spline, as described in Section 4.1.1. The Alpine Fault is located 85–87 km northwest of the baseline. As has been shown in previous studies, the distribution of precipitation exhibits a distinct profile across the Southern Alps. Around 2–4 m of precipitation is experienced by sites on the West Coast of the South Island each year. Moving southeastward, precipitation rises sharply, reaching 10–12 m a^{-1} at some stations located a few kilometres southeast of the Alpine Fault. The wettest gauges in this region are generally sourced from the WRA, vividly illustrating the value of these data. The spline fitted to the observations peaks at 9.0 m a^{-1}. The location of this peak is 78.1 km northwest of the baseline and 7–9 km southeast of the Alpine Fault. Continuing southeastward, precipitation drops to less than 1 m a^{-1} in the lee of the Southern Alps.

Separate profiles of mean annual precipitation were subsequently constructed across the northeast Hokitika, southwest Hokitika, Franz Josef, Haast and Milford transects. The locations of these transects within the South Island are shown in Figure 3.2. Details of individual gauges in each transect, including the amount of recorded mean annual precipitation, are listed in Appendix A.
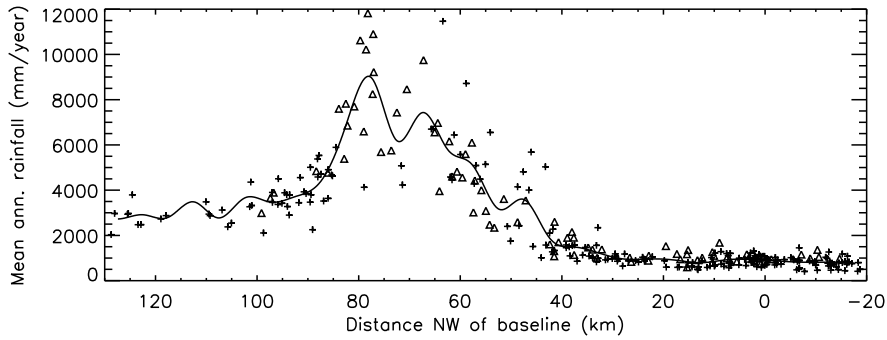
(a) Southern Alps
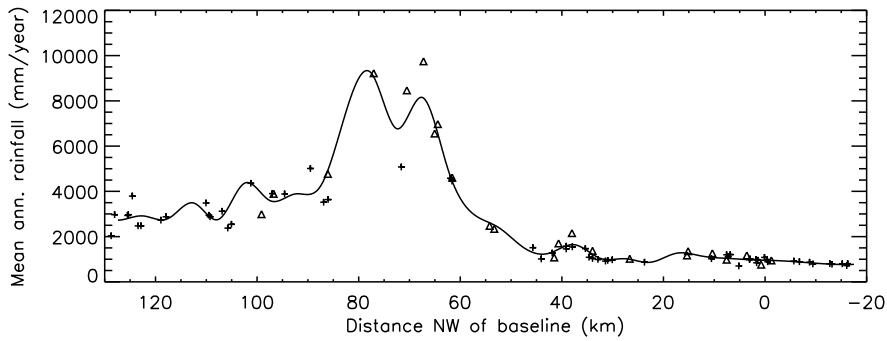
(b) Northeast Hokitika
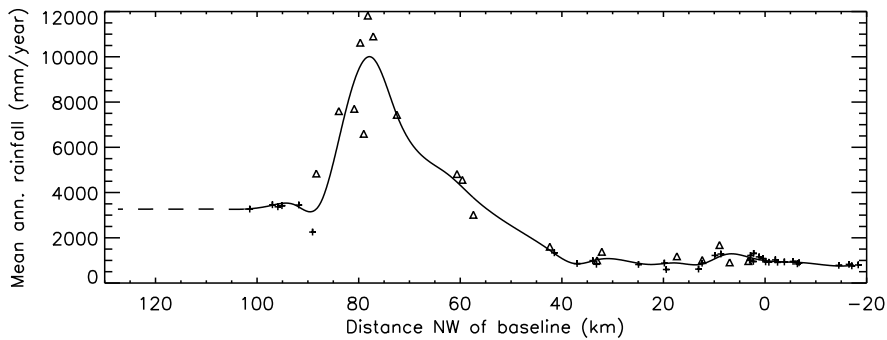
(c) Southwest Hokitika

Figure 5.2   Mean annual precipitation (mm a^{-1}) observed at Southern Alps stations from 1971 to 2000, versus distance northwest of baseline (km). '+' symbols denote CliDB gauges, '△' symbols denote WRA gauges. The curved line shows the cubic spline fitted to the profile. The dashed line represents extrapolated values, which are equal to the mean annual precipitation observed in the 5-km division at the northwestern tail of each profile.
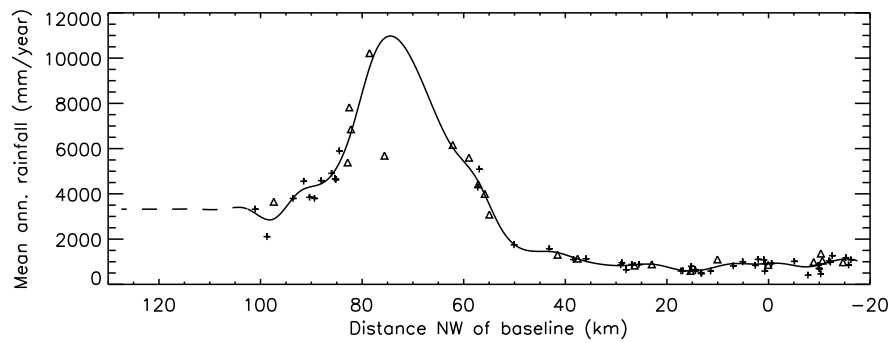
(d) Franz Josef
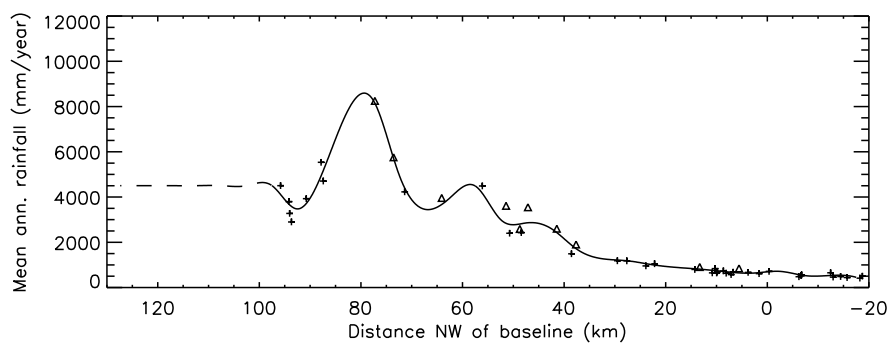
(e) Haast
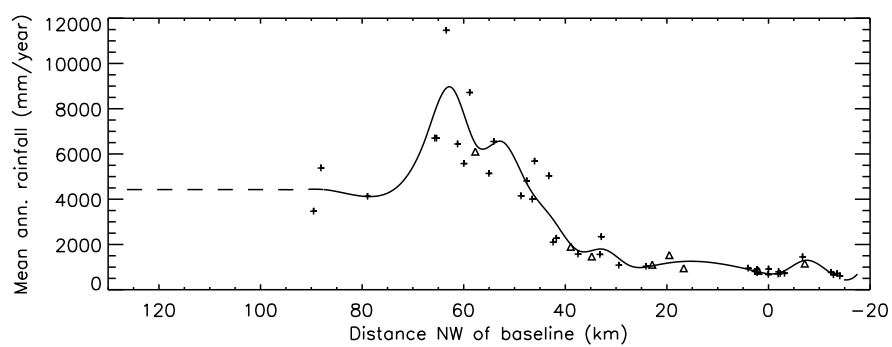
(f) Milford

Figure 5.2 (continued).

Northeast Hokitika transect

The spline fitted through the averaged divisions of the northeast Hokitika transect peaks at 9.4 m a^{-1} (Figure 5.2b). This maximum is located 78.4 km northwest of the baseline and 8 km southeast of the Alpine Fault. The location and magnitude of the peak is largely defined by the sole station within the 75–80 km division: Mount Browning (1160 m a.s.l.) at the head of the Styx River, where 9.2 m a^{-1} of precipitation was recorded. However, Cabot Ridge (1450 m a.s.l.), just east of the Wilberforce River and 67.2 km northwest of the baseline, is the individual station that recorded the maximum mean annual precipitation across the northeast Hokitika transect: 9.7 m a^{-1}. The spline through this transect has a second, smaller peak of 8.1 m a^{-1} at 67.7 km.

Southwest Hokitika transect

The spline through the southwest Hokitika transect peaks at 10.0 m a^{-1} (Figure 5.2c). This maximum is located 77.9 km northwest of the baseline and 7 km southeast of the Alpine Fault. The wettest 5-km division of the southwest Hokitika transect extends from 75–80 km northwest of the baseline. This division contains stations in the Tuke and Cropp catchments. However, one station within this division, Moonbeam Torrent (410 m a.s.l.) on the Waitaha River, recorded average precipitation of only 6.6 m a^{-1}.

Franz Josef transect

The wettest individual gauge within the Franz Josef transect is Luncheon Rock (680 m a.s.l.), near the lower tongue of the Franz Josef Glacier and 78.5 km northwest of the baseline (Figure 5.2d). 10.2 m a^{-1} of precipitation was recorded at Luncheon Rock during 3.7 years of observations between 1982 and 1986. Almer Hut (1735 m a.s.l.) lies just 3 km to the southeast, near the upper tongue of the Franz Josef Glacier. Only 5.7 m a^{-1} of precipitation was recorded at Almer Hut during 4.5 years of observation between 1991 and 1996.

No observations are recorded between Almer Hut and the next gauge to

the southeast, Panorama Ridge (1509 m a.s.l.) at the head of the Godley River. Panorama Ridge is 22 km to the east of Almer Hut, and the distance between these two stations along the northwest-southeast axis normal to the baseline is 13 km. 6.2 m a^{-1} of precipitation was recorded at Panorama Ridge over 7.0 station years.

Initially, all the stations in the Franz Josef transect were included in the interpolation, and the peak of the spline reached 8.2 m a^{-1}. This peak was located 74.4 km northwest of the baseline, 11 km southeast of the Alpine Fault and 4–5 km northwest of the Main Divide above the Franz Josef névé. Almer Hut was then removed from the interpolation and the spline was recalculated. The location of the peak of the spline remained at 74.4 km northwest of the baseline. However, the maximum magnitude of the spline with Almer Hut excluded was 10.9 m a^{-1} — an increase of 2.7 m a^{-1}. This illustrates the sensitivity of the spline to individual gauges located in data-sparse areas. Figure 5.2d shows the spline with Almer Hut excluded from the interpolation, but mean annual precipitation recorded at Almer Hut is still represented on the plot by the '△' symbol located at 75.6 km northwest of the baseline.

The available observations form a distinctly shaped profile across the Franz Josef transect, but observations of precipitation at Almer Hut appear to be anomalously low. A high proportion of the precipitation experienced at Almer Hut is likely to fall in the form of snow, due to the high elevation of the site. The combination of the reduced fall-velocity of snowflakes and deformation of the wind field around rain gauges can lead to significant undercatch of precipitation in exposed, highly elevated locations (Goodison et al. 1998). The low precipitation recorded at Almer Hut was suspected to be at least partially due to undercatch. Observations from Almer Hut were therefore excluded from the interpolation for the remainder of the analysis. With Almer Hut excluded, the peak of the spline through the Franz Josef transect (10.9 m a^{-1}) is higher than the peak of the spline through the other 4 transects. Measurements of snow accumulation on the Franz Josef Glacier appear to support this level of precipitation, as discussed in Chapter 6.

Haast transect

The spline through the Haast transect peaks at 8.6 m a^{-1} (Figure 5.2e). This peak is located 79.4 km northwest of the baseline, around 7 km southeast of the Alpine Fault. Of the 5 transects — northeast Hokitika, southwest Hokitika, Franz Josef, Haast and Milford — Haast has the lowest peak. The peak of the Haast profile is 2.3 m a^{-1} lower than that of the Franz Josef profile. The Haast region has lower topographic elevation than other parts of the Southern Alps. This may lead to reduced orographic uplift of air and explain the lower magnitude of precipitation across this transect. The wettest gauge across the Haast transect is Cron Creek (58 m a.s.l.), near the Haast River, which lies 77.3 km northwest of the baseline and 8 km southeast of the Alpine Fault. An average of 8.2 m a^{-1} of precipitation was observed at Cron Creek during 9.0 years of observation between 1991 and 2001. No stations are located in the 80–85 km interval of the Haast transect. The southeastern tail of the spline fitted through the Haast transect drops away at a lower rate than the tails of the other 4 transects. This gives some support to the low peak of the spline, since there may be more spillover of precipitation to compensate.

Milford transect

The wettest gauge in the Milford transect (Figure 5.2f) is Dumpling Hut (120 m a.s.l.). 11.5 m a^{-1} of precipitation was recorded at Dumpling Hut between 1982 and 1987, though the number of daily readings from this site equates to only 1.7 years of observation over this time. The spline through the Milford transect peaks at 9.0 m a^{-1}. This peak is located 62.8 km northwest of the baseline, 11.6 km southeast of the peak across the Franz Josef transect. The peaks of splines fitted to the northeast Hokitika, southwest Hokitika and Haast transects all lie yet further to the northwest. This could be partially due to the topography of the Milford region, where the Main Divide lies furthest to the southeast. However, there are large observational gaps in the profile through the Milford transect, with only 3 stations located more than 66 km northwest of the baseline. The observations are insufficient to describe
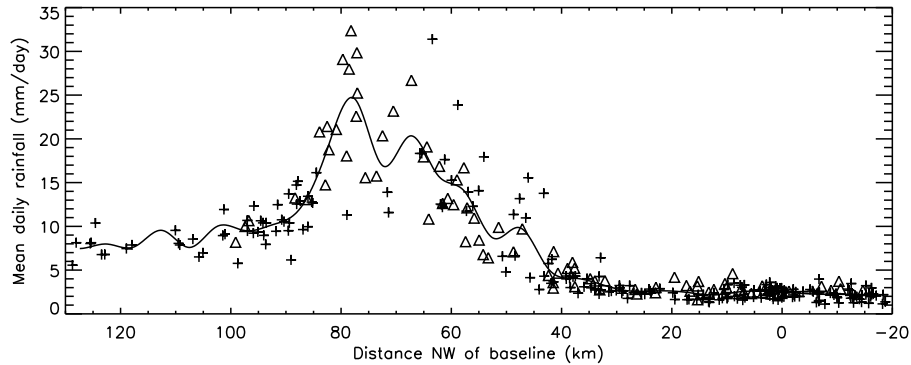
Figure 5.3 Mean daily precipitation (mm dy^{-1}) at Southern Alps stations from 1971 to 2000, versus distance northwest of baseline (km). '+' symbols denote CliDB gauges, '△' symbols denote WRA gauges. The curved line shows the cubic spline fitted to the profile.

the distribution of precipitation in this region, and the northwest section of the Milford profile must be viewed with caution.

5.2.2 Comparison of daily profiles with atmospheric properties

One of the basic aims of the methodology was to use the two-dimensional profile of orographically enhanced rainfall as a predictor of rainfall distribution at high spatial resolution. Since the profile of observed rainfall could be expected to vary under different atmospheric conditions, it was hypothesised that incorporating such variations of the profile might improve the skill of the downscaling method. The profile of mean daily precipitation across the Southern Alps on all days from 1 January 1971 to 31 December 2000 is shown in Figure 5.3. The shape of the daily profile is the same as that of the annual profile in Figure 5.2a, but the units of the ordinate axis are instead millimetres of precipitation per day (mm dy^{-1}).

Using data from NCEP/NCAR Reanalysis 1, the mean direction and magnitude of wind — diagnosed at 42.5° S 170° E, north of the central Southern Alps (see Figure 3.4) — was calculated on all days from 1 January 1971 to 31 December 2000. The direction and magnitude of the wind
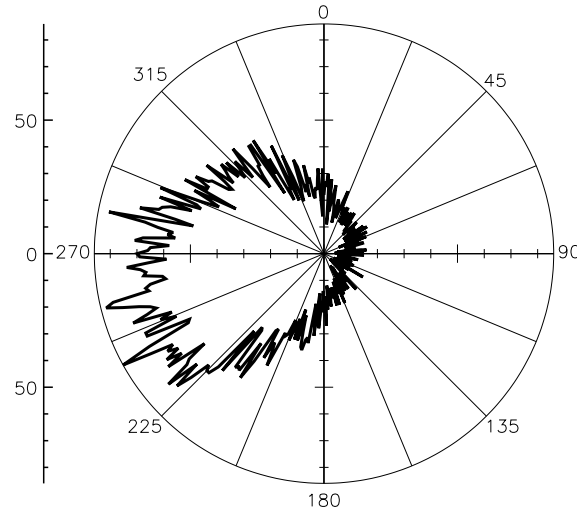
Figure 5.4 Frequency of mean daily wind direction at 850 hPa 42.5° S 170° E from 1 Jan 1971 to 31 Dec 2000 in NCEP/NCAR Reanalysis 1. Frequency is measured by the total number of days on which the mean horizontal wind direction blew from each 1° segment of the 360° compass.

in the horizontal plane was calculated via a vector sum of the zonal and meridional wind vectors at the 850 hPa pressure level. The resultant wind vectors were then rotated by 180° in the horizontal plane, so as to point in the source direction of the wind.

Figure 5.4 shows the frequency of mean daily wind direction at 42.5° S 170° E, at a height of 850 hPa. Westerlies are dominant at this height and location: the wind blows from the western half of the compass on 78.4% of all days from 1971 to 2000. The wind most commonly blows from the southwest (42.4% of days), west (50.8%) and northwest (36.0%) quadrants. Winds from the eastern half of the compass are infrequent (21.6%) and winds from the eastern quadrant are particularly rare (8.4%).

The source wind directions were initially categorised into 4 quadrants (90° segments) of the compass: northwest, northeast, southeast and southwest. Quadrants were used for simplicity; the use of smaller segments, such as 45° segments, would have necessitated a greater number of different wind-classifications, thereby complicating the downscaling process. An additional 4 quadrants were however used to analyse the relationships between precip-

itation and wind direction, but these were not used during the downscaling process. These additional 4 quadrants were: north, east, south and west, each with quadrant again forming a 90° segment of the compass.

The profile of daily precipitation across the Southern Alps was then categorised by the quadrant from which the wind blew on each UTC day. The profile of precipitation across the Southern Alps varies considerably during different wind directions (Figure 5.5). The greatest amount of precipitation falls on days during which the wind blows from the northwest, north and west quadrants. The highest precipitation is experienced on 'northwesterly days', when the spline fitted through the transect of observations peaks at 53.2 mm dy^{-1}. When the wind blows from the southwest, west, northwest, north or northeast quadrant, the average location of peak precipitation is 77–81 km northwest of the study baseline, that is, on the northwest flank of the Southern Alps.

The peak precipitation of the spline across the Southern Alps is lowest on days when the wind blows from the south (3.1 mm dy^{-1}), southeast (4.3 mm dy^{-1}) and east (4.2 mm dy^{-1}) quadrants. Wind from these quadrants produces a very flat distribution of precipitation. The average location of peak precipitation on such days is on the southeast side of the Southern Alps, approximately 5 km northwest of the baseline. This is around 72–75 km southeast of the peak that occurs on days the wind blows from the other quadrants.

Air temperature and specific humidity from NCEP/NCAR Reanalysis 1 were also analysed. Table 5.1 presents a summary of atmospheric variables and precipitation, classified according to the source direction of the mean daily wind at 42.5° S 170° E. Mean air temperature, specific humidity and peak precipitation are all highest on days when the wind blows from the north and northwest quadrants. Conversely, these properties are all lowest when the wind blows from the south quadrant. Mean wind magnitude is strongest on days when wind blows from the west (9.7 m s^{-1}) and northwest (9.4 m s^{-1}) quadrants, and is weakest when wind blows from the east (5.1 m s^{-1}) quadrant.

The distribution of precipitation across the Southern Alps was also clas-
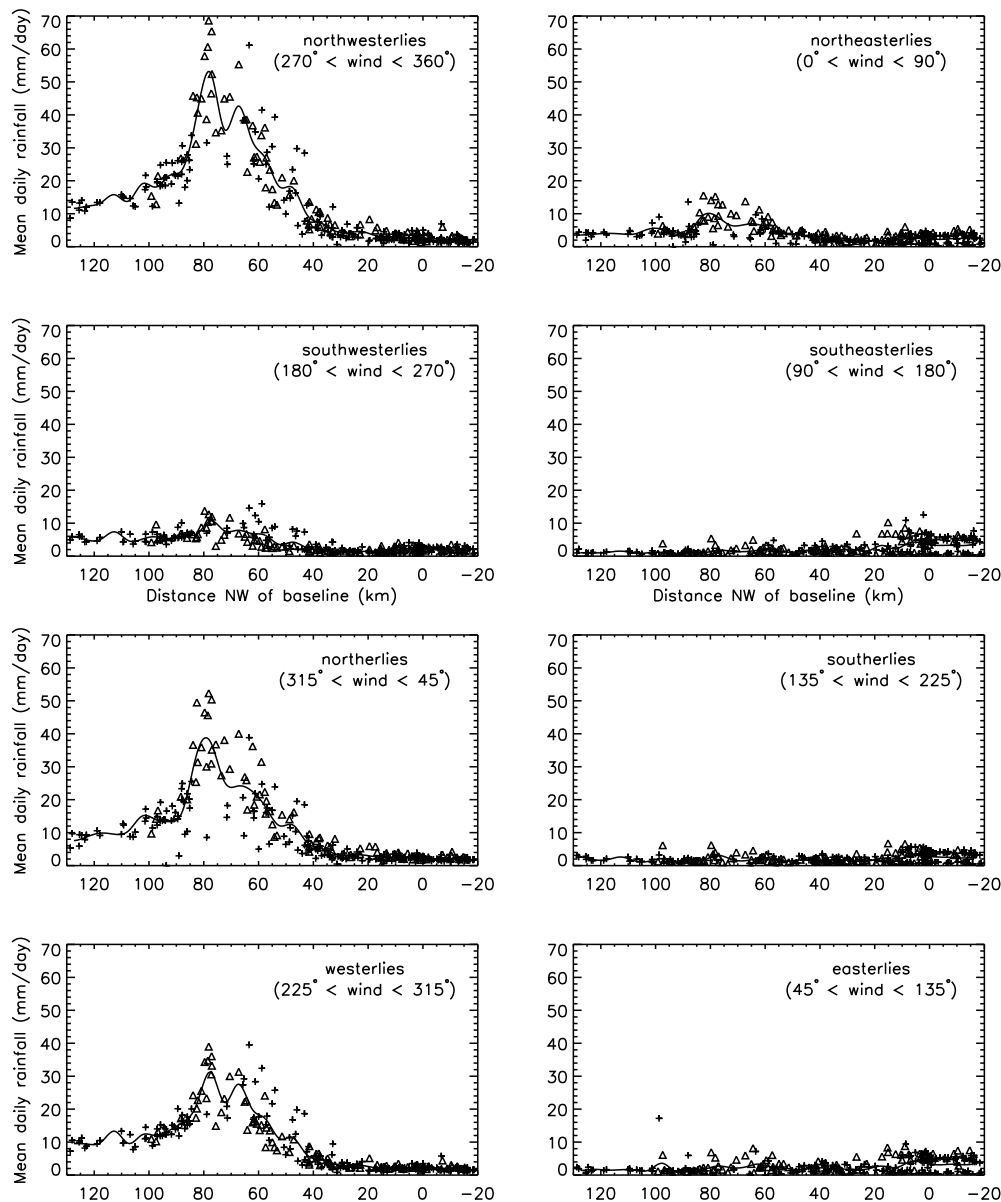
Figure 5.5 Mean daily precipitation (mm dy^{-1}) observed at Southern Alps stations from 1971 to 2000, versus distance northwest of baseline (km), categorised by wind direction at 850 hPa 42.5° S 170° E. '+' symbols denote CliDB gauges, '△' symbols denote WRA gauges. The curved line shows the cubic spline fitted to each profile.

Table 5.1 Atmospheric properties and observed precipitation in the Southern Alps from 1 Jan 1971 to 31 Dec 2000. Wind, air temperature and specific humidity are taken from 850 hPa 42.5° S 170° E in NCEP/NCAR Reanalysis 1. Precipitation was observed by rain gauges located in the Southern Alps. All data are categorised by the source direction of the mean daily wind in the horizontal plane. [Column 1] quadrant from which the wind originates, and in parentheses, the minimum and maximum bearings that enclose the quadrant; [2] mean magnitude of the sum of the zonal and meridional mean daily wind velocities ($|\overline{u + v}|$); [3] mean daily air temperature ($\overline{T}$); [4] mean daily specific humidity ($\overline{q}$); [5] maximum value of spline fitted to the profile of observed precipitation across the Southern Alps (p_{max}); [6] distance from the study baseline northwest to the location of p_{max} (NW Dist.); [7] number of days on which the wind blew from within the quadrant; [8] number of days on which the wind blew from within the quadrant, expressed as a percentage of the total number of days from 1 Jan 1971 to 31 Dec 2000.

Wind		$\overline{T}$	$\overline{q}$	Precipitation		Days	
Quadrant	$\lvert\overline{u+v}\rvert$			p_{max}	NW Dist.		
(Min. °, Max. °)	(m s^{-1})	(°C)	(g kg^{-1})	(mm dy^{-1})	(km)	Num.	(%)
Northwest (270, 360)	9.4	6.5	5.0	53.2	78.1	3947	36.0
Northeast (0, 90)	6.4	5.0	4.6	10.1	80.6	1356	12.4
Southwest (180, 270)	8.9	3.2	3.6	10.7	77.3	4647	42.4
Southeast (90, 180)	5.3	2.3	3.4	4.3	5.5	1008	9.2
North (315, 45)	8.1	6.5	5.3	38.8	79.2	2269	20.7
South (135, 225)	7.1	1.8	3.3	3.1	5.3	2213	20.2
West (225, 315)	9.7	5.0	4.2	31.2	77.7	5567	50.8
East (45, 135)	5.1	3.7	4.0	4.2	5.1	925	8.4

sified by air temperature and specific humidity. However, the distinctions
between the different precipitation profiles under such classifications were
not as clear as those under classification by wind direction. On days during
which the mean air temperature at 850 hPa 42.5° S 170° E was less than
0 °C, the spline fitted to the transect of precipitation observations reached
a peak of just 6.7 mm dy^{-1}, 77.0 km NW of the baseline. However, the
reduced air temperature and precipitation were accompanied by a notable
change of the source wind direction toward the south. Thus to some extent
air temperature appears to be a proxy for wind direction.

To further analyse the influence of air temperature, observations were lim-
ited to days on which the 850 hPa wind blew from the northwest quadrant
and the 850 hPa mean air temperature was less than or equal to 0 °C (Fig-
ure 5.6). The introduction of the upper temperature limit of 0 °C reduces the
peak precipitation of the spline on northwesterly days from 53.2 mm dy^{-1}
to 21.6 mm dy^{-1}. Much of this reduction is likely to be due to the lower
humidity of cold air. The location of the peak remains on the northwest
flank of the Southern Alps, moving from 78.1 km to 79.4 km northwest of
the baseline. A marked relationship between air temperature and spillover
of precipitation southeast of the Main Divide is not obvious. However, the
highest levels of precipitation are recorded at gauges southeast of the Main
Divide, and precipitation is more evenly distributed in the centre of the pro-
file. This could be caused by an increase in the southeastward drift of ice
crystals during temperatures below freezing.

In order to investigate the influence of varying amounts of atmospheric
moisture upon the distribution of precipitation, the observations of precipi-
tation were classified by the amount of specific humidity at 850 hPa 42.5° S
170° E, with no limitation of wind direction or air temperature. The mag-
nitude of the precipitation profile across the Southern Alps had a strong,
positive correlation with the amount of specific humidity. However, varia-
tions in specific humidity did not correlate with changes in the location of
peak precipitation to any great extent. Air temperature correlated positively
with specific humidity.

Due to the covariances between wind direction, air temperature and spe-
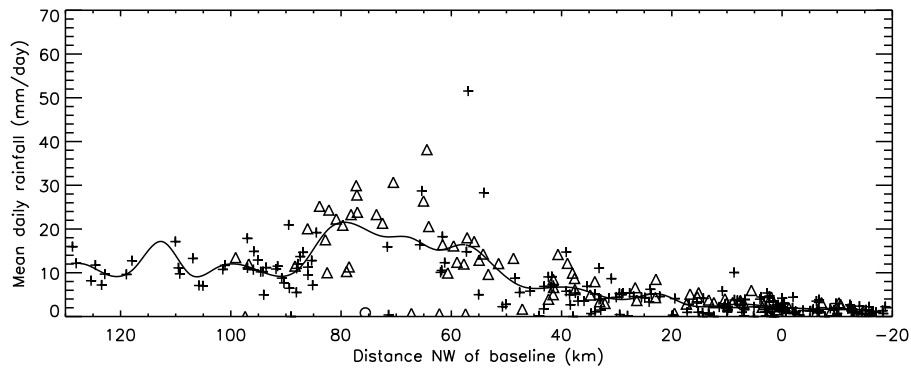
Figure 5.6 Mean daily precipitation $(mm\ dy^{-1})$ in the Southern Alps on northwesterly days with 850 hPa temperature less than or equal to 0 °C, from 1971 to 2000, versus distance northwest of baseline (km). '+' symbols denote CliDB gauges, '△' symbols denote WRA gauges. The curved line shows the cubic spline fitted to the profile.

cific humidity, it was difficult to isolate the effect of any one of these variables upon the spatial distribution of precipitation in the Southern Alps. However, classification by wind direction produced the most distinct changes in the mean profile of rainfall. The wind-based classifications were therefore incorporated into the downscaling of precipitation simulated by the RCM in the Southern Alps.

5.3 Surfaces of observed precipitation

Surfaces of observed precipitation in the Southern Alps, constructed from the interpolated precipitation profiles, are described in this section. A new 30-year mean annual surface is compared with precipitation surfaces that have been independently developed by other researchers. The accuracy of the new 30-year surface is further assessed by its use within a model simulation of glacial flow in the central Southern Alps. Surfaces of mean daily precipitation, classified by wind direction, are then analysed.

5.3.1   Surface of mean annual precipitation

The five two-dimensional transects of precipitation observed across the Southern Alps (northeast Hokitika, southwest Hokitika, Franz Josef, Haast and Milford, see Figure 5.2) were combined into a three-dimensional surface that extends across much of the South Island, as described in Section 4.1.2. Figure 5.7 is an oblique aerial view of this surface, hereafter referred to as $Surf_{Obs.A}$. The surface in this image extends from 300 to 500 km northeast of the domain origin in Cape Providence, and from 20 km southeast of the baseline northwest to the Tasman Sea. This area encompasses all but the southwestern tip of the primary study region. The profile of precipitation across the Southern Alps is the dominant feature of the three-dimensional surface, as one would expect given the methodological approach of joining the two-dimensional transects. The ridge of peak rainfall along the axis of the Southern Alps is clearly visible, as is the rain shadow on the southeast side of the mountain range. Moving southwestward along the ridge, the surface initially rises a little and then dips significantly.

A plan view of $Surf_{Obs.A}$ within the primary study region is shown in Figure 5.8. The surface peaks at 10.9 m a^{-1} on the northwest flank of the central Southern Alps, around 74 km northwest of the baseline and approximately 11 km southeast of the Alpine Fault. The single maximum value of the surface is 10.93 m a^{-1}, on the upper region of the Fritz Range, which separates the Franz Josef and Fox glaciers. The location of this maximum is around 4 km northwest of the Main Divide, immediately northwest of the Pukaki catchment. In the context of the interpolative process, the location of peak precipitation is due to two factors. Firstly, of the 5 transects across the Southern Alps (northeast Hokitika, southwest Hokitika, Franz Josef, Haast and Milford), the magnitude of the interpolated profile was highest across the Franz Josef transect (10.9 m a^{-1}, see Figure 5.2d). Secondly, the Franz Josef profile was georeferenced so as to bisect the domain of the Franz Josef transect (Figure 4.1), and this bisecting line intersects the Franz Josef Glacier itself.

Throughout the central Southern Alps, the ridge of maximum precipitation in $Surf_{Obs.A}$ is generally around 6–10 km southeast of the Alpine Fault.
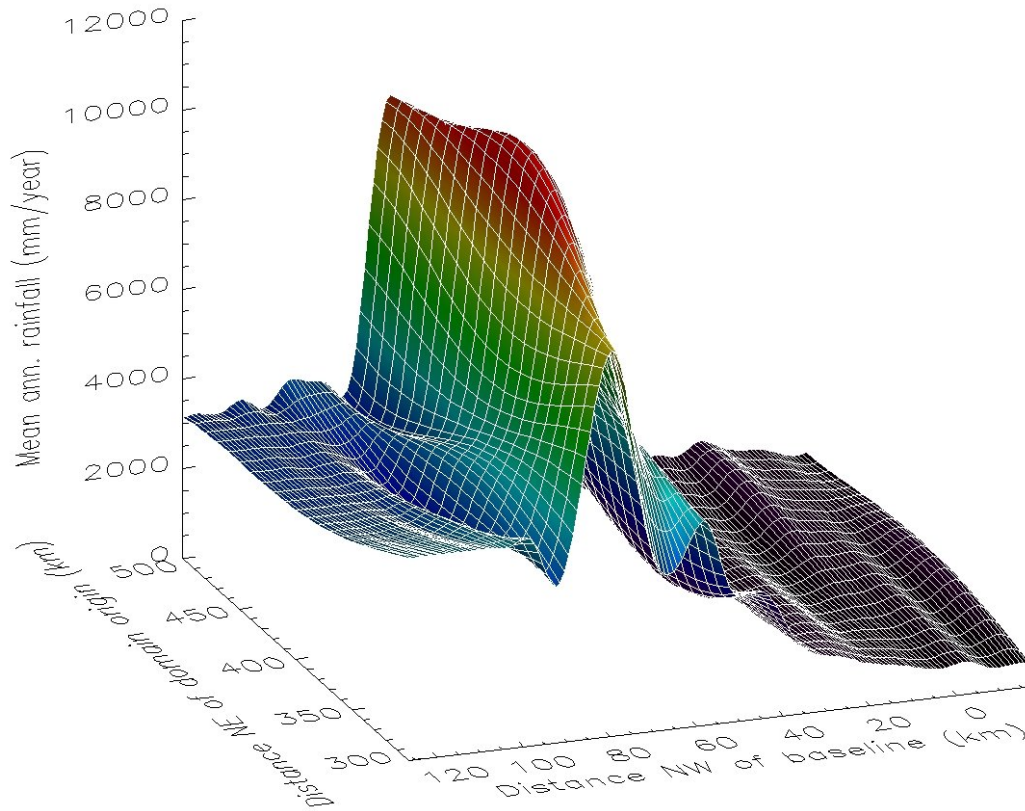
Figure 5.7 An oblique aerial view of the surface of observed mean annual precipitation (mm a^{-1}) in the central Southern Alps from 1971 to 2000 (Surf$_{\mathrm{Obs.A}}$). The x-axis is the distance (km) northwest of the study baseline, the y-axis is the distance (km) northeast of the domain origin in Cape Providence, and the z-axis is mean annual precipitation (mm a^{-1}).

Figure 5.8 Isohyets of interpolated observations of mean annual precipitation (mm a^{-1}) in the central Southern Alps from 1971 to 2000 (Surf$_{\mathrm{Obs.A}}$). The dashed line delineates the primary study region, within which Pukaki catchment is outlined. Shading indicates topographic elevations from a 500 m DEM.

Due to the deformation of the main topographic ridge along the Southern Alps, the distance from the precipitation ridge to the Main Divide is more variable, ranging from just 4 km in the Franz Josef region, to a maximum of around 25 km in the Haast region, where the Main Divide lies further to the southeast.

Comparison with other precipitation surfaces

Scientists at the Antarctic Research Centre currently use a surface of mean annual precipitation in their simulations of the mass balance and flow of glaciers in the Southern Alps. Dr Brian Anderson, of the ARC, derived a precipitation surface ($Surf_{Obs.BA}$) from 'invariant' orographic profiles of mean annual rainfall across the Southern Alps, which were subjectively estimated by Henderson and Thompson (1999). The magnitude of the profile of rainfall was slightly reduced during the construction of $Surf_{Obs.BA}$.

Dr Nick Golledge, a Post-Doctoral Fellow working with Dr Andrew Mackintosh at the ARC, compared $Surf_{Obs.BA}$ to $Surf_{Obs.A}$ within the domain of the Parallel Ice Sheet Model (PISM), which encompasses the central region of the Southern Alps. Figure 5.9 shows contours of the differences between the mean annual precipitation of the two surfaces in this region. The area of greatest difference lies on the northwest flank of the Southern Alps, northwest of the Pukaki catchment. In part of this region, $Surf_{Obs.A}$ is over 3.0 m a^{-1} wetter than $Surf_{Obs.BA}$. $Surf_{Obs.A}$ is around 1.5–2.5 m a^{-1} wetter than $Surf_{Obs.BA}$ in the northern part of Pukaki catchment, and around 1.5 m a^{-1} wetter than $Surf_{Obs.BA}$ at the head of the Tekapo catchment. To the southeast of the Main Divide, $Surf_{Obs.A}$ is generally 0–0.5 m a^{-1} drier than $Surf_{Obs.BA}$.

Figure 5.10 compares $Surf_{Obs.A}$ with two precipitation surfaces produced by Kerr (2009). These surfaces comprise estimated mean annual measured precipitation ($Surf_{Obs.TK.M}$) and estimated mean annual 'true' precipitation ($Surf_{Obs.TK.T}$) in the Pukaki catchment from 1971 to 2000. The surfaces were compared at a horizontal spatial resolution of 1 km x 1 km. Throughout most of the Pukaki catchment, mean annual precipitation in $Surf_{Obs.A}$ is within 1.0 m a^{-1} of both $Surf_{Obs.TK.M}$ and $Surf_{Obs.TK.T}$. Across the whole catchment, the root mean square errors of the 1-km grid cells of $Surf_{Obs.A}$,
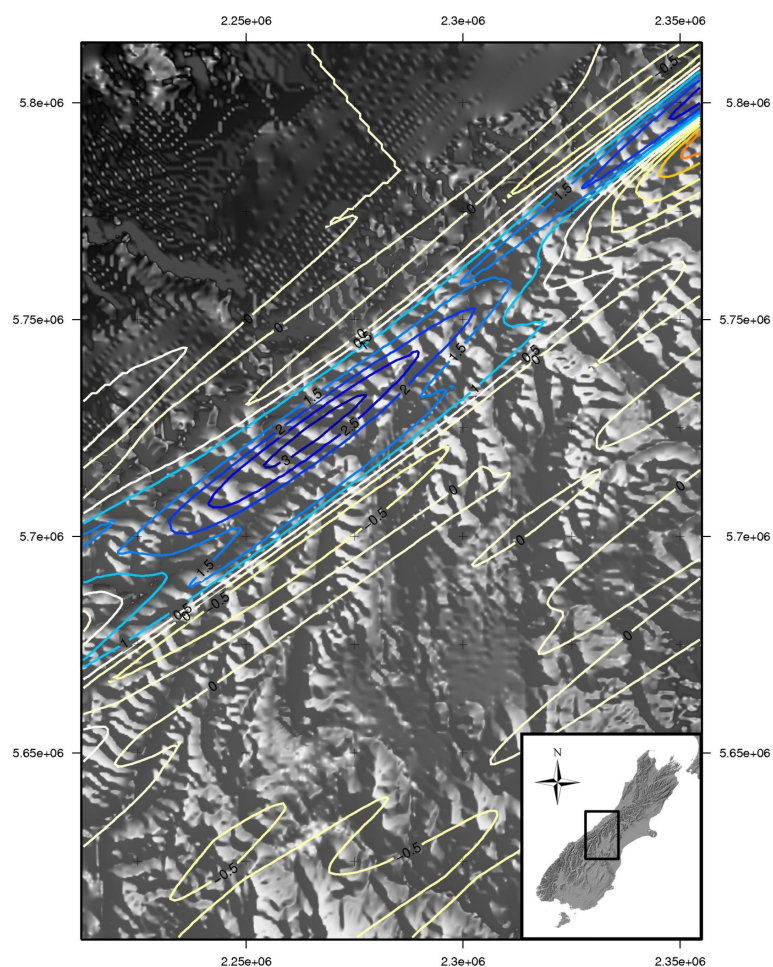
Figure 5.9   Contours of differences in mean annual precipitation $(m\ a^{-1})$ in the central Southern Alps: $\text{Surf}_{\text{Obs.A}}$ minus $\text{Surf}_{\text{Obs.BA}}$. Blue contours with positive values indicate regions in which $\text{Surf}_{\text{Obs.A}} > \text{Surf}_{\text{Obs.BA}}$; warm-coloured contours with negative values indicate regions in which $\text{Surf}_{\text{Obs.A}} < \text{Surf}_{\text{Obs.BA}}$. Image produced by Dr Nick Golledge of the Antarctic Research Centre, Victoria University of Wellington, New Zealand.

(a) Surf$_{\mathrm{Obs.A}}$ minus Surf$_{\mathrm{Obs.TK.M}}$ (b) Surf$_{\mathrm{Obs.A}}$ minus Surf$_{\mathrm{Obs.TK.T}}$
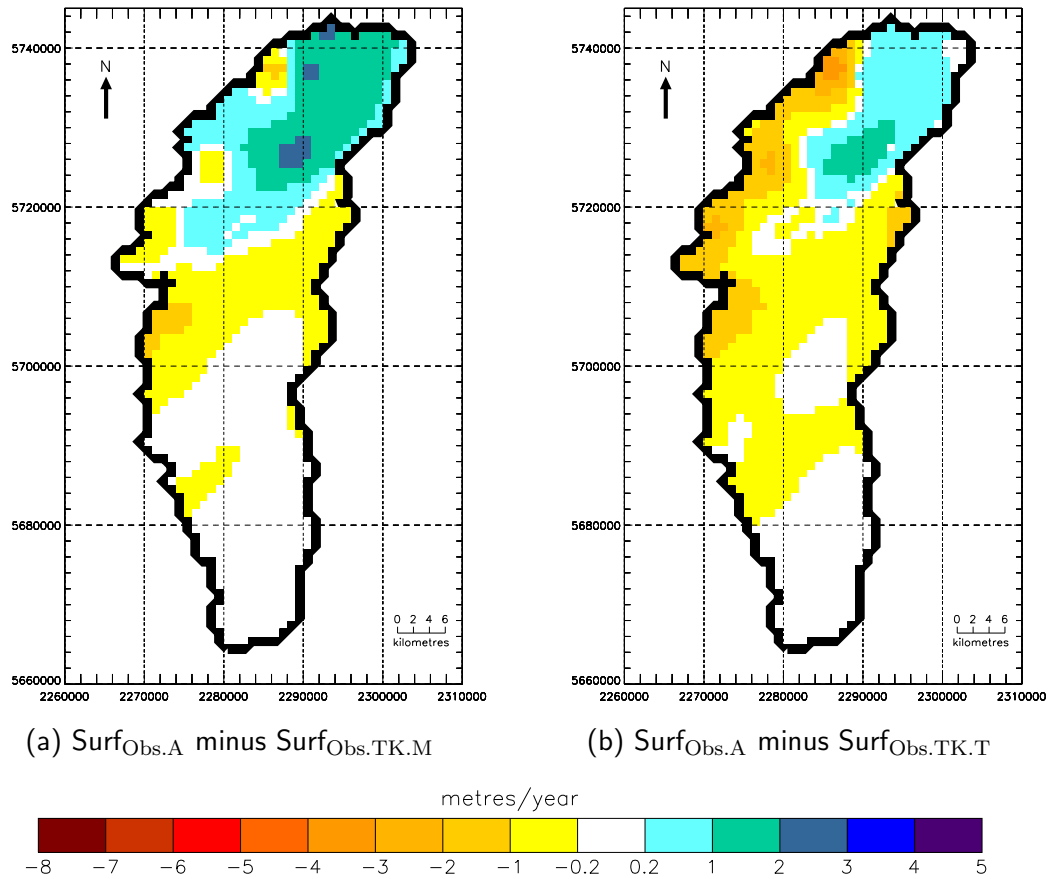
Figure 5.10 Differences in mean annual precipitation (m a^{-1}) in the Pukaki catchment from 1971 to 2000: Surf$_{\mathrm{Obs.A}}$ minus Surf$_{\mathrm{Obs.TK.M}}$ (left image), and Surf$_{\mathrm{Obs.A}}$ minus Surf$_{\mathrm{Obs.TK.T}}$ (right image). Surf$_{\mathrm{Obs.TK.T}}$ is estimated 'true' precipitation, which takes into account the estimated undercatch by rain gauges; Surf$_{\mathrm{Obs.TK.M}}$ does not consider undercatch. Cool colours indicate regions in which Surf$_{\mathrm{Obs.A}}$ > Surf$_{\mathrm{Obs.TK.M}}$ and Surf$_{\mathrm{Obs.A}}$ > Surf$_{\mathrm{Obs.TK.T}}$; warm colours indicate regions in which Surf$_{\mathrm{Obs.A}}$ < Surf$_{\mathrm{Obs.TK.M}}$ and Surf$_{\mathrm{Obs.A}}$ < Surf$_{\mathrm{Obs.TK.T}}$. Both Surf$_{\mathrm{Obs.TK.M}}$ and Surf$_{\mathrm{Obs.TK.T}}$ were produced by Kerr (2009).

validated against $\text{Surf}_{\text{Obs.TK.M}}$ and $\text{Surf}_{\text{Obs.TK.T}}$, are 0.7 m a^{-1} and 0.8 m a^{-1}, respectively. $\text{Surf}_{\text{Obs.A}}$ is generally around 0.2–2.0 m a^{-1} wetter than both $\text{Surf}_{\text{Obs.TK.M}}$ and $\text{Surf}_{\text{Obs.TK.T}}$ in the northeast part of the catchment.

$\text{Surf}_{\text{Obs.A}}$ is up to 4.0 m a^{-1} drier than $\text{Surf}_{\text{Obs.TK.T}}$ on the northwest edge of the Pukaki catchment. This is due to the extremely steep horizontal precipitation gradient and high levels of precipitation in the very northwest region of $\text{Surf}_{\text{Obs.TK.T}}$, which are not represented to the same extent in $\text{Surf}_{\text{Obs.A}}$. Variations between the surfaces from Kerr (2009) and the surface produced in the present analysis are due to the different interpolative techniques and data used in their construction. While $\text{Surf}_{\text{Obs.A}}$ was constructed via a spline of a series of transects, $\text{Surf}_{\text{Obs.TK.M}}$ and $\text{Surf}_{\text{Obs.TK.T}}$ were produced by a direct two-dimensional interpolation of precipitation observed at rain gauges, via ordinary kriging. $\text{Surf}_{\text{Obs.TK.M}}$ and $\text{Surf}_{\text{Obs.TK.T}}$ include additional observations from high-elevation gauges that were not present among the data used to build $\text{Surf}_{\text{Obs.A}}$, and $\text{Surf}_{\text{Obs.TK.T}}$ also takes into account the amount of estimated undercatch. Kerr (2009) focused primarily on the Pukaki catchment — a much smaller region than that covered by $\text{Surf}_{\text{Obs.A}}$ — and $\text{Surf}_{\text{Obs.TK.M}}$ and $\text{Surf}_{\text{Obs.TK.T}}$ are likely to be more accurate representations of the true distribution of precipitation in this catchment. However, the overall similarities between $\text{Surf}_{\text{Obs.A}}$ and the Kerr (2009) surfaces indicate that $\text{Surf}_{\text{Obs.A}}$ provides a reasonably good representation of mean annual precipitation in the Pukaki catchment, and suggests that $\text{Surf}_{\text{Obs.A}}$ may provide a similarly good description of precipitation over the wider region of the central Southern Alps.

Use of precipitation surface within the Parallel Ice Sheet Model

Another way to assess the quality of a precipitation surface is to examine its performance within an independently developed model of palaeoclimatic processes. Dr Nick Golledge of the ARC currently uses the Parallel Ice Sheet Model to simulate the flow and extent of glaciers in the Southern Alps during the last 40,000 years. The precipitation fed into the glacial model is a single mean annual surface, which is then temporally divided into equal amounts according to the timestep of the model. In early simulations using other

precipitation surfaces, the simulated extent of glaciers on the southeast side of the Southern Alps did not match geological evidence: the simulated ice did not extend far enough to the south.

Figure 5.11 shows the flux and extent of glacial ice in the central Southern Alps, as simulated by the PISM under possible cooling of 5–6 °C during the Last Glacial Maximum (LGM). This simulation uses the $Surf_{Obs.A}$ surface of observed precipitation, with the magnitude of the precipitation uniformly reduced by 50%. It was not possible to simulate the mapped ice extent without this reduction in precipitation. A decrease in precipitation at the LGM is consistent with suggestions from the second phase of the Palaeoclimate Modelling Intercomparison Project (PMIP2) (Rojas et al. 2009). The horizontal spatial resolution of $Surf_{Obs.A}$ was set to 1 km, which is the resolution of the PISM grid. The white lines delineate historical glacial extents inferred from geological evidence, provided courtesy of David Barrell from the Institute of Geological and Nuclear Sciences in New Zealand.

In Figure 5.11, the overall extent of simulated ice compares well to geological evidence, though the simlated ice extends a little beyond its geologically-estimated boundaries in some areas northwest of the Main Divide. On the southern side of the Southern Alps, the tongues of ice stretch south to the estimated extents in the Ohau, Pukaki and Tekapo catchments. This particular image is a snapshot in time rather than a scenario of glacial equilibrium. The domain of the PISM has subsequently been enlarged so as to encompass the whole of the South Island; this precludes the use of $Surf_{Obs.A}$ in further simulations. However, the improved correlation between simulated glacial extents and those inferred from geological evidence suggests that $Surf_{Obs.A}$ provides a more accurate representation of mean annual precipitation in the central Southern Alps than previous surfaces.

5.3.2 Surfaces of mean daily precipitation, categorised by wind direction

The profile of mean daily precipitation across the Southern Alps, on all days from 1 January 1971 to 31 December 2000 (Figure 5.3), was split into the
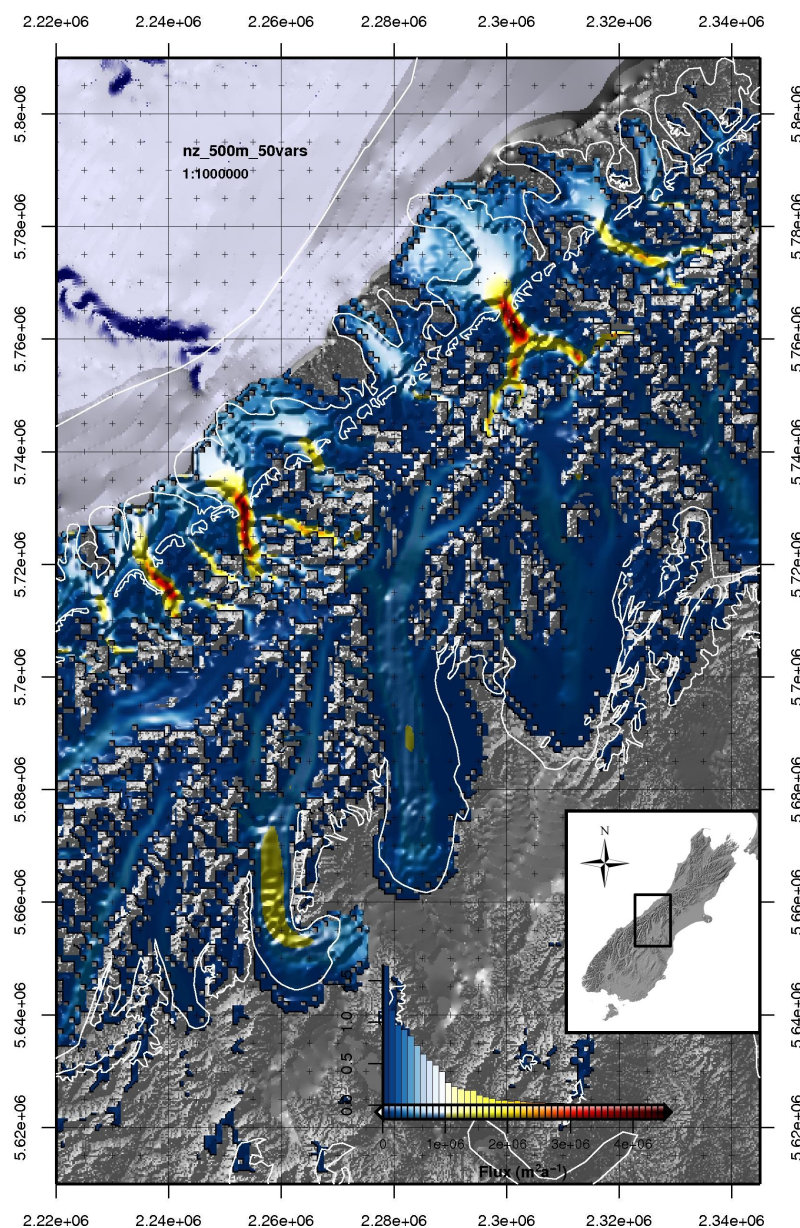
Figure 5.11   Snapshot of the flux $(m^2 \ a^{-1})$ and extent of glacial ice in the central Southern Alps, as simulated by the Parallel Ice Sheet Model under possible LGM cooling of 5–6 °C. The simulation uses the $Surf_{Obs.A}$ surface of observed precipitation, with the magnitude of the precipitation uniformly reduced by 50%. The white lines delineate glacial extents inferred from geological evidence, provided courtesy of David Barrell from the Institute of Geological and Nuclear Sciences in New Zealand. Image produced by Dr Nick Golledge of the Antarctic Research Centre, Victoria University of Wellington, New Zealand.

5 transects of northeast Hokitika, southwest Hokitika, Franz Josef, Haast and Milford. These 5 daily transects were interpolated, again via a two-dimensional tensor-product B-spline, to produce a surface of mean daily precipitation in the Southern Alps from 1971 to 2000 ($Surf_{Obs.D}$, Figure 5.12). The spatial distribution of $Surf_{Obs.D}$ is the same as that of the annual surface $Surf_{Obs.A}$ (Figure 5.8), but the units of the daily surface are millimetres of precipitation per day (mm dy^{-1}), rather than millimetres of precipitation per annum (mm a^{-1}). The northwest flank of the Southern Alps, northwest of the Pukaki catchment, experiences on average over 25 mm of precipitation each day. Mean daily precipitation peaks at just under 30 mm dy^{-1} on the upper region of the Fritz Range, between the Franz Josef and Fox glaciers.

The wind-classified profiles of mean daily precipitation in the Southern Alps (Figure 5.5) were each split into the 5 transects of northeast Hokitika, southwest Hokitika, Franz Josef, Haast and Milford. These wind-classified daily transects were then interpolated to produce wind-classified surfaces of daily precipitation in the Southern Alps from 1971 to 2000. The surface of mean daily precipitation on northwesterly days ($Surf_{Obs.D.NW}$) is shown in Figure 5.13.

The spatial pattern of precipitation in the central Southern Alps on northwesterly days is generally similar to the spatial pattern of precipitation on all days. $Surf_{Obs.D.NW}$ peaks in essentially the same place as $Surf_{Obs.D}$: on the upper northwest flank of the Southern Alps, near the Franz Josef and Fox glaciers. The similarities are unsurprising: since most of the annual precipitation in the Southern Alps falls on northwesterly days (see Figure 5.5 and Table 5.1), one would expect the annual climatology to be biased toward the northwesterly climatology. However, the magnitude of precipitation on northwesterly days is considerably higher than on all days, with $Surf_{Obs.D.NW}$ peaking at 65 mm dy^{-1} on the upper regions of the Franz Josef and Fox glaciers. Another point of difference is that the horizontal precipitation gradient on northwesterly days is much steeper than on all days, as indicated by the tightly grouped 5-mm dy^{-1} isohyets in Figure 5.13. This is consistent with the increased precipitation one would expect from warmer, moister air encountering the mountains at an angle approximately perpendicular to the
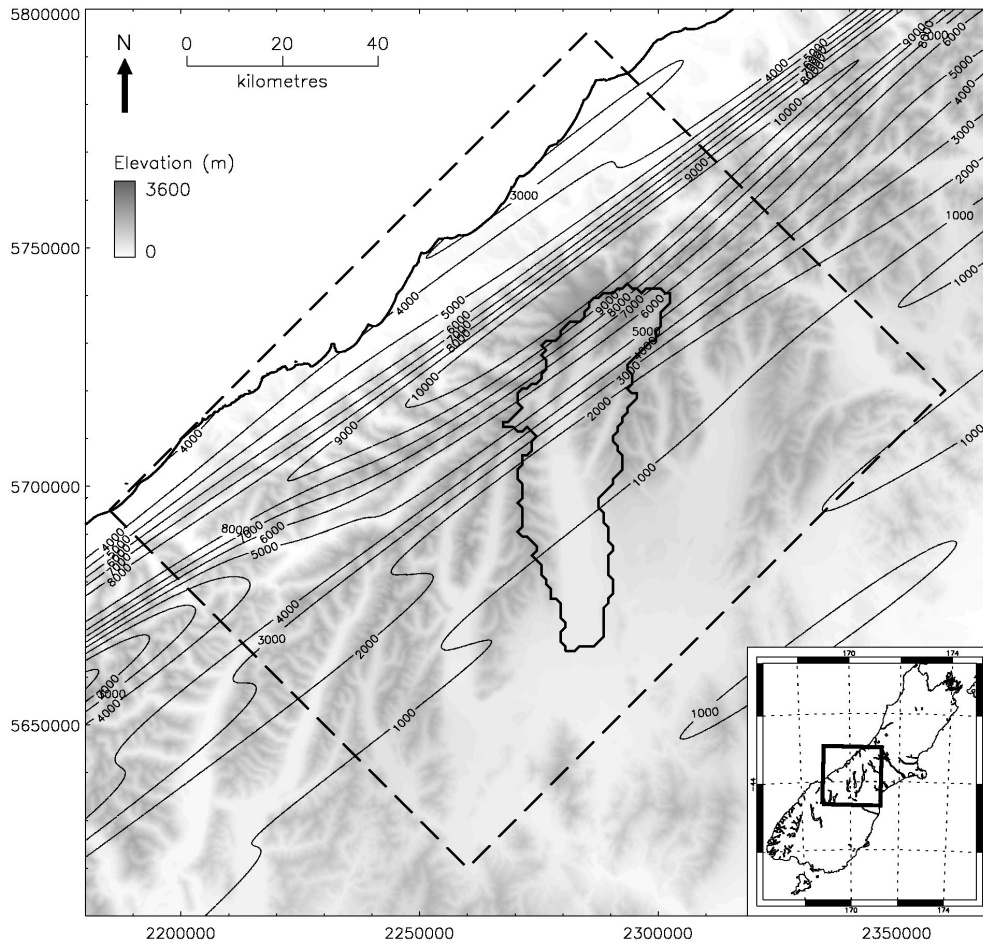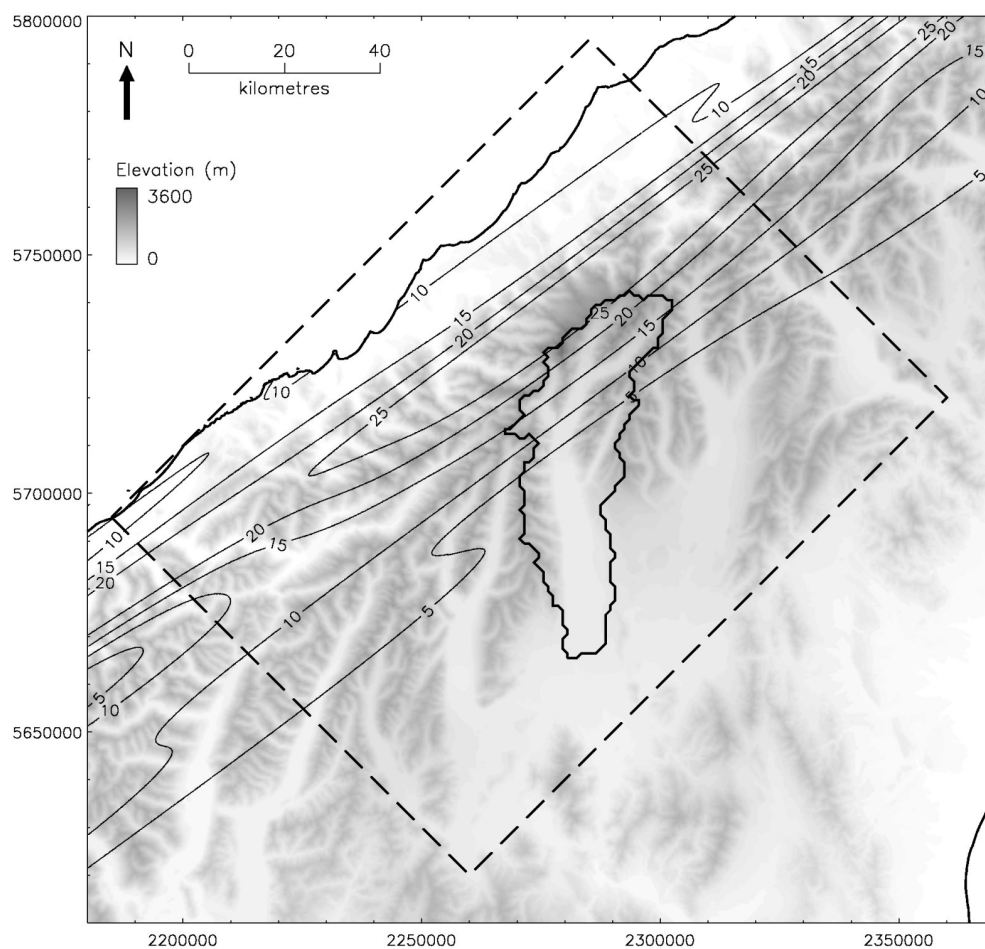
Figure 5.12 Isohyets of interpolated observations of mean daily precipitation (mm dy^{-1}) in the central Southern Alps from 1971 to 2000 (Surf$_{\mathrm{Obs.D}}$).
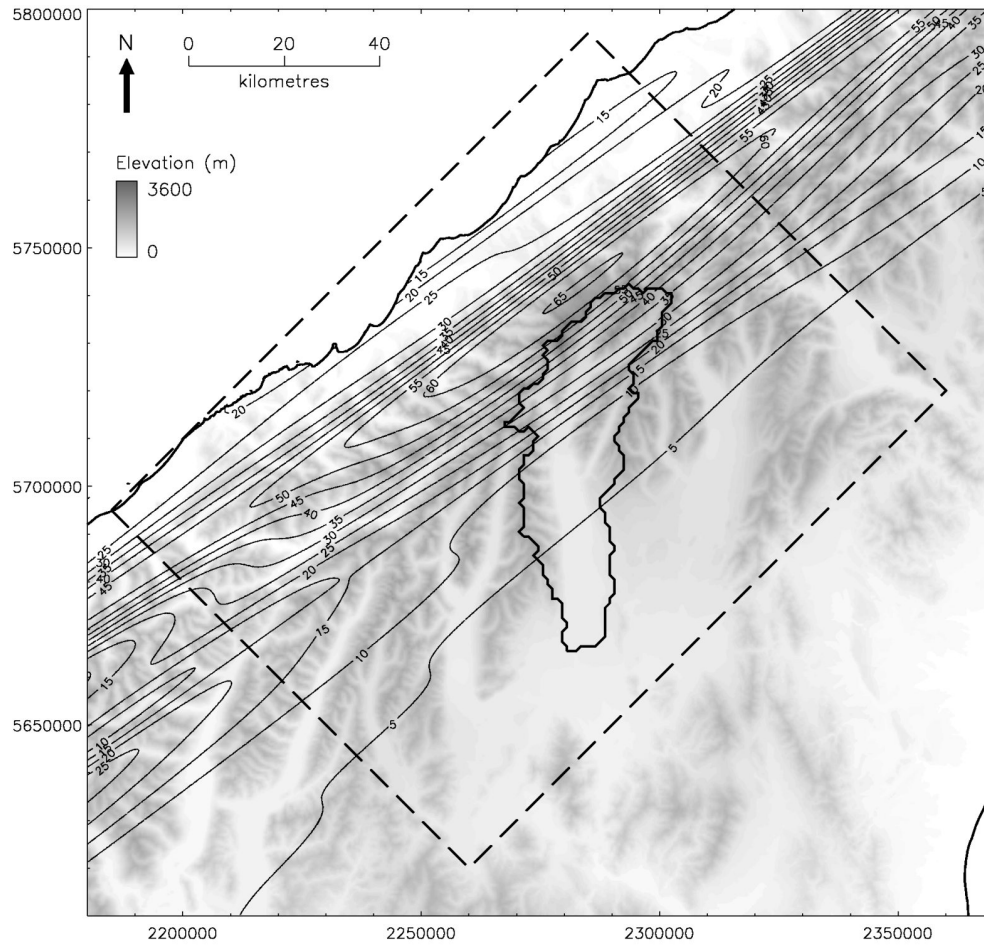
Figure 5.13 Isohyets of interpolated observations of mean daily precipitation (mm dy^{-1}) in the central Southern Alps on northwesterly days from 1971 to 2000 (Surf$_{\mathrm{Obs.D.NW}}$), that is, days on which the mean horizontal wind at 850 hPa 42.5° S 170° E blew from bearings of 270–360°.

main orographic axis.

The surface of mean daily precipitation on southwesterly days ($Surf_{Obs.D.SW}$) is shown in Figure 5.14. The isohyetal resolution has been increased to 1 mm dy^{-1} in this image, so as to distinguish the shallower precipitation gradients. Much less precipitation falls in the central Southern Alps on southwesterly days than on northwesterly days, which is consistent with cooler, drier air approaching the Southern Alps from a more oblique angle. The spatial pattern of $Surf_{Obs.D.SW}$ is generally similar to that of $Surf_{Obs.D}$ and $Surf_{Obs.D.NW}$, but the wettest transect on southwesterly days is the Milford transect rather than the Franz Josef transect, which reflects the increased exposure of the Fiordland region to southwesterly winds.

The surface of mean daily precipitation on northeasterly days ($Surf_{Obs.D.NE}$, not pictured) was distorted in the Milford region by lack of data. The overall magnitude of precipitation on northeasterly days was again low relative to that on northwesterly days. $Surf_{Obs.D.NE}$ is generally highest on the northwest flank of the Southern Alps, and, excluding the distorted Milford region, peaks at 13 mm dy^{-1} on the northwest edge of the Pukaki catchment. The surface of mean daily precipitation on southeasterly days ($Surf_{Obs.D.SE}$, not pictured) exhibits the lowest overall rainfall of the 4 precipitation surfaces classified by daily wind direction (northwesterly, southwesterly, northeasterly, southeasterly).

5.4 Simulation of precipitation from 1971 to 2000

To have a measure of confidence in downscaled global projections of future precipitation, the HadRM3P regional climate model should first be able to replicate the general spatial pattern of observed rainfall in the Southern Alps in recent decades. Significant differences between the spatial distributions of simulated and observed precipitation may indicate that certain aspects of HadRM3P, such as the model's orography or the parameterisation of meteorological processes, need to be recalibrated. This section examines the
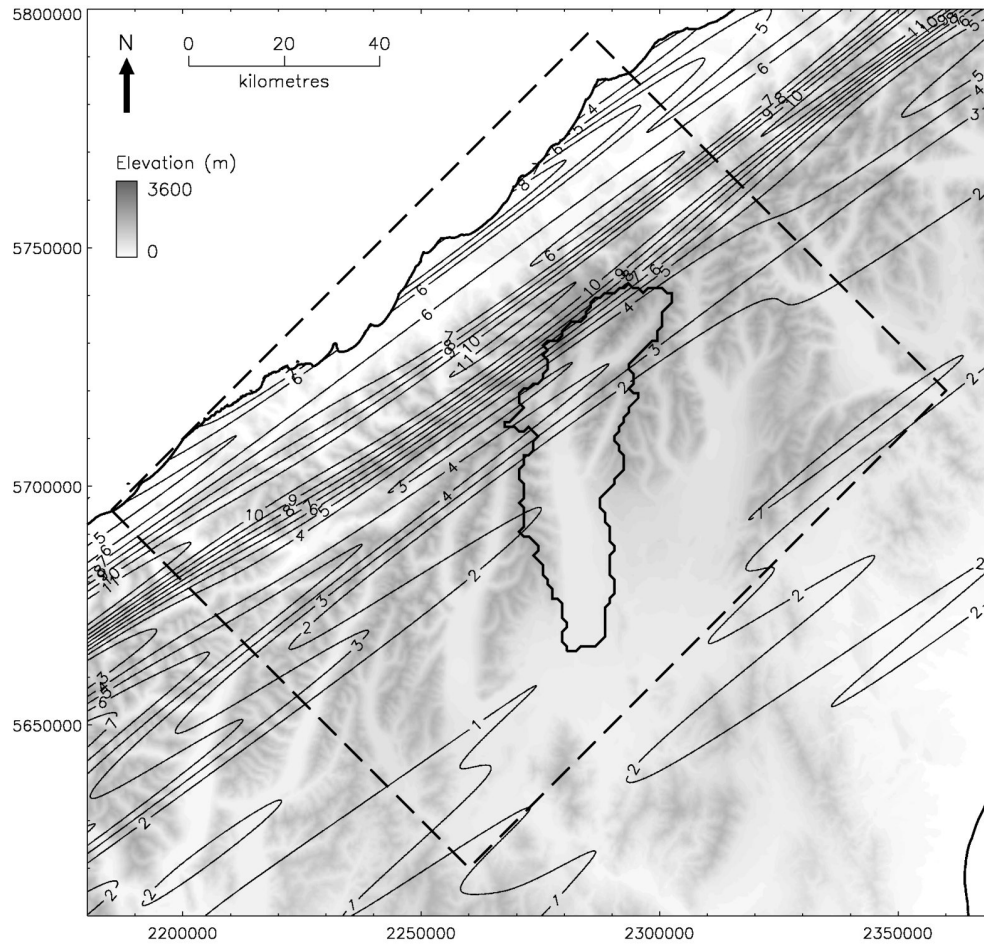
Figure 5.14 Isohyets of interpolated observations of mean daily precipitation (mm dy^{-1}) in the central Southern Alps on southwesterly days from 1971 to 2000 (Surf$_{\text{Obs.D.SW}}$), that is, days on which the mean horizontal wind at 850 hPa 42.5° S 170° E blew from bearings of 180–270°.

spatial distribution of mean annual precipitation simulated in the central Southern Alps from 1971 to 2000, both at HadRM3P's original spatial resolution of 30 km, and at downscaled resolutions of 100 m and 1 km. To evaluate the skill of the downscaling method, the simulated precipitation is compared with observations from individual rain gauges, and also with an independently constructed surface of observed precipitation in the Pukaki catchment.

5.4.1 Distribution of simulated precipitation

Figure 5.15 shows mean annual precipitation in the central Southern Alps from 1971 to 2000, as simulated by HadRM3P at 30-km resolution; this surface will hereafter be referred to as $Surf_{Rcm.A.Raw}$. One can see a 'wall' of very high precipitation simulated along the West Coast of the South Island, ranging from 7.9 m a^{-1} in the southwest near Haast, up to 9.5 m a^{-1} in the northeast over the Whataroa catchment. By comparison with the $Surf_{Obs.A}$ surface of observed precipitation (Figure 5.8), the amount of simulated precipitation appears to be too high on the edge of the West Coast. As mentioned in Chapter 1, at a spatial resolution of 30 km, HadRM3P cannot accurately represent steep precipitation gradients, such as those that occur in the West Coast region. The excessive simulated precipitation in parts of the West Coast is also likely to be partly due to the representation of New Zealand orography within HadRM3P (Figure 2.5), in which the topography of the West Coast rises abrubtly at its boundary with the Tasman Sea. This sudden rise in the modelled topography is likely to exaggerate both the simulated orographic uplift of air and the consequent precipitation on the edge of the West Coast.

Moving southeastward away from the West Coast, the next NE-SW diagonal line of RCM grid cells generally lies over the most elevated region of the Southern Alps. HadRM3P simulates 5.4–6.8 m a^{-1} of precipitation along this line of grid cells. Further to the southeast, in the rain shadow of the Southern Alps, the RCM simulates on average around 0.3–1.3 m a^{-1} of precipitation.

The coarse simulated precipitation was then downscaled to a horizontal
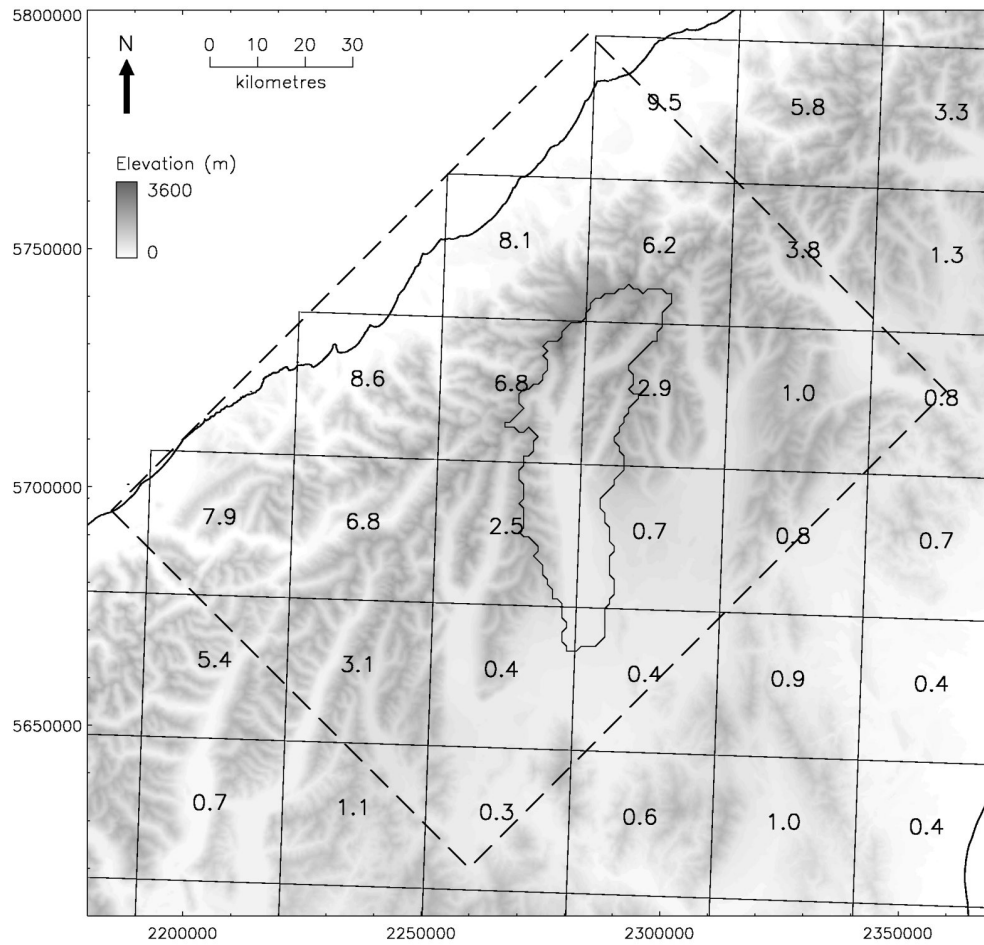
Figure 5.15 Mean annual precipitation (m a^{-1}) in the central Southern Alps from 1971 to 2000, as simulated by HadRM3P at 30-km resolution (Surf$_{\mathrm{Rcm.A.Raw}}$). Squares outline the grid cells of the RCM within the land mask of the model.

spatial resolution of 100 m. The downscaling was performed via a thin-plate smoothing spline, with the $\text{Surf}_{\text{Obs.D}}$ surface of observed mean daily precipitation employed as an independent variable, as described in Section 4.2. Initially, a square-root transformation was applied during the trivariate interpolation, in order to reduce skewness within the frequency distribution of the simulated precipitation. Figure 5.16 shows isohyets of the simulated rainfall after being downscaled in this manner; this surface is hereafter referred to as $\text{Surf}_{\text{Rcm.A.DsT}}$. The downscaled precipitation surface is represented by curved contour lines, and $\text{Surf}_{\text{Rcm.A.DsT}}$ is a far smoother surface than $\text{Surf}_{\text{Rcm.A.Raw}}$.

$\text{Surf}_{\text{Rcm.A.DsT}}$ exhibits a fairly steep horizontal gradient across the Southern Alps. The surface rises from around 5 m a^{-1} on the edge of the West Coast to more than 9 m a^{-1} on the upper northwest flank of the Southern Alps. $\text{Surf}_{\text{Rcm.A.DsT}}$ has a peak value of 9.98 m a^{-1} in the upper Mahitahi catchment, approximately 40 km southwest of Aoraki Mount Cook. Moving southeastward across the Pukaki catchment, the surface quickly drops away from around 8 m a^{-1} to around 2–3 m a^{-1}, before falling below 1 m a^{-1} on the southeast side of the South Island.

The smoothing parameter ρ of the thin-plate smoothing spline fitted to $\text{Surf}_{\text{Rcm.A.DsT}}$ was 1.56×10^{-5}, that is, almost zero. ρ was determined by minimising the generalised cross validation (GCV). The spline's signal of 57 is equal to the total number of interpolated RCM grid points. This leads to a signal-to-error ratio of 57:0, which suggests that the surface-fitting procedure has failed to find a genuinely optimum value for ρ (Hutchinson 2000). The low value of ρ results in 'overfitting' of the surface to the grid points (represented by '•' symbols in Figure 5.16). The grid points are consequently given too much 'pull', causing concentric circles to form around the grid points in some regions.

Figure 5.17 shows isohyets of precipitation that has been simulated by HadRM3P and then downscaled, without transforming the simulated precipitation during the interpolation process. ρ was again determined by minimising the GCV. This surface is hereafter referred to as $\text{Surf}_{\text{Rcm.A.Ds}}$. $\text{Surf}_{\text{Rcm.A.Ds}}$ is generally quite similar to $\text{Surf}_{\text{Rcm.A.DsT}}$, but it is more loosely fitted to the RCM grid points, resulting in a smoother surface with little distortion. This
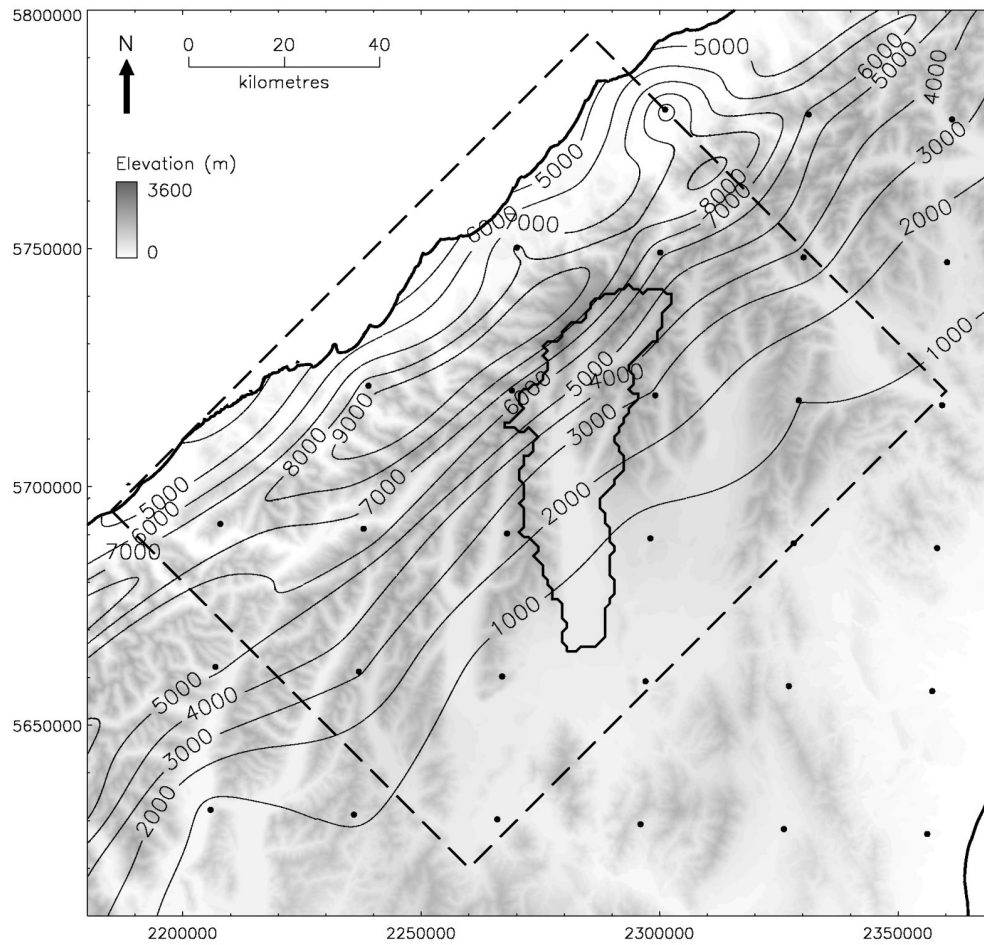
Figure 5.16 Isohyets of mean annual precipitation (mm a^{-1}) the central Southern Alps from 1971 to 2000, simulated by HadRM3P and downscaled using a square-root transformation (Surf$_{\mathrm{Rcm.A.DsT}}$). '•' symbols denote RCM grid points.
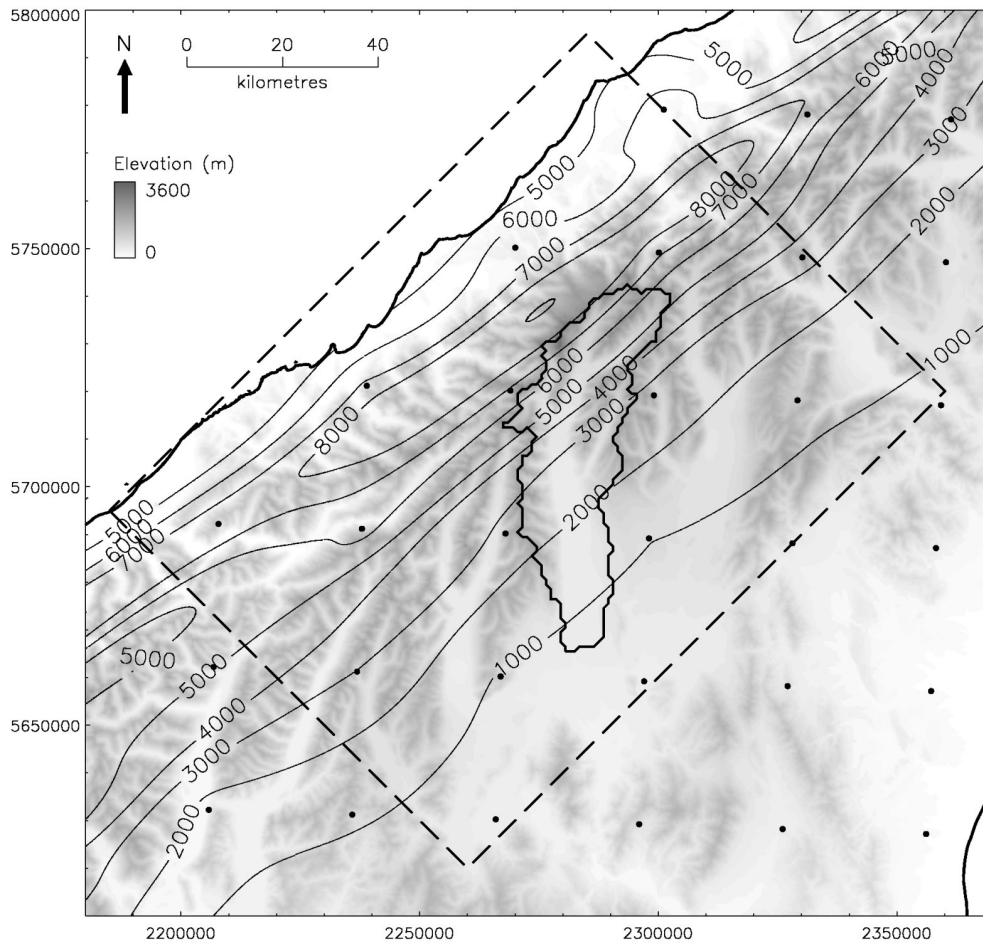
Figure 5.17   Isohyets of mean annual precipitation $(\mathrm{mm\ a}^{-1})$ in the central Southern Alps from 1971 to 2000, simulated by HadRM3P and downscaled without transformation $(\mathrm{Surf_{Rcm.A.Ds}})$. '•' symbols denote RCM grid points.

is reflected in the statistics of the spline. $\text{Surf}_{\text{Rcm.A.Ds}}$ has a much larger value of ρ (831) and a more optimal signal-to-error ratio of 34:23, which approximately equates to 1.5:1. $\text{Surf}_{\text{Rcm.A.Ds}}$ peaks at 9.02 m a^{-1} on the upper Fox Range, around 6 km northwest of the Pukaki catchment boundary. Moving southeastward across the Pukaki catchment, this surface also drops quickly away from around 8 m a^{-1} to around 2–3 m a^{-1}, though at a slightly lower rate than $\text{Surf}_{\text{Rcm.A.DsT}}$. This slight shallowing of the horizontal precipitation gradient in $\text{Surf}_{\text{Rcm.A.Ds}}$ is a consequence of the higher ρ. The reduced distortion present in $\text{Surf}_{\text{Rcm.A.Ds}}$ suggests that this surface describes the annual distribution of precipitation in the central Southern Alps more realistically than $\text{Surf}_{\text{Rcm.A.DsT}}$.

5.4.2 Comparison of simulated precipitation with observations

Validation of simulated precipitation against rain gauges

The simulated and downscaled precipitation was compared with observations in order to assess its accuracy. HadRM3P was initially validated against long-term observations from individual rain gauges. These gauges were all located within the primary study region, and had each recorded at least 15 years of precipitation during the 30-year period from 1971 to 2000. The latter requirement was imposed to allow the mean annual precipitation at each gauge to be estimated with reasonable accuracy, although it did reduce to 17 the number of gauges available at elevations above 500 m a.s.l. Twenty-eight gauges within the Franz Josef and Haast transects fulfilled both selection criteria; the locations of these gauges are shown in Figure 5.18.

From 1971 to 2000, the average total period of observation at these stations was 24.3 years. The elevations of the stations range from 2 to 1027 m a.s.l, with a mean elevation of 461 m a.s.l. None of the long-term gauges are located in the wettest region of the Southern Alps, that is, the upper northwest flank. The wettest validation gauge is at Franz Josef Village (155 m a.s.l.), where an annual average of 5.9 m of rainfall was recorded during 18.4 years of observation between 1982 and 2000.
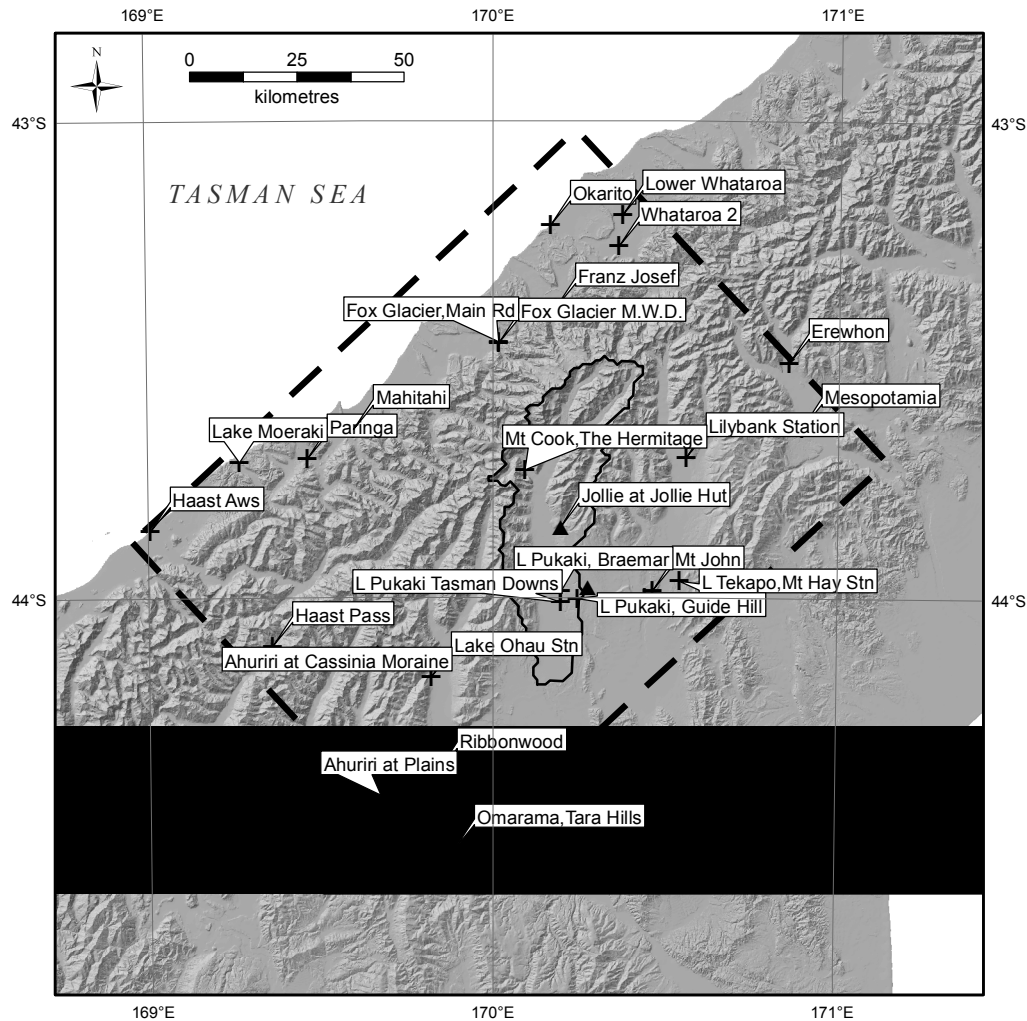
Figure 5.18 Stations in the central Southern Alps used to validate precipitation simulated by HadRM3P from 1971 to 2000. '+' symbols denote CliDB gauges, '▲' symbols denote WRA gauges. The thick dashed line delineates the primary study region. The Pukaki catchment is outlined by a thin solid line within the primary study region.

Table 5.2 Mean annual precipitation simulated by HadRM3P, minus observations from rain gauges, from 1971 to 2000. Bias equates to the mean error of the simulated precipitation, by comparison with observations from 28 long-term rain gauges.

Surface	Max. Deficit $(m\,a^{-1})$	Max. Surplus $(m\,a^{-1})$	Bias $(m\,a^{-1})$	RMSE $(m\,a^{-1})$
$Surf_{Rcm.A.Raw}$	1.4	5.7	1.1	2.2
$Surf_{Rcm.A.DsT}$	0.6	4.1	0.9	1.4
$Surf_{Rcm.A.Ds}$	0.4	2.5	0.8	1.0

Comparisons between HadRM3P and each individual validation gauge are presented in Table B.1 of Appendix B. These comparisons are summarised in the three scatter plots shown in Figure 5.19. Also displayed in each of these three plots is the coefficient of determination (r^2), and a dashed line of equal simulated and observed precipitation, that is, the 'target line' for a perfect model. At 30-km resolution (Figure 5.19a), HadRM3P tends to overestimate precipitation at the sites of the validation gauges: $Surf_{Rcm.A.Raw}$ has a wet bias (mean error) of 1.1 m a^{-1}, and a substantial root mean square error (RMSE) of 2.2 m a $^{-1}$ (Table 5.2). The greatest surpluses of simulated precipitation are on the West Coast, where the model orography is generally 400–800 m a.s.l. higher than the actual elevations of the validation sites. The maximum surplus occurs in the lower Whataroa catchment (30 m a.s.l.): here $Surf_{Rcm.A.Raw}$ overestimates rainfall by 5.7 m a^{-1}. HadRM3P performs better in the rain shadow southeast of the Southern Alps, where both modelled and observed precipitation are generally less than 3 m a^{-1}. The mismatch between the model elevations and those of the validation sites is less pronounced in this region, and simulated precipitation is within 0.5 m a^{-1} of observations.

Less excess precipitation on the West Coast is present in $Surf_{Rcm.A.DsT}$, as can be seen by the improved correlation between simulated and observed precipitation in Figure 5.19b. The trivariate interpolation introduces a smooth 'downhill' gradient from the upper northwestern flank of the Southern Alps, northwest to the Tasman Sea. This results in less surplus rainfall on the West

(a) $\mathrm{Surf}_{\mathrm{Rcm.A.Raw}}$

(b) $\mathrm{Surf}_{\mathrm{Rcm.A.DsT}}$

(c) $\mathrm{Surf}_{\mathrm{Rcm.A.Ds}}$
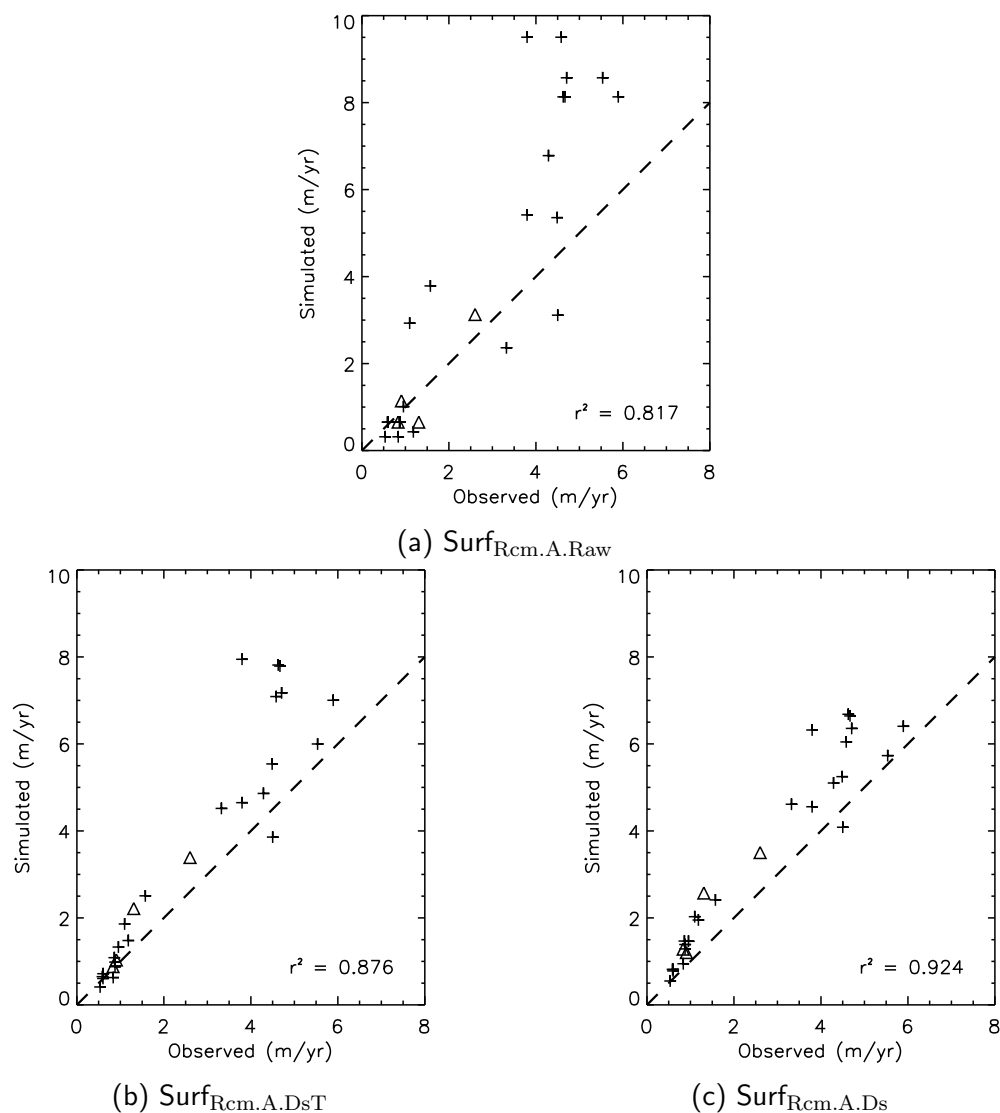
Figure 5.19   Mean annual precipitation (m a^{-1}) simulated by HadRM3P versus observations from rain gauges from 1971 to 2000. '+' symbols denote CliDB gauges, '$\triangle$' symbols denote WRA gauges. The dashed line indicates a perfect model, where simulated precipitation equals observed precipitation. Downscaling has improved the match between simulated and observed precipitation, as indicated by the higher coefficients of determination (r^2) in (b) and (c).

Coast and a lower RMSE of 1.4 m a^{-1} in $Surf_{Rcm.A.DsT}$. However, a wet bias of 0.9 m a^{-1} still exists. The low smoothing parameter ρ for $Surf_{Rcm.A.DsT}$ causes the surface to be tightly fitted to the excessive precipitation simulated at the HadRM3P grid points on the West Coast. The maximum surplus of simulated precipitation, 4.1 m a^{-1}, is still in the lower Whataroa catchment.

The surplus rainfall is further reduced in $Surf_{Rcm.A.Ds}$ (Figure 5.19c), which has the highest r^2 (0.924) of the three surfaces, and a 53% reduction in RMSE to 1.0 m a^{-1}. This surface is not so tightly fitted to the excessive precipitation simulated at the RCM grid points on the West Coast, and the maximum surplus precipitation, again at Whataroa, decreases subtantially to 2.5 m a^{-1}. The wet bias also drops slightly to 0.8 m a^{-1}. The maximum deficit of simulated precipitation falls from 1.4 m a^{-1} in $Surf_{Rcm.A.Raw}$ to 0.4 m a^{-1} in $Surf_{Rcm.A.Ds}$. Thus in $Surf_{Rcm.A.Ds}$, the RMSE, maximum surplus and maximum deficit of simulated precipitation are all at least 50% lower than in $Surf_{Rcm.A.Raw}$. By comparison with long-term observations from these 28 rain gauges in the Southern Alps, the downscaled surface $Surf_{Rcm.A.Ds}$ is a significant improvement upon the precipitation simulated by HadRM3P at its original spatial resolution of 30 km.

Comparison between simulated and observed precipitation within the Pukaki catchment

In order to further assess the accuracy of the precipitation simulated by HadRM3P, the simulated and downscaled precipitation surfaces were validated against a surface of estimated 'true' precipitation in the Pukaki catchment ($Surf_{Obs.TK.T}$, Figure 3.6b), which was independently produced by Kerr (2009). $Surf_{Obs.TK.T}$ takes into account the estimated undercatch at rain gauges. The simulated and observed precipitation in the Pukaki catchment were compared at the 1-km resolution of the precipitation surfaces provided by Kerr (2010).

In Figure 5.20a, which compares the raw RCM ($Surf_{Rcm.A.Raw}$) to $Surf_{Obs.TK.T}$, the differenced precipitation surface contains sharp steps at the edges of the 30-km grid cells of HadRM3P. Within each RCM grid cell, the simulated precipitation tends toward a deficit in the northwest, and a surplus

(a) Surf$_{\mathrm{Rcm.A.Raw}}$

(b) Surf$_{\mathrm{Rcm.A.DsT}}$

(c) Surf$_{\mathrm{Rcm.A.Ds}}$

metres/year
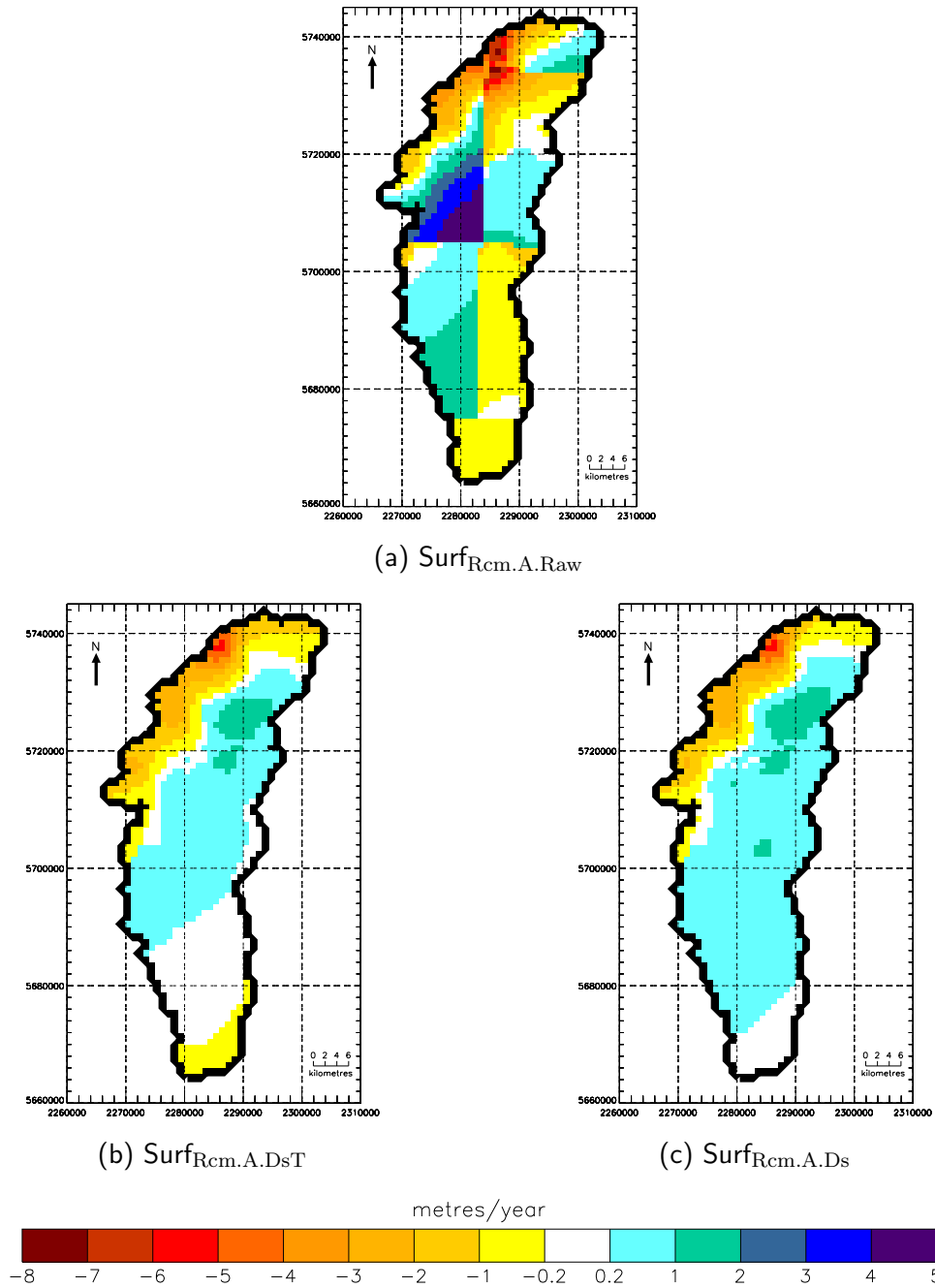
Figure 5.20 Mean annual precipitation (m a^{-1}) simulated by HadRM3P, minus estimated 'true' mean annual precipitation (Surf$_{\mathrm{Obs.TK.T}}$) in the Pukaki catchment, from 1971 to 2000. 'True' mean annual precipitation was estimated by Kerr (2009). Cool colours indicate a wet bias in HadRM3P; warm colours indicate a dry bias.

in the southeast. This is indicative of the uniform rainfall simulated within each 30-km grid cell of the model, which cannot accurately represent the observed horizontal precipitation gradient at smaller spatial scales.

There is a deficit of simulated precipitation in the northwest of the Pukaki catchment, near its boundary with the Main Divide, where the topography is most elevated. HadRM3P underestimates precipitation by up to 7.6 m a^{-1} in this region. In the middle of the catchment, HadRM3P overestimates precipitation by up to 5.0 m a^{-1}.

Figure 5.20b compares $\text{Surf}_{\text{Obs.TK.T}}$ with precipitation that has been simulated and downscaled using a square-root transformation ($\text{Surf}_{\text{Rcm.A.DsT}}$). This differenced surface is much smoother than Figure 5.20a, with most of $\text{Surf}_{\text{Rcm.A.DsT}}$ lying within 1.0 m a^{-1} of the estimated 'true' mean annual precipitation. The downscaled surface still evidently underestimates precipitation in the northwest of the catchment, though the maximum deficit has dropped to 5.5 m a^{-1}. The precipitation deficit in this area of the downscaled surface is due to two main factors. Firstly, with respect to $\text{Surf}_{\text{Obs.TK.T}}$ (Figure 3.6b), HadRM3P simulates a relatively low amount of precipitation in the northwest catchment at its original 30-km resolution (Figure 5.15). The second factor relates to the third independent variable of the trivariate interpolation used in the downscaling process, namely the $\text{Surf}_{\text{Obs.D}}$ surface of observed mean daily rainfall (Figure 5.12). The horizontal precipitation gradient of $\text{Surf}_{\text{Obs.D}}$ in the northwest Pukaki catchment is not as steep as that of $\text{Surf}_{\text{Obs.TK.T}}$, as described earlier in Section 5.3.1. This contributes to the relative shallowness of the gradient in the downscaled surface $\text{Surf}_{\text{Rcm.A.DsT}}$, with respect to $\text{Surf}_{\text{Obs.TK.T}}$. The maximum surplus of precipitation in $\text{Surf}_{\text{Rcm.A.DsT}}$ lies over the southern Liebig Range in the northeast part of the catchment, where precipitation is overestimated by 1.8 m a^{-1}.

Figure 5.20c shows the differences between $\text{Surf}_{\text{Obs.TK.T}}$ and the precipitation that was simulated and downscaled without any transformation of the dependent variable ($\text{Surf}_{\text{Rcm.A.Ds}}$). The general pattern of differences is similar that in Figure 5.20b, though a small wet bias of 0.2–1.0 m a^{-1} is present throughout most of the southern part of the catchment. This wet bias is reflective of the shallower precipitation gradient in $\text{Surf}_{\text{Rcm.A.Ds}}$ — a

Table 5.3 Maximum deficit, maximum surplus, catchment bias and RMSE of mean annual precipitation simulated by HadRM3P in the Pukaki catchment from 1971 to 2000, when validated against estimated 'true' mean annual precipitation (Surf$_{\text{Obs.TK.T}}$). 'True' mean annual precipitation in the Pukaki catchment was estimated by Kerr (2009). The formula used to calculate the catchment bias is shown in Equation 5.1.

Surface	Max. Deficit (m a^{-1})	Max. Surplus (m a^{-1})	Catchment Bias (%)	RMSE (m a^{-1})
Surf$_{\text{Rcm.A.Raw}}$	7.6	5.0	+3.6	1.8
Surf$_{\text{Rcm.A.DsT}}$	5.5	1.8	-2.0	1.0
Surf$_{\text{Rcm.A.Ds}}$	5.5	2.0	+5.3	1.0

consequence of the smoother interpolation of the simulated precipitation.

The overall catchment bias of each of the three RCM surfaces was calculated as

$$\text{Catchment Bias} = \frac{\sum \left(\text{Surf}_{\text{Rcm}} - \text{Surf}_{\text{TK.T}}\right)}{\sum \text{Surf}_{\text{TK.T}}} \qquad (5.1)$$

where $(\text{Surf}_{\text{Rcm}} - \text{Surf}_{\text{TK.T}})$ is the difference between the simulated and estimated 'true' mean annual precipitation in each of the 1-km grid cells throughout the Pukaki catchment, and $\sum \text{Surf}_{\text{TK.T}}$ is the sum of the estimated 'true' mean annual precipitation across all of the 1-km grid cells throughout the catchment. Table 5.3 summarises the comparison of the simulated precipitation to observations in the Pukaki catchment. Surf$_{\text{Rcm.A.Raw}}$ has on average a wet bias of 3.6%, while Surf$_{\text{Rcm.A.DsT}}$ has a small dry bias of 2.0%. Surf$_{\text{Rcm.A.Ds}}$ has an overall wet bias of 5.3%, which is indicative of the relatively small (generally < 1.0 m a^{-1}) wet bias of this surface in much of the catchment.

Across all of the 1-km grid cells within the Pukaki catchment, the RMSE of the simulated precipitation drops from 1.8 m a^{-1} in Surf$_{\text{Rcm.A.Raw}}$ to 1.0 m a^{-1} in both Surf$_{\text{Rcm.A.DsT}}$ and Surf$_{\text{Rcm.A.Ds}}$. This equates to RMSE reductions of 48% in Surf$_{\text{Rcm.A.DsT}}$ and 45% in Surf$_{\text{Rcm.A.Ds}}$. (The reductions in RMSE are 3% different from one another when the calculations are performed to several significant figures.) With their higher spatial resolu-

tion, the downscaled surfaces can more accurately represent the observed fall in precipitation associated with increasing distance from the Main Divide. These reductions in the RMSE represent a significant improvement in the accuracy of mean annual precipitation simulated by HadRM3P in the Pukaki catchment.

5.5 Case study: precipitation on 5 November 1994

The nesting of HadRM3P within reanalyses of historical atmospheric conditions allows past individual weather events to be recreated within the domain of the model, albeit at the model's relatively coarse resolution of 30 km. This section contains an analysis of precipitation simulated during an intense northwesterly storm in November 1994, and compare the simulated precipitation to observations from rain gauges. Comparisons are made at the original 30-km resolution of the RCM, and at 100-m resolution after the simulated precipitation has been downscaled via a trivariate thin-plate smoothing spline.

5.5.1 Observed weather during the Guy Fawkes storm

The 'Guy Fawkes storm' was an extended northwesterly storm from 4 to 9 November 1994, during which more than 1300 mm of rain was recorded in some areas near the Main Divide of the Southern Alps (Sinclair et al. 1997). The focus of the present analysis is the second day of the storm: 5 November UTC. Figure 5.21 shows mean sea level pressure and 850-hPa isotachs on 5 and 6 November 1994. An anticyclone to the east of New Zealand slowed the movement of a trough across the Tasman Sea, bringing a warm, moist northwesterly flow to the country. Blocking of low level air by the Southern Alps led to northeasterly barrier winds on the West Coast of the South Island from 4 to 6 November, but synoptic-scale airflow further upstream of the Southern Alps was from the northwestern quadrant throughout the period from 4 to 8 November. On 5 November, at the 42.5° S 170° E grid point of
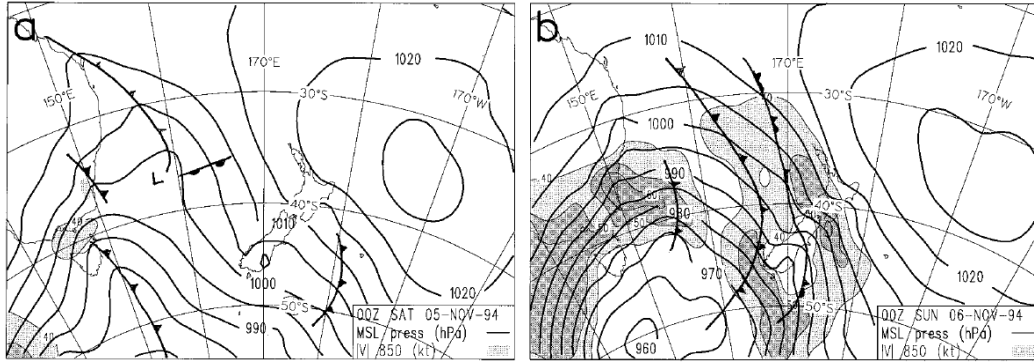
Figure 5.21 ECMWF mean sea level pressure (solid, every 5 hPa) and 850-hPa isotachs, with values greater than 40 kt and 50 kt shaded (1 kt = 0.514 m s^{-1}), at 00:00 5 Nov 1994 (left) and 00:00 6 Nov 1994 (right) UTC. Maps reproduced from Sinclair et al. (1997), including frontal positions from analyses by the Meteorological Service of New Zealand.

NCEP/NCAR Reanalysis 1, the mean horizontal wind velocity at 850 hPa was 19 m s^{-1} from an approximately northwesterly bearing of 331°. An occluded front encountered the South Island on 5 November, and strong winds and heavy rainfall were recorded on the West Coast and in the Southern Alps. Sinclair et al. (1997) showed that the profile of observed precipitation moved southeastward across the mountains on 6 and 7 November, causing substantial spillover in catchments east of the Main Divide. This movement was associated with a reduction in static stability and an increase in the wind speed normal to the axis of the mountains, particularly above the freezing level.

5.5.2   Simulated precipitation on 5 November 1994

Precipitation simulated at 30-km resolution on 5 November 1994

The distribution of precipitation simulated by HadRM3P on 5 November 1994 UTC, at the original 30-km resolution of the model, is shown in Figure 5.22. This surface is hereafter referred to as Surf$_{\text{Rcm.D.Raw}}$. Heavy orographic rainfall of 160–210 mm is simulated along the West Coast, with 210 mm falling in the Whataroa catchment in the northern corner of the primary study region.

Moving inland from the West Coast and on to the highly elevated spine of the Southern Alps (see Figure 2.5 for topographic elevations of the HadRM3P grid cells), rainfall ranges from 134 mm in the southwest up to 227 mm in the northeast. Some precipitation spills over the Main Divide into southeast catchments, though the magnitude of rainfall suddenly drops further to the southeast, from 71–80 mm in the middle of the Pukaki catchment down to 0–1 mm over the Canterbury plains. The heaviest orographic rainfall is thus generally confined to the region upwind of and over the mountains, which is reasonably consistent with the observed blocking of low-level air northwest of the Main Divide during the first two days of the storm.

The simulated precipitation was compared with observations from rain gauges, in order to assess its accuracy. Only WRA gauges were used to validate the short-term precipitation, owing to the 4-hour difference between the observations periods of the CliDB gauges (20:00 to 20:00 UTC) and the days of the HadRM3P simulation (00:00 to 00:00 UTC). Nineteen WRA gauges recorded precipitation within the primary study region on 5 November 1994 (Figure 5.23). These gauges were generally situated at higher and more mountainous locations than the gauges used to validate the 30-year simulation. The topographic elevation of the short-term validation stations ranged from 58 m a.s.l. to 1509 m a.s.l., with a mean elevation of 728 m a.s.l.

At the location of each of the 19 validation gauges, the precipitation simulated by HadRM3P was compared to the observed precipitation. The result of each of these individual comparisons is presented in Table B.2 of Appendix B. A summary of these comparisons is presented in Table 5.4, which shows the maximum deficit, maximum surplus, bias and RMSE across all of the 19 locations. At 30-km resolution, the simulated precipitation differs greatly from observations at some of validation gauges. $\text{Surf}_{\text{Rcm.D.Raw}}$ overestimates precipitation by 199 mm at Panoroma Ridge (1509 m a.s.l.) in the upper Godley catchment. However, the observed 11 mm of rainfall at Panoroma Ridge looks suspiciously low compared to the 219 mm observed at Eade Hut (975 m a.s.l.), just 4 km to the south. Across all of the 19 validation gauges, $\text{Surf}_{\text{Rcm.D.Raw}}$ has a substantial RMSE of 78 mm and a wet bias of 29 mm. The RCM generally appears to be too wet on the western
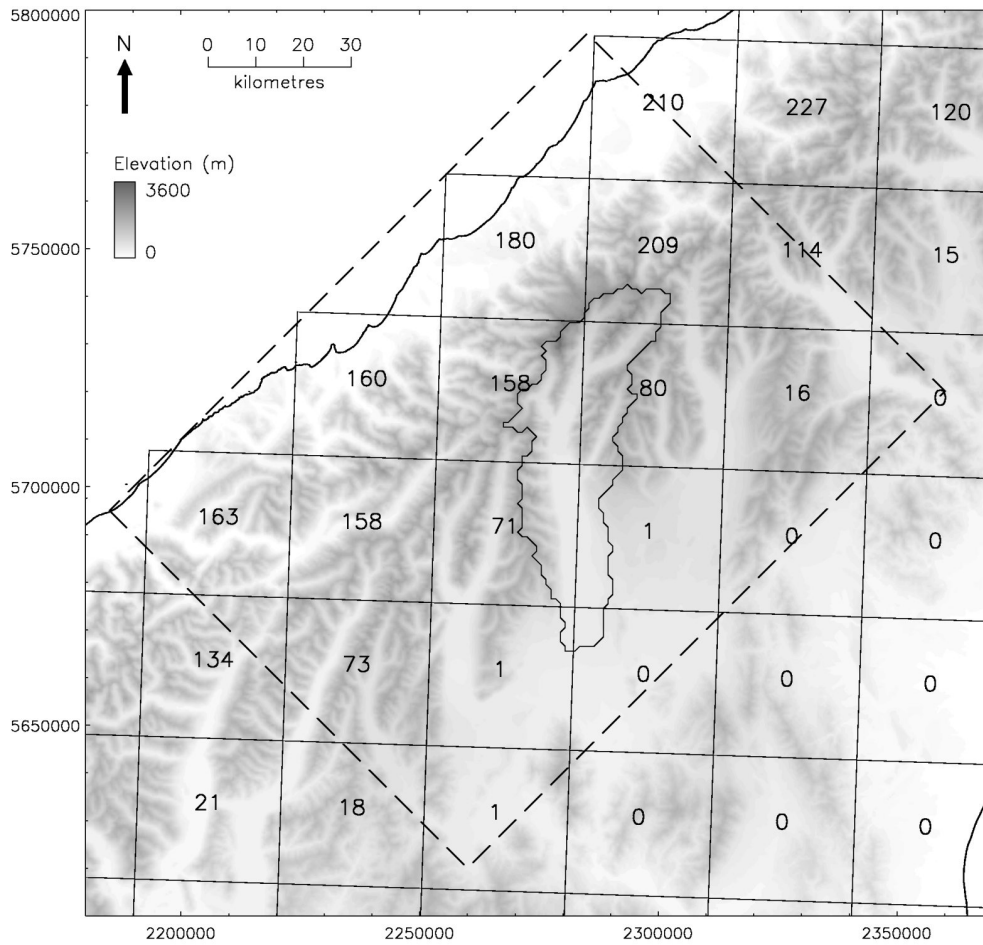
Figure 5.22   Precipitation (mm) in the central Southern Alps on 5 Nov 1994 UTC, as simulated by HadRM3P at 30-km resolution (Surf$_{\mathrm{Rcm.D.Raw}}$). Squares outline the grid cells of the RCM within the land mask of the model.
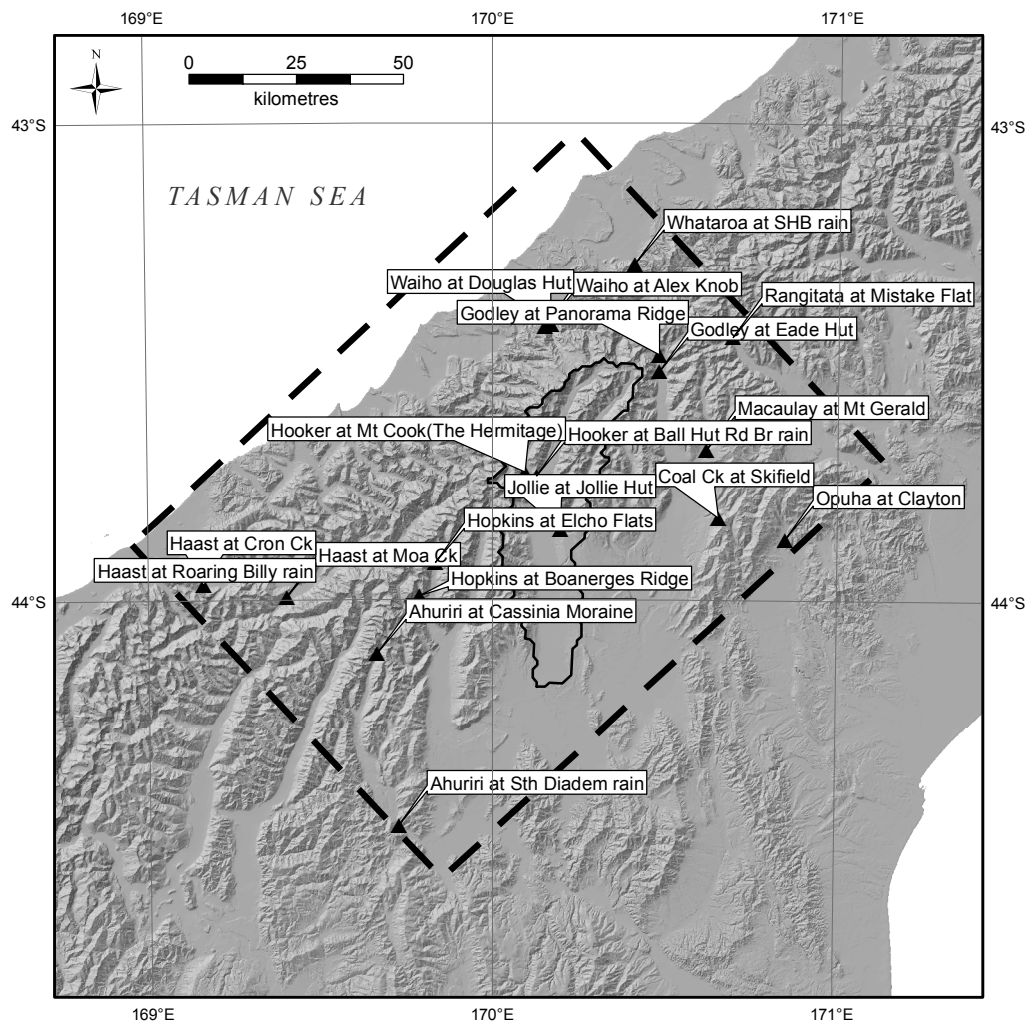
Figure 5.23 Stations in the central Southern Alps used to validate precipitation simulated by HadRM3P on 5 Nov 1994. '▲' symbols denote WRA gauges.

Table 5.4 HadRM3P-simulated precipitation minus observations from rain gauges on 5 Nov 1994 UTC. Comparisons were performed at the location of each of the 19 gauges shown in Figure 5.23; the maximum deficit, maximum surplus, bias and RMSE of the simulated precipitation across all of these 19 locations are presented in the table below. Bias equates to the mean error of the simulated precipitation, when validated against the 19 rain gauges.

Surface	Max. Deficit (mm)	Max. Surplus (mm)	Bias (mm)	RMSE (mm)
$Surf_{Rcm.D.Raw}$	106	199	29	78
$Surf_{Rcm.D.Ds}$	118	141	6	65
$Surf_{Rcm.D.Ds.NW}$	109	143	9	65

flank of the Southern Alps, and too dry to the east of the Main Divide. This may be due to excessively high topography in this version of the RCM, which could exaggerate both orographic precipitation and lee-side drying. A new orographic model of New Zealand has been since been incorporated into HadRM3P. The topographic elevations of both the West Coast and the Southern Alps are significantly reduced in the updated version.

Downscaled precipitation on 5 November 1994

The precipitation simulated by HadRM3P on 5 November 1994 was first downscaled by using the $Surf_{Obs.D}$ surface of observed mean daily rainfall as the third independent variable of the trivariate interpolation, with no transformation of the simulated daily rainfall. Initially, the smoothing parameter ρ was determined by minimising the GCV, but the resultant surface had a signal-to-error ratio of 57:0. This indicated that the downscaled surface fitted exactly to the precipitation simulated at the RCM grid points, with no 'error', that is to say, no residual. This surface was consequently somewhat distorted.

An alternative smoothing method was used, in which a fixed signal was supplied to the spline procedure. The resulting downscaled surface was validated against observations from the rain gauges. A square-root transforma-

tion of the daily rainfall was disregarded because it increased the RMSE of
the downscaled surface. A number of different fixed signals were tried; the
lowest RMSE (65 mm) was achieved by using a fixed signal-to-error ratio of
15:42. This RMSE is 17% less than that of the simulated precipitation at
its original resolution of 30 km. Figure 5.24a shows the simulated precipita-
tion after being downscaled with the fixed signal value of 15. This surface is
hereafter referred to as $\text{Surf}_{\text{Rcm.D.Ds}}$.

$\text{Surf}_{\text{Rcm.D.Ds}}$ is a much-smoothed version of the precipitation simulated on
5 November 1994. In this surface, around 75–100 mm of rainfall falls on the
edge of the West Coast, and rainfall peaks at over 250 mm in the region of the
Franz Josef Glacier and upper Whataroa catchment. A ridge of 175+ mm
rainfall extends southwest-to-northeast along the upper western flank of the
Southern Alps. Spillover into the Pukaki catchment ranges from more than
225 mm in the northern tip, to less than 25 mm in the southern part of
the catchment. By comparison with rain gauges, downscaling the simulated
precipitation decreased the mean bias on 5 November from 29 mm to 6 mm
— a reduction of 79%. However, the high RMSE of 65 mm indicates that
significant differences remain between HadRM3P and observations in some
locations, with the same general trend of a wet bias in the west and a dry
bias in the east.

Since the spatial distribution of rainfall observed in the Southern Alps
varies significantly according to the mean daily wind direction (see Sections
5.2.2 and 5.3.2), it was hypothesised that downscaling skill could be improved
by using the $\text{Surf}_{\text{Obs.D.NW}}$ northwesterly surface (Figure 5.13) as the third
independent variable of the trivariate interpolation. Figure 5.24b shows the
simulated precipitation after being downscaled using $\text{Surf}_{\text{Obs.D.NW}}$ as the third
independent variable. The remaining parameters of the spline interpolation
were not altered. This surface is hereafter referred to as $\text{Surf}_{\text{Rcm.D.Ds.NW}}$.

There is very little difference between $\text{Surf}_{\text{Rcm.D.Ds.NW}}$ and $\text{Surf}_{\text{Rcm.D.Ds}}$.
$\text{Surf}_{\text{Rcm.D.Ds.NW}}$ has the same RMSE of 65 mm and a slightly larger wet
bias of 9 mm. Therefore by comparison with observations from rain gauges,
the use of the northwesterly surface during the trivariate interpolation did
not improve the accuracy of the downscaled precipitation. One reason for
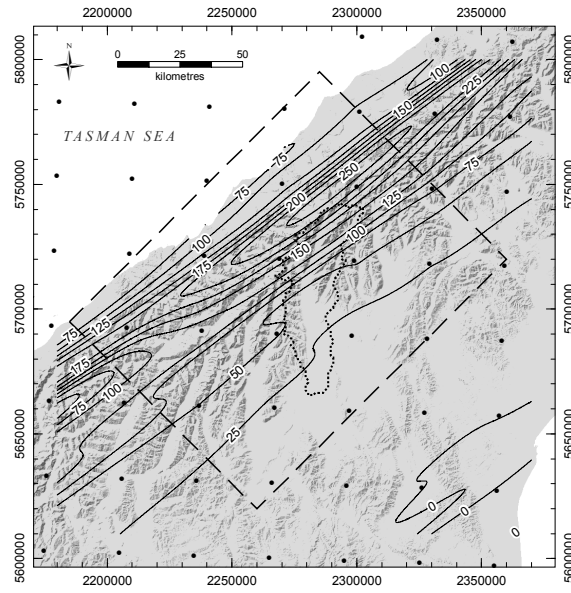
(a) Surf$_{\mathrm{Rcm.D.Ds}}$
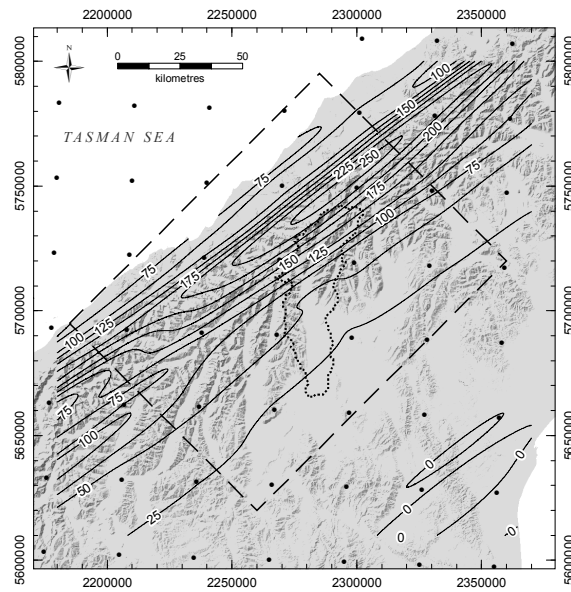
(b) Surf$_{\mathrm{Rcm.D.Ds.NW}}$

Figure 5.24 Isohyets of downscaled HadRM3P-simulated precipitation (mm) in the central Southern Alps on 5 Nov 1994 UTC. '•' symbols denote RCM grid points. The upper surface (Surf$_{\mathrm{Rcm.D.Ds}}$) uses the Surf$_{\mathrm{Obs.D}}$ surface as the third independent variable of the trivariate interpolation; the lower surface uses the Surf$_{\mathrm{Obs.D.NW}}$ surface, as discussed in the text. Each contour represents 25 mm of precipitation.

this may be that the mean daily surface (Surf$_{\text{Obs.D}}$) is reasonably similar in shape to the northwesterly surface (Surf$_{\text{Obs.D.NW}}$) — albeit substantially smaller in magnitude — and thus already reflects a climatology dominated by northwesterlies. However, downscaling skill might be improved by using, for example, a southeasterly surface to downscale precipitation simulated on a southeasterly day, since the climatology on southeasterly days differs more markedly from the mean daily climatology. More research is required to determine whether this approach will actually improve downscaling skill for precipitation simulated by the model during individual weather events.

5.6 Summary of key results

- Observations from rain gauges in the Southern Alps from 1971 to 2000 were objectively interpolated to produce mean annual profiles. Peak mean annual precipitation across the interpolated profiles ranges from 8.6 m a^{-1} at Haast, to 9.0–9.4 m a^{-1} in the Hokitika region, up to a maximum of 10.9 m a^{-1} at Franz Josef.

- The profile of mean daily precipitation in the Southern Alps varies markedly according to the 850 hPa wind direction north of the central Southern Alps. On days when the mean horizontal wind at 850 hPa blows from the east, southeast or south quadrants, the daily precipitation peak across the Southern Alps is located approximately 80 km southeast of the Alpine Fault, well to the southeast of the Main Divide.

- A trivariate thin-plate smoothing spline, incorporating a surface of observed mean daily precipitation as a third independent variable, was used to downscale mean annual precipitation simulated in the central Southern Alps by the HadRM3P regional climate model from 1971 to 2000. Downscaling the simulated precipitation lead to large reductions in RMSE when validated against observations.

- Precipitation simulated by the HadRM3P RCM during an historic northwesterly storm exhibits a generally realistic spatial distribution, but still

differs considerably from point-based observations by rain gauges in some locations. Substantial errors still remain after downscaling via a thin-plate smoothing spline, although the mean wet bias of the simulated precipitation was reduced by almost 80%.

Chapter 6

Discussion

Precipitation is a particularly difficult atmospheric phenomenon to simulate accurately, due to the numerous and complex meteorological interactions that contribute to its formation. The simulation of rainfall is even more difficult in regions of high topographic relief, such as the Southern Alps, where strong orographic forcing causes vigorous condensation of tropospheric moisture and extremely steep horizontal precipitation gradients at the surface. Future advances in computing power will inevitably lead to dynamic climate models with higher spatial resolution and more refined representations of the underlying physical processes that cause precipitation. For example, the newly installed IBM p575 supercomputer at NIWA, FitzRoy, is nearly 100 times more powerful than its Cray T3E1200e predecessor. NIWA is currently upgrading its regional climate model to a newer version of the UKMO Unified Model. This upgraded RCM may soon be simulating the New Zealand climate on FitzRoy at a horizontal resolution of 12 km. However, precipitation simulated by the RCM, even at this increased resolution, is still too spatially coarse to be used in many downstream environmental models, such as the ARC energy-balance model of South Island glaciers, or the TopNet hydrological model currently being developed at NIWA (Clark et al. 2008). In the absence of a dynamic model that is able to accurately simulate long-term climate at a spatial resolution of less than 1 km, some means of mathematical or statistical downscaling is still necessary.

The northeast-southwest axis of the Southern Alps lies across the domi-

nant mid-latitude westerlies. Moisture-laden air blown in from the Tasman Sea encounters the very steep topography of this mountain range, producing a very distinct cross-mountain profile of precipitation. This is the dominant spatial characteristic of precipitation observed in the South Island. In Chapter 1, I asked the research question: what is the spatial distribution of precipitation in the central Southern Alps, and how is it influenced by topography and wind direction? Due to the shortage of available observations in the Milford transect, it is not possible to infer the magnitude and location of maximum rainfall in the Fiordland region from results in this thesis. Across the other objectively interpolated profiles, peak mean annual precipitation ranges from 8.6 m a^{-1} at Haast, to 9.0–9.4 m a^{-1} in the Hokitika region, up to a maximum of 10.9 m a^{-1} at Franz Josef (Figure 5.2). The peak magnitudes of the interpolated profiles across the Hokitika and Franz Josef transects are somewhat lower than the 13 m a^{-1} peak of the 'invariant' orographic profile subjectively estimated by Henderson and Thompson (1999). In this thesis, however, observations from short-term stations were not normalised to observations from nearby long-term stations, and no allowance was made for undercatch. The mean annual profiles developed in this thesis do support the hypothesis — put forward by Henderson and Thompson (1999) and implicit in Griffiths and McSaveney (1983) — that the peak magnitude of the precipitation profile is related to the elevation of the Main Divide in the vicinity of the profile.

The analysis presented in Section 5.2.1 indicates that orographic forcing causes mean annual precipitation to peak around 7–11 km southeast of the Alpine Fault in the Hokitika, Franz Josef (Figure 6.1) and Haast regions. This is again consistent with previous research by Henderson and Thompson (1999), which showed that rainfall during storms in the Southern Alps peaked within a slender zone approximately 10 km southeast of the Alpine Fault and 10–20 km northwest of the highest ground.

Peak precipitation thus occurs some considerable distance 'upwind' of the line of maximum topographic elevation. After much of the moisture in the atmospheric water column has condensed and precipitated northwest of the Main Divide, the consequent lee-side drying in the rain shadow of the
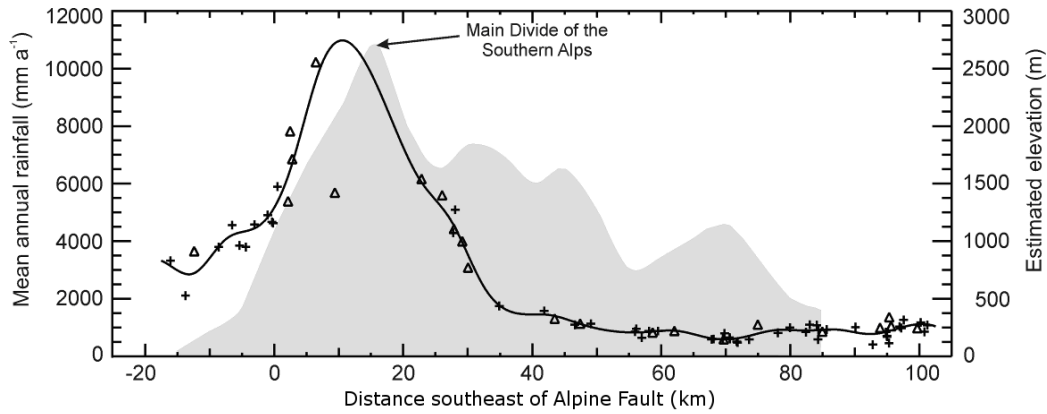
Figure 6.1 Mean annual precipitation (mm a^{-1}) in the Franz Josef transect from 1971 to 2000, versus distance southeast of the Alpine Fault (km). '+' symbols denote CliDB gauges, '△' symbols denote WRA gauges. The curved line shows the cubic spline fitted to observations. Shading indicates topographic elevation (m a.s.l.) in the vicinity of Franz Josef, using the right-hand ordinate axis. Topographic elevations were added by Purdie (2011), using topographic data from Henderson and Thompson (1999).

mountains reduces the correlation between local topographic elevation and observed rainfall. As shown in previous research (Wratt et al. 2000; Tait et al. 2006) and in Section 5.1 of this thesis, local topographic elevation alone explains very little of the spatial variation in rainfall in the Southern Alps. Thus when interpolating point-based observations using mathematical techniques such as thin-plate smoothing splines, a direct dependence upon local topographic elevation does not produce particularly accurate surfaces of observed rainfall in the Southern Alps region (Leathwick et al. 2002; Tait et al. 2006). This also has implications for the downscaling of simulated rainfall: in order to increase the spatial resolution of rainfall simulated by the mesoscale HadRM3P regional climate model, an alternative approach is necessary.

The basic objective of the methodology in this thesis was to use the dominant spatial characteristic of observed rainfall in the Southern Alps — the precipitation profile across the whole mountain range — as a predictor of the distribution of precipitation at high spatial resolutions. In this approach, es-

tablishing the observed profile becomes very important and one must consider the uncertainties involved. At high elevations in the heavily glaciated Aoraki Mount Cook region, observational data are scarce and the prevalence of both snow and strong winds makes rain gauges very susceptible to undercatch. If the anomalously low observations at Almer Hut are disregarded, then across the Franz Josef transect, the splined profile normal to the Alpine Fault is unguided by observational data for approximately 16 km between Luncheon Rock (680 m a.s.l.) and Panorama Ridge (1509 m a.s.l.) (Figure 6.1).

In research independent of the analysis in the present thesis, Kees (2011) used ground-penetrating radar (GPR) to measure snow thicknesses in high-altitude locations in the central Southern Alps during 2009. GPR readings were obtained at three points in the Davis Snowfield in the Franz Josef névé (2050, 2300 and 2450 m a.s.l.), one point in the Annette Plateau (2250 m a.s.l.) and one point in the Jollie Valley (approximately 2000 m a.s.l.). The snow thicknesses were converted to water equivalent using snow density measurements in associated snowpits. These water equivalents were then compared to 30-year norms (1971–2000) from nearby climate stations, in order to derive a precipitation index and estimates of mean annual precipitation at the GPR locations. Figure 6.2 shows the profile of observed mean annual precipitation across the Franz Josef transect, with a cubic spline fitted only to observations from rain gauges, as presented earlier in Figure 5.2d. The five GPR-based estimates of mean annual precipitation, provided by Kees (2011), have been added to Figure 6.2. It must be acknowledged that the Kees (2011) estimates are based on GPR measurements in just one accumulation year, and due to interannual variability it would be preferable to make this comparison in the year of measurement (2009). However, the three GPR-based estimates of 9.9–11.3 m a^{-1} in the Franz Josef névé do compare well to the spline's 10.9 m a^{-1} peak only 2–3 km to the northwest. The GPR measurements in the Franz Josef névé cast further doubt upon the validity of the relatively low 5.7 m a^{-1} of precipitation observed at Almer Hut ('○' symbol in Figure 6.2) from 1991 to 1996, which was excluded from the fitted spline. All of the GPR-based estimates, including those for the Annette Plateau and the Jollie Valley east of the Main Divide, are within 0.5 m a^{-1}
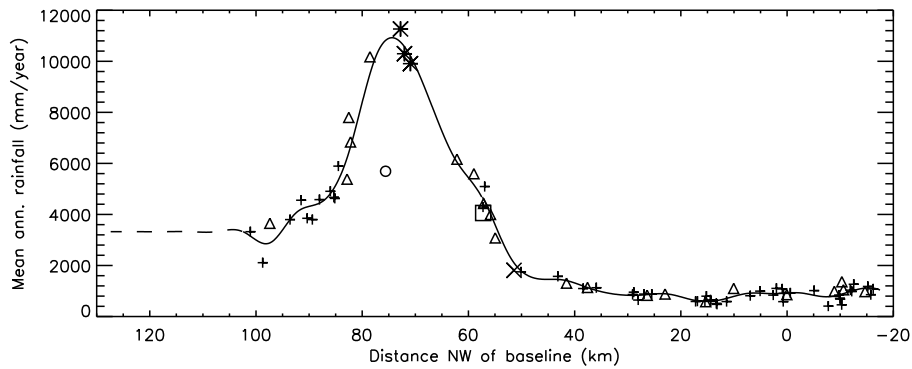
Figure 6.2 Mean annual precipitation (mm a^{-1}) in the Franz Josef transect versus distance northwest of baseline (km). The following symbols denote estimated precipitation, as derived from observations from rain gauges and ground-penetrating radar (GPR): '+' (CliDB gauges), '△' (WRA gauges), '○' (Almer Hut gauge), '*' (Franz Josef névé GPR), '□' (Annette Plateau GPR), '×' (Jollie Valley GPR). The curved line shows the cubic spline fitted to observations from the CliDB gauges and WRA gauges, excluding Almer Hut. Mean annual precipitation at GPR sites was estimated by Kees (2011), based on GPR measurements in 2009.

of the spline fitted to observations from rain gauges.

Using additional rain gauges at high elevations, Kerr (2009) estimated mean annual precipitation in the northwesternmost part of the Pukaki catchment, along the southeast flank of the Main Divide, to be up to 13 m a^{-1}. Kerr (2009) suggested that the precipitation profile in the Aoraki Mount Cook region may exhibit a dual peak, with the second peak located near or slightly 'downwind' of the Main Divide. The data from rain gauges used in this thesis are insufficient to diagnose a second peak in Franz Josef region (Figure 6.1), but Figure 5.2b does suggest the presence of a second peak in the Hokitika region. Such a peak could be produced by orographic forcing of air that approaches the Southern Alps from the south or east. However, a comparison of the daily profile to reanalyses (Section 5.2.2) indicates that comparatively little precipitation falls near the Main Divide when the wind — diagnosed at a location north of the central Southern Alps — blows from the south or east (Figure 5.5). The use of data from additional reanalysis grid points southeast of the Main Divide would aid further analysis, to en-

sure that the diagnosed wind direction is representative of airflow on both sides of the mountain range. Since the annual climatology is dominated by northwesterly and westerly precipitation, if a significant second peak does indeed exist in the central Southern Alps, this second peak may be formed primarily when wind approaches the mountain range from the northwest and west. Results from a high-resolution dynamic weather model of the European Alps suggest that an atmospheric freezing level near a mountain's summit may encourage the formation of a dual peak in the orographic precipitation profile (Zängl 2008), and Kerr (2009) suggested that such conditions may be present in the Aoraki Mount Cook region. Kerr et al. (2011) will begin a two-year campaign of precipitation observations in the late austral summer of 2011. Newly designed gauges, capable of recording high magnitudes of precipitation with reduced undercatch, will be installed in the wettest and most data-sparse areas of the central Southern Alps, east of Westland Tai Poutini National Park. With these new observations, Kerr et al. (2011) hope to refine the profile of mean annual precipitation in this region.

While there is still some uncertainty about the exact distribution of observed rainfall in the Aoraki Mount Cook region, the $Surf_{Obs.A}$ surface is within 0.6 m a^{-1} of the five GPR-based estimates at high elevations independently produced by Kees (2011), with the caveat that the GPR readings were taken in the single year of 2009. $Surf_{Obs.A}$ also generally compares well to the surface of mean annual precipitation in the Pukaki catchment independently developed by Kerr (2009) (Figure 5.10). These results suggest that the merger of two-dimensional transects — a method used previously by Dr Brian Anderson of the Antarctic Research Centre — is a suitable way to develop surfaces of precipitation in this region.

Dr Nick Golledge of the ARC found that the use of $Surf_{Obs.A}$ within the Parallel Ice Sheet Model led to improved correlations between simulated glacial extent and geological evidence in the Southern Alps (Figure 5.11). At the time of writing, $Surf_{Obs.A}$ was being used by several other researchers at the Victoria University of Wellington. Anderson and Mackintosh (2011) used $Surf_{Obs.A}$ within an energy-balance model, in order to analyse the sensitivity of maritime and debris-covered glaciers in the Southern Alps. Sat-

tler et al. (2011) are using $\text{Surf}_{\text{Obs.A}}$ to help determine distribution patterns of rockglaciers in Canterbury and debris-flow activity across the Southern Alps. Doughty et al. (2011) aim to estimate late-glacial temperatures in New Zealand by replicating past glacial extents in the Ben Ohau and Arrowsmith ranges. In their research, $\text{Surf}_{\text{Obs.A}}$ is being used to calibrate monthly precipitation data fed into a coupled energy-balance/ice-flow model.

Having established that $\text{Surf}_{\text{Obs.A}}$ provides a reasonably good representation of the observed spatial distribution of mean annual precipitation in the central Southern Alps, the surface was incorporated into the downscaling of precipitation simulated at 30-km resolution by the HadRM3P regional climate model. The approach taken was a trivariate thin-plate smoothing spline interpolation, with $\text{Surf}_{\text{Obs.A}}$ employed as an independent variable. The use of a square-root transformation produced a downscaled surface ($\text{Surf}_{\text{Rcm.A.DsT}}$) that was overfitted to the RCM grid points, and when validated directly against long-term rain gauges, $\text{Surf}_{\text{Rcm.A.DsT}}$ had a higher RMSE than the surface downscaled without transformation ($\text{Surf}_{\text{Rcm.A.Ds}}$). The $\text{Surf}_{\text{Rcm.A.Ds}}$ surface is therefore regarded as a better representation of mean annual precipitation in the Southern Alps from 1971 to 2000. As shown in Section 5.4.2, the downscaling without transformation reduced the RMSE of HadRM3P-simulated rainfall by 53% when compared directly with observations from long-term rain gauges in the central Southern Alps, and by 45% when compared with a precipitation surface for the Pukaki catchment produced by Kerr (2009).

The distribution of mean annual rainfall in the Southern Alps at spatial resolutions finer than 30 km can thus be estimated with some success by assuming a dependence upon historical spatial patterns of precipitation. This finding is consistent with research by Tait et al. (2006) into the production of historical daily precipitation surfaces for New Zealand; the present analysis may also represent an advance in interpolated precipitation surfaces within elevated regions of the Southern Alps. The trivariate spline interpolation could just as easily be applied to a future scenario of New Zealand rainfall, generated by the RCM nested within a GCM simulation. This method could be used to produce data for environmental models and other applications that

require high-resolution annual surfaces of precipitation without day-to-day temporal variations.

In the context of downscaling future climatic projections, one must consider the implications of potential changes to the distribution of mean annual precipitation. GCM simulations for the IPCC Fourth Assessment Report (AR4) project enhanced warming in the tropical upper troposphere, accompanied by an expansion of the Hadley circulation (Meehl et al. 2007). In the Southern Hemisphere, the surface meridional temperature gradient is expected to steepen, accentuating a poleward movement of the primary storm tracks (Yin 2005). Descending air from the poleward limb of an expanded Hadley Cell is forecast to increase sea level pressure in the southern mid-latitudes. The AR4 GCM simulations have been downscaled in the New Zealand region, via both statistical regression and the HadRM3P RCM (Ministry for the Environment 2008). A steepening of the meridional sea level pressure gradient to the north of New Zealand is expected to increase westerlies over New Zealand during winter and spring, leading to increased precipitation west of the Southern Alps. This may exaggerate the current east-west gradient of mean annual rainfall across the South Island and reduce the skill of downscaling methods that make assumptions about its stationarity.

Downscaling techniques therefore often classify climatic variables according to the state of synoptic-scale meteorological predictors (Mullan et al. 2001; Wilby et al. 2004; Christensen et al. 2007). Kerr (2009) found that the spatial distribution of daily precipitation in the Pukaki catchment varied according to the horizontal wind direction at 850 hPa north and south of the catchment. As shown in Section 5.2.2, variations in wind direction north of the central Southern Alps have a profound influence upon the shape of the daily precipitation profile across the whole mountain range. On days when the mean horizontal wind at 850 hPa blows from the east, southeast or south quadrants, the daily precipitation peak along the Southern Alps is located approximately 80 km southeast of the Alpine Fault, well to the southeast of the Main Divide. Consequently, pressure-based indices of synoptic-scale circulation around New Zealand, such as those developed by Trenberth (1976)

or Kidson (2000), are also likely to be good predictors of changes in the precipitation profile. The influence of atmospheric temperature upon the precipitation profile was difficult to isolate due to the strong correlation between temperature and wind direction. Greater insight into the influence of temperature variations may be gained by a more sophisticated statistical analysis or high-resolution numerical modelling.

Since wind direction appears to be the dominant atmospheric influence upon the spatial distribution of precipitation in the Southern Alps, a wind-based surface was incorporated into the downscaling of daily precipitation simulated by HadRM3P during a northwesterly storm (Section 5.5). The general pattern of simulated precipitation appeared realistic and its mean bias was substantially reduced after being downscaled with surfaces of mean daily precipitation on all days ($Surf_{Obs.D}$) and northwesterly days ($Surf_{Obs.D.NW}$). However, the use of the northwesterly-based surface as a predictor did not improve downscaling skill, partly due to similarities between the $Surf_{Obs.D}$ and $Surf_{Obs.D.NW}$ surfaces. The 65 mm RMSE of both downscaled surfaces was still relatively high. Difficulties are posed by the complex spatial distribution of daily precipitation in highly elevated regions, which is considerably more patchy and 'noisy' than that of mean annual precipitation. Minimising the GCV during the downscaling resulted in a slightly distorted surface that fitted exactly to the RCM grid points; a low fixed signal was necessary to prevent such distortion. This probably indicates that the 30-km grid of HadRM3P is too sparse to adequately represent the complexity of daily rainfall distributions in the Southern Alps during heavy precipitation events. This problem will be mitigated if the spatial resolution of the RCM is increased to 10–12 km in future versions of the model.

By using any historical precipitation surface as an independent variable during the downscaling of future climatic scenarios, one makes the implicit assumption that historical precipitation patterns will be a good predictor of future precipitation; one must ask whether this is a reasonable model. Regression models may encounter similar problems by assuming temporally constant relationships between local climatic variables and synoptic-scale circulation, which may not be valid in a future world climate perturbed by

higher atmospheric concentrations of carbon dioxide and other greenhouse gases. Both of these downscaling techniques also require an accurate representation of historical precipitation, which can be difficult to ascertain in a rugged and isolated region such as the Southern Alps. A simpler approach might be to employ a predictor that is both known with certainty and essentially static for the next few centuries. While local topographic elevation has been shown to be a poor predictor of precipitation in the Southern Alps, the distinct cross-mountain profile of rainfall suggests that distance perpendicular to the main orographic axis could be a good alternative. The use of the Main Divide as a line of reference is problematic: it is too irregular and it does not always represent the line of highest ground, with higher ranges to the west at Mount Hooker and Mount Dechen, for example. The Alpine Fault, however, is approximately straight, and marks a clear change in topographic elevation across the Southern Alps.

A thin-plate smoothing spline does not require a temporally constant relationship between its independent and dependent variables. Each independent variable simply needs to be a good predictor of the dependent variable during the period being downscaled. Even if the exact relationship between rainfall and topography changes in the future, surface precipitation in the Southern Alps region will certainly still be greatly affected by its position with respect to the Alpine Fault. During a trivariate spline interpolation, a simple exponential or logarithmic transformation could be applied to the distance between each RCM grid point and the Alpine Fault, to help reproduce the observed east-west gradient of rainfall in the South Island. Any empirical calibration would still make some assumption of stationarity, but this is to some extent unavoidable; even dynamic climate models are tuned to accurately reproduce historical climate before being used to make future projections. This approach would have parallels with the logistic-growth model developed by Griffiths and McSaveney (1983) and is worth investigating in future research.

Chapter 7

Conclusion

The central theme of this thesis has been the spatial distribution of precipitation in the central Southern Alps, and the manner in which it is influenced by topography and wind direction. The main axis of the Southern Alps runs parallel to the New Zealand Alpine Fault, at which point the topographic profile rises sharply and air moving horizontally is forced vigorously upward. The essence of the present analysis has been two-dimensional profiles of observed precipitation across the Southern Alps from 1971 to 2000, which were created objectively using a cubic spline interpolation. This analysis indicates that distance from the Alpine Fault is the most influential determinant of mean annual rainfall in the central Southern Alps, in agreement with previous work (Henderson and Thompson 1999). In 4 transects of the Hokitika, Franz Josef and Haast regions, the mean annual precipitation maxima of the objectively interpolated profiles are consistently located 7–11 km southeast of the Alpine Fault. Due to a shortage of available observations in the Milford transect, no conclusions are drawn for Fiordland.

Local topographic elevation explains very little (0.3%) of the variation in mean annual precipitation recorded by individual rain gauges in the Southern Alps. Peak mean annual precipitation across the interpolated profiles ranges from 8.6 m a^{-1} at Haast, to 9.0–9.4 m a^{-1} in the Hokitika region, up to a maximum of 10.9 m a^{-1} at Franz Josef, although higher levels were recorded by individual gauges. The magnitude of peak precipitation across 4 transects of the Southern Alps is thus related to the elevation of the Main Divide across

each transect, in agreement with Henderson and Thompson (1999).

Peak mean annual precipitation is consistently located northwest of the Main Divide. The distance from the annual precipitation maxima southeast to the Main Divide ranges from 4–5 km in the Franz Josef region, up to a maximum of 25 km in the Haast region, where the Main Divide deviates significantly to the southeast. The magnitude and shape of the mean daily precipitation profile are strongly influenced by the wind direction north of the central Southern Alps, as evidenced by comparisons of observed daily rainfall to wind vectors from NCEP/NCAR Reanalysis 1. On days when the mean horizontal wind at 850 hPa blows from the east, southeast or south quadrants, the daily precipitation peak along the Southern Alps is located approximately 80 km southeast of the Alpine Fault, well to the southeast of the Main Divide.

Rain gauges are sparse in the Aoraki Mount Cook region. The interpolated profile of 1971–2000 mean annual precipitation across the Franz Josef transect is however supported by independent estimates from Kees (2011), which were based on GPR measurements at high elevations of the Aoraki Mount Cook region in 2009. The Surf$_{Obs.A}$ surface of mean annual precipitation in the central Southern Alps, developed in this thesis, also generally compares well to an independently developed surface for the Pukaki catchment (Kerr 2009). The two-dimensional nature of its construction has made Surf$_{Obs.A}$ unrealistically smooth, but the sparsity of observations necessitates some form of idealised model in order to describe the spatial distribution of precipitation throughout the region. This surface is currently being used by several researchers at VUW, to gain further understanding of glacial behaviour in the central Southern Alps.

A trivariate thin-plate smoothing spline was used to interpolate mean annual precipitation simulated by the HadRM3P regional climate model in the central Southern Alps during the 30-year period from 1971 to 2000, with the Surf$_{Obs.A}$ surface being employed as an independent variable. This method of downscaling reduced the RMSE of HadRM3P-simulated rainfall by 53% when compared directly with observations from long-term rain gauges in the central Southern Alps, and by 45% when validated against an independently

developed surface of mean annual precipitation in the Pukaki catchment (Kerr 2009). This result indicates that the observed rainfall profile across the Southern Alps can be successfully integrated into a trivariate thin-plate smoothing spline, in order to increase the spatial resolution and accuracy of mean annual precipitation simulated by a regional climate model. This approach may also be applicable in other north-south trending mountain ranges that intersect primarily zonal circulation and exhibit a similarly distinct profile of orographically enhanced rainfall.

The HadRM3P RCM generally simulated realistic spatial patterns of rainfall in the central Southern Alps during an historic and intense northwesterly storm. However, the 30-km resolution of the RCM is too coarse to accurately represent the steep precipitation gradients of daily rainfall distributions in mountainous regions during heavy precipitation events. This led to only moderate improvements in the accuracy of the simulated daily rainfall after downscaling via a trivariate thin-plate smoothing spline. This issue will be mitigated in future versions of the RCM, which will run on a more powerful supercomputer and have a higher spatial resolution.

References

Anagnostopoulou C., Tolika K., Maheras P., Kutiel H., Flocas H.A. (2008). Performance of the general circulation HadAM3P model in simulating circulation types over the Mediterranean region. *International Journal of Climatology*, 28(2):185.

Anderson B., Lawson W., Owens I., Goodsell B. (2008). Response of Franz Josef Glacier 'Ka Roimata o Hine Hukatere' to climate change. *Global and Planetary Change*, 63(1):23–30.

Anderson B., Mackintosh A. (2006). Temperature change is the major driver of late-glacial and Holocene glacier fluctuations in New Zealand. *Geology*, 34(2):121–124.

Anderson B., Mackintosh A. (2011). Controls on glacier sensitivity for maritime and debris-covered glaciers. *Journal of Geophysical Research*. In prep.

Anderson B., Mackintosh A., Stumm D., George L., Kerr T., Winter-Billington A., Fitzsimons S. (2010). Climate sensitivity of a high-precipitation glacier in New Zealand. *Journal of Glaciology*, 56(195):114–128.

Barry R.G. (2008). *Mountain Weather and Climate*. Cambridge University Press, 3rd edition.

Barry R.G., Chorley R.J. (2003). *Atmosphere, Weather, and Climate*. Routledge, 8th edition.

Batt G.E., Braun J., Kohn B.P., McDougall I. (2000). Thermochronological analysis of the dynamics of the Southern Alps, New Zealand. *Geological Society of America Bulletin*, 112(2):250–266.

Bueler E., Khroulev C., Aschwanden A., Joughin I., Smith B. (2010). Modeled and observed fast flow in the Greenland ice sheet. *Geophysical Research Letters*. Submitted.

Chater A., Sturman A. (1998). Atmospheric conditions influencing the spillover of rainfall to lee of the Southern Alps, New Zealand. *International Journal of Climatology*, 18(1):77–92.

Chinn T., Winkler S., Salinger M.J., Haakensen N. (2005). Recent glacier advances in Norway and New Zealand: a comparison of their glaciological and meteorological causes. *Geografiska Annaler. Series A, Physical Geography*, 87(1):141–157.

Chinn T.J. (1979). How wet is the wettest of the wet West Coast? *New Zealand Alpine Journal*, 32:85–87.

Chinn T.J. (1996). New Zealand glacier responses to climate change of the past century. *New Zealand Journal of Geology & Geophysics*, 39(3):415–428.

Chinn T.J. (2001). Distribution of the glacial water resources of New Zealand. *Journal of Hydrology (NZ)*, 40(2):139–187.

Chinn T.J.H. (1995). Glacier fluctuations in the Southern Alps of New Zealand determined from snowline elevations. *Arctic and Alpine Research*, 27(2):187–198.

Christensen J.H., Hewitson B., Busuioc A., Chen A., Gao X., Held I., Jones R., Kolli R.K., Kwon W.T., Laprise R., Rueda V.M., Mearns L., Menndez C.G., Risnen J., Rinke A., Sarr A., Whetton P. (2007). Regional climate projections. In Solomon S., Qin D., Manning M., Chen Z., Marquis M., Averyt K.B., Tignor M., Miller H.L., editors, *Climate Change 2007: The Physical Science Basis. Contribution of Working Group I to the Fourth Assessment Report of the Intergovernmental Panel on Climate Change*, chapter 11, pages 847–940. Cambridge University Press, Cambridge, United Kingdom and New York, USA.

Clark M., Rupp D., Woods R., Zheng X., Ibbitt R., Slater A., Schmidt J., Uddstrom M. (2008). Hydrological data assimilation with the ensemble Kalman filter: Use of streamflow observations to update states in a distributed hydrological model. *Advances in Water Resources*, 31(10):1309–1324.

Craven P., Wahba G. (1979). Smoothing noisy data with spline functions: estimating the correct degree of smoothing by the method of generalized cross-validation. *Numerische Mathematik*, 31(4):377–403.

da Rocha R.P., Morales C.A., Cuadra S.V., Ambrizzi T. (2009). Precipitation diurnal cycle and summer climatology assessment over South America: An evaluation of Regional Climate Model version 3 simulations. *Journal of Geophysical Research-Atmospheres*, 114, doi:10.1029/2008JD010212.

de Boor C. (1978). *A Practical Guide to Splines*, volume 27 of *Applied Mathematical Sciences*. Springer-Verlag, New York.

Doughty A., Mackintosh A., Anderson B., Kaplan M., Vandergoes M., Denton G., Barrell D., Schaefer J. (2011). Modelling late-glacial ice extent in the Ben

Ohau Range to estimate past temperatures. In *2011 Annual Workshop of the New Zealand Snow and Ice Research Group (SIRG)*, Fox Glacier Township, New Zealand. 9–11 February 2011.

Dravitzki S.M. (2009). *Precipitation in the Waikato River Catchment.* Phd, School of Geography, Environment and Earth Sciences, Victoria University of Wellington, New Zealand.

Drost F., Renwick J., Bhaskaran B., Oliver H., McGregor J. (2007). Simulation of New Zealand's climate using a high-resolution nested regional climate model. *International Journal of Climatology*, 27(9):1153–1169.

Dykes R.C., Brook M.S. (2010). Terminus recession, proglacial lake expansion and 21st century calving retreat of Tasman Glacier, New Zealand. *New Zealand Geographer*, 66(3):203–217.

Eby M., Zickfeld K., Montenegro A., Archer D., Meissner K.J., Weaver A.J. (2009). Lifetime of Anthropogenic Climate Change: Millennial Time Scales of Potential CO_2 and Surface Temperature Perturbations. *Journal of Climate*, 22(10):2501–2511, doi:10.1175/2008JCLI2554.1.

Fitzharris B.B., Chinn T.J., Lamont G.N. (1997). Glacier balance fluctuations and atmospheric circulation patterns over the Southern Alps, New Zealand. *International Journal of Climatology*, 17:745–763.

Fitzharris B.B., Hay J.E., Jones P.D. (1992). Behaviour of New Zealand glaciers and atmospheric circulation changes over the past 130 years. *The Holocene*, 2(2):97106.

Frei C., Schär C. (1998). A precipitation climatology of the Alps from high-resolution rain-gauge observations. *International Journal of Climatology*, 18(8):873–900.

Fujiyoshi Y., Kondo H., Inoue J., Yamada T. (1987). Characteristics of precipitation and vertical structure of air temperature in the northern Patagonia. *Bulletin of Glacier Research*, 4:15–23.

Giorgi F., Shields Brodeur C., Bates G.T. (1994). Regional climate change scenarios over the United States produced with a nested regional climate model. *Journal of Climate*, 7(3):375–399.

Goodison B.E., Louie P.Y.T., Yang D. (1998). WMO Solid Precipitation Measurement Intercomparison - Final Report. Technical report, World Meteorological Organization. Instruments and Observing Methods - Report No. 67, WMO/TD - No. 872.

Gordon N. (1986). The Southern Oscillation and New Zealand weather. *Monthly Weather Review*, 114(2):371–387.

Griffiths G.A., McSaveney M.J. (1983). Distribution of mean annual precipitation across some steepland regions of New Zealand. *New Zealand Journal of Science*, 26(2):197–209.

Hay J.E., Fitzharris B.B. (1988). The synoptic climatology of ablation on a New Zealand glacier. *International Journal of Climatology*, 8(2):201–215.

Haylock M.R., Cawley G.C., Harpham C., Wilby R.L., Goodess C.M. (2006). Downscaling heavy precipitation over the United Kingdom: a comparison of dynamical and statistical methods and their future scenarios. *International Journal of Climatology*, 26(10):1397–1415.

Hegerl G.C., Zwiers F.W., Braconnot P., Gillett N.P., Luo Y., Orsini J.A.M., Nicholls N., Penner J.E., Stott P.A. (2007). Understanding and attributing climate change. In Solomon S., Qin D., Manning M., Chen Z., Marquis M., Averyt K.B., Tignor M., Miller H.L., editors, *Climate Change 2007: The Physical Science Basis. Contribution of Working Group I to the Fourth Assessment Report of the Intergovernmental Panel on Climate Change*, chapter 9. Cambridge University Press, Cambridge, United Kingdom and New York, NY, USA.

Henderson R.D. (1993). Extreme storm rainfalls in the Southern Alps, New Zealand. *IAHS Publication*, pages 113–120.

Henderson R.D., Thompson S.M. (1999). Extreme rainfalls in the Southern Alps of New Zealand. *Journal of Hydrology (New Zealand)*, 38(2):309–330.

Hessell J.W.D. (1982). *The climate and weather of Westland.* Miscellaneous Publication 115 (10). Ministry of Transport, New Zealand Meteorological Service, Wellington, New Zealand.

Hessell J.W.D. (1983). Climatic effects on the recession of the Franz Josef Glacier. *New Zealand Journal of Science*, 26(2).

Holton J.R. (1992). *An Introduction to Dynamic Meteorology.* Academic Press, London, United Kingdom, 3rd edition.

Hooker B.L., Fitzharris B.B. (1999). The correlation between climatic parameters and the retreat and advance of Franz Josef Glacier, New Zealand. *Global and Planetary Change*, 22:39–48.

Hudson D.A., Jones R.G. (2002). Regional climate model simulations of present-day and future climates of southern Africa. Technical report, Hadley Centre, Met Office.

Hutchinson M.F. (1995). Interpolating mean rainfall using thin plate splines. *International Journal of Geographic Information Systems*, 9(4):385–403.

Hutchinson M.F. (1998a). Interpolation of rainfall data with thin plate smoothing splines. Part I: Two dimensional smoothing of data with short range correlation. *Journal of Geographic Information and Decision Analysis*, 2(2):139–151.

Hutchinson M.F. (1998b). Interpolation of rainfall data with thin plate smoothing splines. Part II: Analysis of topographic dependence. *Journal of Geographic Information and Decision Analysis*, 2(2):152–167.

Hutchinson M.F. (2000). *ANUSPLIN Version 4.1 User Guide.* Centre for Resource and Environmental Studies, Australian National University, Canberra.

Hutchinson M.F. (2011). ANUSPLIN Version 4.3. `http://fennerschool.anu.edu.au/publications/software/anusplin.php`.

Hutchinson M.F., Gessler P.E. (1994). Splines - more than just a smooth interpolator. *Geoderma*, 62(1-3):45–67.

Hutchinson M.F., McKenney D.W., Lawrence K., Pedlar J.H., Hopkinson R.F., Milewska E., Papadopol P. (2009). Development and testing of Canada-wide interpolated spatial models of daily minimum–maximum temperature and precipitation for 1961–2003. *Journal of Applied Meteorology and Climatology*, 48(4):725–741.

Johns T.C., Durman C.F., Banks H.T., Roberts M.J., McLaren A.J., Ridley J.K., Senior C.A., Williams K.D., Jones A., Rickard G.J. et al. (2006). The new Hadley Centre climate model (HadGEM1): Evaluation of coupled simulations. *Journal of Climate*, 19(7):1327–1353.

Jones R.G., Murphy J.M., Noguer M. (1995). Simulation of climate change over Europe using a nested regional-climate model. I: Assessment of control climate, including sensitivity to location of lateral boundaries. *Quarterly Journal of the Royal Meteorological Society*, 121(526):1413–1449.

Jones R.G., Noguer M., Hassell D.C., Hudson D., Wilson S.S., Jenkins G.J., Mitchell J.F.B. (2004). *Generating High Resolution Climate Change Scenarios Using PRECIS.* Hadley Centre, United Kingdom Met Office, Exeter, United Kingdom.

Kalnay E. (2003). *Atmospheric Modeling, Data Assimilation and Predictability.* Cambridge University Press, Cambridge, United Kingdom.

Kalnay E., Kanamitsu M., Kistler R., Collins W., Deaven D., Gandin L., Iredell M., Saha S., White G., Woollen J. et al. (1996). The NCEP/NCAR 40-year

reanalysis project. *Bulletin of the American Meteorological Society*, 77(3):437–471.

Kees L. (2011). Assessment of a snow storage gradient across a maritime mountain environment; a GPR investigation. Master's thesis, Victoria University of Wellington, New Zealand.

Kerr T., Henderson R., Sood A. (2011). Design of a precipitation observation campaign to investigate the precipitation distribution in Westland Tai Poutini National Park, New Zealand. In *2011 Annual Workshop of the New Zealand Snow and Ice Research Group (SIRG)*, Fox Glacier Township, New Zealand. 9–11 February 2011.

Kerr T.R. (2009). *Precipitation Distribution in the Lake Pukaki Catchment, New Zealand.* Phd, University of Canterbury, New Zealand.

Kerr T.R. (2010). Personal communication. 16 March 2010, Christchurch, New Zealand.

Kidson J.W. (2000). An analysis of New Zealand synoptic types and their use in defining weather regimes. *International Journal of Climatology*, 20:299–316.

Kidson J.W., Thompson C.S. (1998). A comparison of statistical and model-based downscaling techniques for estimating local climate variations. *Journal of Climate*, 11(4):735–753.

Kidston J., Renwick J.A., McGregor J. (2009). Hemispheric-Scale Seasonality of the Southern Annular Mode and Impacts on the Climate of New Zealand. *Journal of Climate*, 22(18):4759–4770, doi:10.1175/2009JCLI2640.1.

Kundzewicz Z.W., Mata L.J., Arnell N., Dll P., Kabat P., Jimnez B., Miller K., Oki T., Sen Z., Shiklomanov I. (2007). Freshwater resources and their management. In Parry M.L., Canziani O.F., Palutikof J.P., van der Linden P., Hanson C., editors, *Climate Change 2007: Impacts, Adaptation and Vulnerability. Contribution of Working Group II to the Fourth Assessment Report of the Intergovernmental Panel on Climate Change*, pages 173–210. Cambridge University Press, Cambridge, UK.

Leathwick J.R., Wilson G., Stephens R.T.T. (2002). Climate Surfaces for New Zealand. Technical Report LC9798/126, Biodiversity and Conservation Division, Landcare Research.

Leyland, CAE (1998). *Electricity Supply and Demand to 2015: On the Basis of Existing and Proposed Generating Capacities.* Leyland Consultants and Centre for Advanced Engineering, University of Canterbury, New Zealand, 4th edition.

McKerchar A.I., Pearson C.P., Fitzharris B.B. (1998). Dependency of summer lake inflows and precipitation on spring SOI. *Journal of Hydrology*, 205(1-2):66–80.

Meehl G.A., Stocker T.F., Collins W.D., Friedlingstein P., Gaye A.T., Gregory J.M., Kitoh A., Knutti R., Murphy J.M., Noda A., Raper S.C.B., Watterson I.G., Weaver A.J., Zhao Z.C. (2007). Global climate projections. In Solomon S., Qin D., Manning M., Chen Z., Marquis M., Averyt K.B., Tignor M., Miller H.L., editors, *Climate Change 2007: The Physical Science Basis. Contribution of Working Group I to the Fourth Assessment Report of the Intergovernmental Panel on Climate Change*, chapter 10, pages 747–845. Cambridge University Press, Cambridge, United Kingdom and New York, USA.

Ministry for the Environment (2008). Climate change effects and impacts assessment: A guidance manual for local government in new zealand. Technical Report WLG2007/62, Ministry for the Environment, Wellington, New Zealand. xviii + 149 p.

Mullan A.B., Wratt D.S., Renwick J.A. (2001). Transient model scenarios of climate changes for New Zealand. *Weather and Climate*, 21:3–34.

New Zealand Meteorological Service (1985). Climatic map series. part 6: annual rainfall. *New Zealand Meteorological Service Miscellaneous Publication 175*.

New Zealand Meteorological Service (2010). Understanding radar imagery. Website. `http://vaac.metservice.com/default/index.php?alias=chradar`.

NIWA (2007). Water Resources Archive: the backbone. *Freshwater Update*, 24. National Institute of Water & Atmospheric Research, New Zealand.

NIWA (2010a). National Climate Database. Website. `http://www.niwa.cri.nz/services/clidb`.

NIWA (2010b). Tideda - Time Dependent Data. Website. `http://www.niwa.co.nz/our-services/software/tideda`.

NOAA, NASA, USAF (1976). *US Standard Atmosphere*. National Oceanic and Atmospheric Administration, National Aeronautics and Space Administration, United States Air Force, Washington, D.C., United States.

Oerlemans J. (1997). Climate sensitivity of Franz Josef Glacier, New Zealand, as revealed by numerical modeling. *Arctic and Alpine Research*, 29(2):233–239.

Panziera L., Germann U. (2010). The relation between airflow and orographic precipitation on the southern side of the Alps as revealed by weather radar. *Quarterly Journal of the Royal Meteorological Society*, 136:222–238.

Pielke R.A., Cotton W.R., Walko R.L., Trembaek C.J., Lyons W.A., Grasso L.D.,

Nieholls M.E., Moran M.D., Wesley D.A., Lee T.J. (1992). A comprehensive meteorological modeling system - RAMS. *Meteorology and Atmospheric Physics*, 49:69–91.

Purdie H. (2011). *Controls on spatial and temporal variation in snow accumulation on glaciers in the Southern Alps, New Zealand*. PhD thesis, School of Geography, Environment and Earth Sciences, Victoria University of Wellington, New Zealand.

Randall D.A., Wood R.A., Bony S., Colman R., Fichefet T., Fyfe J., Kattsov V., Pitman A., Shukla J., Srinivasan J., Stouffer R.J., Sumi A., Taylor K. (2007). Climate models and their evaluation. In Solomon S., Qin D., Manning M., Chen Z., Marquis M., Averyt K., Tignor M., Millerw H., editors, *Climate Change 2007: The Physical Science Basis. Contribution of Working Group I to the Fourth Assessment Report of the Intergovernmental Panel on Climate Change*, chapter 8. Cambridge University Press, Cambridge, United Kingdom and New York, NY, USA.

Renwick J.A., Katzfey J.J., Nguyen K.C., McGregor J.L. (1998). Regional model simulations of New Zealand climate. *Journal of Geophysical Research*, 103:5973–5982.

Rew R., Davis G. (1990). NetCDF: an interface for scientific data access. *IEEE Computer Graphics and Applications*, 10(4):76–82.

Rojas M., Moreno P.I., Kageyama M., Crucifix M., Hewitt C., Abe-Ouchi A., Ohgaito R., Brady E.C., Hope P. (2009). The Southern Westerlies during the last glacial maximum in PMIP2 simulations. *Climate Dynamics*, 32(4):525–548, doi:10.1007/s00382-008-0421-7.

Saeed S., Liu Y., Rasul G. (2011). Multiyear hindcast simulations of summer monsoon over South Asia using a nested regional climate model—BCC_RegCM1.0. *Theoretical and Applied Climatology*, 103(1-2):249–264, doi:10.1007/s00704-010-0297-4.

Salinger M.J. (1982). New Zealand climate: Scenarios for a warm high-C0$_2$ world. *Weather and Climate*, 2:9–15.

Sattler K., Mackintosh A., Anderson B., de Roiste M. (2011). Debris-flow activity and the role of permafrost degradation in New Zealands Southern Alps. In *14th Biennial Meeting of the Australian & New Zealand Geomorphology Group*. Australian & New Zealand Geomorphology Group.

Schmidli J., Frei C., Vidale P.L. (2006). Downscaling from GCM precipitation:

a benchmark for dynamical and statistical downscaling methods. *International Journal of Climatology*, 26(5):679–689.

Schneider C., Glaser M., Kilian R., Santana A., Butorovic N., Casassa G. (2003). Weather observations across the southern Andes at 53° S. *Physical Geography*, 24(2):97–119.

Sevruk B. (1997). Regional dependency of precipitation-altitude relationship in the Swiss Alps. *Climatic Change*, 36(3):355–369.

Sinclair M.R. (1994). A diagnostic model for estimating orographic precipitation. *Journal of Applied Meteorology*, 33(10):1163–1175.

Sinclair M.R., Wratt D.S., Henderson R.D., Gray W.R. (1997). Factors affecting the distribution and spillover of precipitation in the Southern Alps of New Zealand - a case study. *Journal of Applied Meteorology*, 36(5):428–442.

Sturman A.P., Tapper N. (2006). *The Weather and Climate of Australia and New Zealand*. Oxford University Press, Victoria, Australia, 2nd edition.

Suggate R.P. (1990). Late Pliocene and Quaternary glaciations of New Zealand. *Quaternary Science Reviews*, 9(2-3):175–197.

Tait A., Turner R. (2005). Generating multiyear gridded daily rainfall over New Zealand. *Journal of Applied Meteorology*, 44(9):1315–1323.

Tait A., Zheng X. (2007). Analysis of the spatial interpolation error associated with maps of median annual climate variables. Technical report, National Institute of Water & Atmospheric Research.

Tait A.B., Henderson R., Turner R., Zheng X. (2006). Thin plate smoothing spline interpolation of daily rainfall for New Zealand using a climatological rainfall surface. *International Journal of Climatology*, 26(14):2097–2115.

Thompson C.S., Sinclair M.R., Gray W.R. (1997). Estimating long-term annual precipitation in a mountainous region from a diagnostic model. *International Journal of Climatology*, 17:997–1007.

Trenberth K.E. (1976). Fluctuations and trends in indexes of southern hemispheric circulation. *Quarterly Journal of the Royal Meteorological Society*, 102(431):65–75.

Uddstrom M., Oliver H., Andrews P., Moore S., Sherlock V. (2007). Weathering the storm - from weather prediction to forecasting hazards. *Water & Atmosphere*, 15(3):10–11.

United Kingdom Met Office (1998). *Unified Model User Guide*. United Kingdom Met Office, Bracknell, United Kingdom.

United Kingdom Met Office (2009). Atmospheric numerical model configurations. Website. `http://www.metoffice.gov.uk/science/creating/daysahead/nwp/um_config.h%tml`.

Uppala S., Kållberg P.W., Simmons A.J., Andrae U., Bechtold V.D.C., Fiorino M., Gibson J.K., Haseler J., Hernandez A., Kelly G.A. et al. (2005). The ERA-40 reanalysis. *Quarterly Journal of the Royal Meteorological Society*, 131(612):2961–3012.

Wahba G. (1990). *Spline Models for Observational Data*. Society for Industrial Mathematics.

Walcott R.I. (1998). Modes of oblique compression: Late Cenozoic tectonics of the South Island of New Zealand. *Reviews of Geophysics*, 36(1):1–26.

Wallace J., Hobbs P. (2006). *Atmospheric Science: An Introductory Survey*. Academic Press, 2nd edition.

Walter K. (2000). Index to Hydrological Recording Sites in New Zealand. Technical Report 73, National Institute of Water & Atmospheric Research, Wellington, New Zealand.

Weaver A.J., Eby M., Wiebe E.C., Bitz C.M., Duffy P.B., Ewen T.L., Fanning A.F., Holland M.M., MacFadyen A., Matthews H.D., Meissner K.J., Saenko O., Schmittner A., Wang H.X., Yoshimori M. (2001). The UVic Earth System Climate Model: Model description, climatology, and applications to past, present and future climates. *Atmosphere-Ocean*, 39(4):361–428.

Weaver A.J., Zickfeld K., Montenegro A., Eby M. (2007). Long term climate implications of 2050 emission reduction targets. *Geophysical Research Letters*, 34(19):L19703.

Webster S., Uddstrom M., Oliver H., Vosper S. (2008). A high-resolution modelling case study of a severe weather event over New Zealand. *Atmospheric Science Letters*, 9:119–128.

Weingartner R., Pearson C. (2001). A comparison of the hydrology of the Swiss Alps and the Southern Alps of New Zealand. *Mountain Research and Development*, 21(4):370–381.

Wilby R.L., Charles S.P., Zorita E., Timbal B., Whetton P., Mearns L. (2004). Guidelines for use of climate scenarios developed from statistical downscaling methods. Technical Report 2, IPCC Task Group on Data and Scenario Support for Impact and Climate Analysis (TGICA).

World Meteorological Organization (1983). *Guide to Climatological Practices*. Se-

creteriat of the World Meteorological Organization, Geneva, Switzerland, 2nd edition. WMO-No. 100.

Wratt D.S., Revell M.J., Sinclair M.R., Gray W.R., Henderson R.D., Chater A.M. (2000). Relationships between air mass properties and mesoscale rainfall in New Zealand's Southern Alps. *Atmospheric Research*, 52(4):261–282.

Wratt D.S., Ridley R.N., Sinclair M.R., Larsen H., Thompson S.M., Henderson R., Austin G.L., Bradley S.G., Auer A., Sturman A.P. (1996). The New Zealand Southern Alps Experiment. *Bulletin of the American Meteorological Society*, 77(4):683–692.

Yin J.H. (2005). A consistent poleward shift of the storm tracks in simulations of 21st century climate. *Geophysical Research Letters*, 32(18), doi:10.1029/2005GL023684.

Zängl G. (2008). The temperature dependence of small-scale orographic precipitation enhancement. *Quarterly Journal of the Royal Meteorological Society*, 134(634):1167–1182.

Zhang L., Hickel K., Dawes W., Chiew F., Western A., Briggs P. (2004). A rational function approach for estimating mean annual evapotranspiration. *Water Resources Research*, 40(2):W02502.

Appendix A

Rain gauges in the Southern Alps

This appendix contains details of rain gauges in the Southern Alps that were operational between 1 January 1971 and 31 December 2000, including precipitation recorded during this period. The gauges are separated into five tables, which correspond to the five transects of the Southern Alps (see Figure 3.2): northeast Hokitika, southwest Hokitika, Franz Josef, Haast and Milford. Within each table, gauges are listed from northwest to southeast. Gauges more than 20 km southeast of the domain's baseline have been omitted.

Table A.1 Rain gauges in the northeast Hokitika transect of the Southern Alps from 1 Jan 1971 to 31 Dec 2000. Total number of gauges: 84; CliDB gauges: 61; WRA gauges: 23. 'Begin Date' is the date of the first daily observation between 1 Jan 1971 and 31 Dec 2000; 'End Date' is the date of the last daily observation between 1 Jan 1971 and 31 Dec 2000; 'Obs. Years' is the number of years of observation by each gauge between 1 Jan 1971 and 31 Dec 2000. '$\bar{p}$ Daily' is mean daily precipitation; '$\bar{p}$ Annual' is mean annual precipitation.

Network/ Site No.	Archive	Station Name	Easting (NZMG)	Northing (NZMG)	Elevation (m a.s.l.)	NW Dist (km)	Begin Date	End Date	Obs. Years	$\bar{p}$ Daily (mm dy^{-1})	$\bar{p}$ Annual (mm a^{-1})
F21321	CDB	Rapahoe 1	2365867	5869819	12	128.7	1/1971	4/1972	1.3	5.6	2032
F21322	CDB	Rapahoe 2	2365640	5868814	10	128.1	5/1981	12/2000	18.7	8.1	2969
F21424	CDB	Runanga Carroll St	2366031	5865933		125.5	1/1988	12/1988	1.0	8.0	2936
F21423	CDB	Runanga	2366439	5866053	6	125.4	5/1987	8/1992	5.2	8.1	2968
F21331	CDB	Rewanui State Mine	2370923	5868367	192	124.6	1/1971	1/1985	14.1	10.4	3792
F21421	CDB	Greymouth Hbr	2362272	5860631	3	123.4	1/1971	6/1990	19.3	6.8	2474
F21422	CDB	Greymouth Aero	2361234	5859164	4	122.9	1/1971	12/2000	30.0	6.8	2476
F21512	CDB	Paroa	2359638	5853130	11	118.9	1/1971	12/2000	30.0	7.5	2725
F21431	CDB	Dobson	2371248	5860373	14	117.9	1/1971	12/2000	29.3	7.9	2876
F21532	CDB	Kokiri,Maori Gully Rd	2375734	5853906	143	110.1	9/1980	12/2000	20.3	9.5	3484
F20794	CDB	Hokitika Aws	2344807	5830564	38	109.5	12/1981	12/2000	16.9	8.1	2943
F20793	CDB	Hokitika Aero	2345217	5830574	39	109.3	1/1971	12/2000	30.0	7.9	2875
F21541	CDB	Arnold Power Station	2379214	5852528	75	106.9	1/1971	7/1995	24.5	8.5	3121
F21701	CDB	Kaniere	2346284	5827044	8	105.8	1/1971	5/1972	1.4	6.5	2378
F21601	CDB	Awatuna	2351781	5830173	6	105.1	1/1971	7/1981	10.2	7.0	2545
F21711	CDB	Kumara Reservoir	2361884	5832843	151	101.2	1/1988	10/1989	1.4	11.9	4356
216510	WRA	Moana at Lake Brunner rain	2384400	5846700	90	99.1	5/1989	1/2001	8.4	8.2	2990
F21631	CDB	Mitchells	2378471	5839737	130	97.0	4/1987	1/1994	6.8	10.7	3901
218117	WRA	Butchers Ck at Butchers Gully	2354671	5821990	140	96.7	8/1972	1/2001	27.5	10.7	3892
F21812	CDB	Lake Kaniere	2357709	5821529	133	94.6	1/1971	10/1989	18.3	10.6	3885
F21641	CDB	Inchbonnie	2383093	5833824	116	89.5	1/1971	12/2000	30.0	13.7	5009
F21653	CDB	Rotomanu 2	2393832	5838458	107	86.9	1/1971	12/2000	29.7	9.6	3519
217411	WRA	Taipo at SHB	2379300	5826800	105	86.1	2/1987	1/2001	11.9	13.1	4773
F21741	CDB	Taipo	2380425	5827552	122	86.0	1/1971	12/1971	1.0	10.0	3638
219211	WRA	Styx at Mt Browning	2371100	5809600	1160	77.0	3/1989	10/2000	6.6	25.3	9243
F21851	CDB	Otira Substation	2392534	5818548	383	71.6	1/1971	10/1987	16.8	13.9	5077
310311	WRA	Wilberforce at Clough Memorial	2374835	5804244	975	70.5	2/1981	8/1999	14.8	23.2	8461
310312	WRA	Wilberforce at Cabot Ridge	2370665	5797127	1450	67.2	4/1994	10/1998	3.4	26.6	9731
310510	WRA	Waimakariri at Carrington	2383440	5803758	823	65.0	3/1989	1/2001	11.1	17.9	6538
310314	WRA	Wilberforce at Griffiths Confluenc	2371448	5794215	700	64.4	4/1994	3/1998	3.5	19.1	6963
H21952	CDB	Arthurs Pass Store	2392495	5806548	748	61.9	1/1971	11/1991	16.3	12.5	4582

Table A.1 (continued)

Network/ Site No.	Archive	Station Name	Easting (NZMG)	Northing (NZMG)	Elevation (m a.s.l.)	NW Dist (km)	Begin Date	End Date	Obs. Years	$\bar{p}$ Daily (mm dy^{-1})	$\bar{p}$ Annual (mm a^{-1})
H21954	CDB	Arthurs Pass	2392660	5806440	740	61.8	1/1971	3/1991	18.7	12.5	4555
H21951	CDB	Arthurs Pass	2392723	5806310	738	61.6	1/1971	12/2000	29.8	12.2	4452
219510	WRA	Waimakariri at Arthurs Pass	2392500	5806100	750	61.6	1/1971	1/2001	28.6	12.6	4605
218810	WRA	Waimakariri at Ranger Stm	2416445	5814501	625	54.2	9/1978	1/2001	20.7	6.8	2475
311301	WRA	Rakaia at Fang Hill	2376928	5784436	625	53.3	5/1972	8/1999	24.0	6.4	2342
H31141	CDB	Glenthorne	2383521	5779863	610	45.7	1/1971	12/2000	29.8	4.1	1510
H31072	CDB	Cass	2408568	5796140	610	44.1	1/1971	2/1975	4.2	2.8	1014
H31241	CDB	Harper River	2384972	5776192	533	41.9	1/1971	12/2000	30.0	3.5	1273
311810	WRA	Waimakariri at Grasmere	2409682	5793803	600	41.5	12/1988	1/2001	12.0	2.9	1077
311610	WRA	Harper at Cockayne rain	2397600	5783900	740	40.7	4/1994	12/1997	3.6	4.7	1702
H31163	CDB	Ski Basin Edl	2402781	5785829	1554	39.2	5/1985	8/1986	1.3	4.0	1457
H31162	CDB	Ski Basin	2402781	5785829	1554	39.2	1/1971	9/1986	8.1	4.3	1578
311710	WRA	Camp Stream at Craigieburn rain	2404343	5785568	1370	38.0	4/1978	1/1994	15.7	5.9	2150
H31173	CDB	Camp Stream	2404734	5785749	1433	37.9	1/1971	7/1974	3.2	4.2	1545
H31172	CDB	Craigieburn Forest	2405427	5783093	914	35.4	1/1971	12/2000	29.9	4.0	1467
H31171	CDB	Flockhill	2410108	5785608	655	34.6	1/1971	3/1974	3.0	3.0	1087
H31091	CDB	Mt White Stn	2423341	5794455	610	34.0	7/1971	12/2000	25.3	2.8	1031
321710	WRA	Waimakariri at Cheeseman	2403600	5780000	880	34.0	6/1990	1/2001	10.5	3.8	1373
H31181	CDB	Craigieburn Stn	2417631	5788936	610	32.9	1/1971	6/1972	1.4	2.7	991
H31251	CDB	Simois Creek	2392096	5768430	549	31.4	1/1971	12/1987	17.0	2.5	918
H31252	CDB	Glenthorne Lower Station	2391785	5767647	564	31.0	9/1985	12/2000	15.3	2.6	947
H31271	CDB	Castle Hill	2405607	5776651	715	30.1	1/1971	12/2000	28.1	2.7	972
311910	WRA	Waimakariri at Esk rain	2425700	5787100	400	26.6	5/1990	1/2001	9.8	2.8	1021
H31351	CDB	L Coleridge Homestead	2395463	5761377	514	23.7	1/1971	12/2000	30.0	2.4	868
314710	WRA	Rakaia at Dry Acheron	2401771	5755618	655	15.4	6/1985	1/2001	15.6	3.2	1165
322110	WRA	Ashley at Townshend	2434180	5779062	470	15.1	2/1976	1/2001	24.5	3.7	1357
H31391	CDB	Mt Torlesse	2422902	5765118	378	10.6	1/1971	11/1996	25.4	2.8	1020
313710	WRA	Selwyn at 13 Mile Bush	2411990	5756899	488	10.4	6/1973	1/2001	24.1	3.5	1262
H31471	CDB	High Peak Station	2407472	5750125	457	7.6	1/1971	11/2000	29.3	3.3	1196
314701	WRA	Selwyn at High Peak	2407629	5750237	457	7.6	12/1987	1/2001	13.1	2.7	982
H32301	CDB	View Hill	2431636	5767447	335	7.3	1/1971	5/1979	8.3	3.0	1107
H31382	CDB	Dalethorpe	2418786	5757509	396	6.8	1/1971	12/1980	9.9	3.3	1206
H31482	CDB	Steventon	2416889	5754039		5.2	1/1971	12/1976	5.0	1.9	701
322210	WRA	Ashley at Ashley Gorge No 1	2446168	5773516	247	3.6	1/1971	1/1988	15.2	3.2	1177
H31472	CDB	Windwhistle,Rockwood	2410276	5746611	366	3.1	1/1971	10/1973	2.5	2.7	983
H31571	CDB	Waverley	2407078	5744119	381	3.0	1/1971	12/1984	5.8	2.8	1010
H32213	CDB	Glentui 2	2444191	5769802	274	1.8	2/1984	12/1998	14.9	2.7	991
H32222	CDB	Oxford	2444515	5769917	259	1.7	1/1971	3/1973	2.2	2.3	843
H3148B	CDB	Glendore	2415589	5748465	360	1.4	1/1972	12/1976	3.0	2.6	954
324110	WRA	Waimakariri at Waimakariri Gorge	2433142	5760479	260	0.8	12/1987	1/2001	12.4	2.1	763

Table A.1 (continued)

Network/ Site No.	Archive	Station Name	Easting (NZMG)	Northing (NZMG)	Elevation (m a.s.l.)	NW Dist (km)	Begin Date	End Date	Obs. Years	$\bar{p}$ Daily (mm dy^{-1})	$\bar{p}$ Annual (mm a^{-1})
H31592	CDB	Woodlands	2409210	5742151	366	0.1	1/1971	12/1991	15.0	3.0	1079
H32311	CDB	Oxford 2	2444217	5767136	232	-0.4	4/1973	1/1984	10.8	2.7	978
H32312	CDB	Oxford, Matai	2444243	5767028	237	-0.5	6/1995	12/2000	5.6	2.4	886
315910	WRA	Selwyn at Whitecliffs rain	2420369	5748637	280	-1.2	5/1988	1/2001	12.6	2.6	947
H31581	CDB	Hororata West	2417613	5741154	287	-5.7	1/1971	12/2000	30.0	2.5	919
H32402	CDB	Homebush	2428443	5747710	244	-6.8	1/1971	12/2000	26.9	2.4	888
H31591	CDB	Hororata	2420964	5739760	213	-8.8	1/1971	12/2000	30.0	2.4	866
H31594	CDB	Hororata, Illana	2424831	5741786	196	-9.4	9/1994	12/2000	6.3	2.2	789
H31593	CDB	Hororata Substation	2427673	5739734	192	-12.7	1/1971	9/1993	21.0	2.2	799
H32424	CDB	Eyrewell Forest	2451530	5756649	158	-13.2	1/1971	12/1989	19.0	2.1	776
H32412	CDB	Darfield	2440217	5745875	195	-15.2	1/1971	12/2000	30.0	2.2	798
H32416	CDB	Darfield Ews	2441272	5745553	190	-16.1	8/1999	12/2000	1.4	2.0	717
H32415	CDB	Darfield Forest Plns	2441114	5745218	184	-16.3	4/1989	12/1997	8.8	2.2	803

Table A.2 Rain gauges in the southwest Hokitika transect of the Southern Alps from 1 Jan 1971 to 31 Dec 2000. Total number of gauges: 54; CliDB gauges: 35; WRA gauges: 19. Column headers as per Table A.1.

Network/ Site No.	Archive	Station Name	Easting (NZMG)	Northing (NZMG)	Elevation (m a.s.l.)	NW Dist (km)	Begin Date	End Date	Obs. Years	$\bar{p}$ Daily (mm dy^{-1})	$\bar{p}$ Annual (mm a^{-1})
F20981	CDB	Ross	2331072	5810548	15	101.5	1/1971	12/2000	30.0	8.9	3267
F30061	CDB	Pukekura	2320171	5797028	86	97.0	11/1982	5/1995	12.5	9.5	3458
F20892	CDB	Kowhitirangi Fairhave	2344564	5813556	30	95.9	1/1971	12/2000	30.0	9.2	3368
F21802	CDB	Kokatahi	2349729	5816346	24	95.1	6/1980	6/1999	18.9	9.4	3419
F21801	CDB	Kowhitirangi No 2	2349262	5811890	30	91.8	1/1971	12/2000	30.0	9.4	3448
F30071	CDB	Waitaha Valley	2325390	5791059	70	89.1	1/1971	7/1971	0.6	6.2	2251
301710	WRA	Waitaha at Fergusons Farm	2325700	5790375	90	88.3	11/1976	1/1984	6.3	13.2	4818
209910	WRA	Hokitika at Colliers Ck rain	2346500	5800100	95	83.9	11/1987	1/2001	12.2	20.8	7591
310010	WRA	Hokitika at Rapid Ck	2348160	5797546	152	80.9	1/1971	1/2001	28.4	21.1	7698
301910	WRA	Tuke at Tuke Hut	2338166	5788770	975	79.7	5/1977	1/2001	23.5	29.1	10625
301810	WRA	Waitaha at MoonBeam Torrent	2331412	5782978	410	79.0	6/1977	4/1982	3.6	18.0	6569
311015	WRA	Cropp at Waterfall	2342803	5790316	975	78.2	6/1982	1/2001	17.5	32.4	11825
301913	WRA	Cropp at Cropp Hut	2344271	5790069	860	77.1	7/1981	1/2001	21.0	29.8	10895
311010	WRA	Hokitika at Prices Flat	2347983	5787026	427	72.5	4/1971	1/2001	27.9	20.4	7446
303911	WRA	Rakaia at Lake Ramsay	2341113	5767332	945	60.6	7/1977	1/2001	22.1	13.2	4817
312110	WRA	Mathias at NZDSA Hut	2358196	5778522	670	59.6	5/1978	1/2001	22.4	12.5	4559
312111	WRA	Talus at Talus Tarn rain	2353640	5772495	1670	57.4	5/1979	9/1986	5.1	8.3	3032
313210	WRA	Rakaia at Glenfalloch	2365795	5762746	610	42.4	3/1977	10/1982	5.6	4.4	1604
H31321	CDB	Double Hill	2369930	5764675	561	41.5	1/1971	12/2000	30.0	3.7	1334
H31331	CDB	Glenariffe	2378037	5765060	457	37.0	1/1971	10/1988	14.4	2.4	860
H3141A	CDB	Upper Lake Heron	2363261	5750421	686	33.9	1/1971	5/1981	10.3	2.7	993
H31341	CDB	Peak Hill	2384208	5764844	411	33.2	1/1971	12/1985	14.7	2.3	828
314412	WRA	Ashburton at Turtons Saddle rain	2377500	5759800	1140	33.1	11/1994	1/2001	6.1	2.7	1003
315010	WRA	Sth Ashburton at Boundary Creek	2353409	5741002	1120	32.1	12/1999	1/2001	1.1	3.8	1386
H31352	CDB	Lake Coleridge	2390795	5759407	364	24.9	1/1971	12/2000	28.5	2.2	820
H31611	CDB	Hakatere Stn	2361886	5731944	616	19.8	1/1971	10/1982	10.9	2.4	880
H31612	CDB	Hakatere	2362215	5731729	604	19.5	12/1984	10/1991	5.4	1.6	598
314411	WRA	Nth Ashburton at Cookies Hut	2383388	5744625	1000	17.4	12/1999	1/2001	1.0	3.2	1180
H31451	CDB	Mt Hutt Skifield	2391688	5745423	1600	13.1	8/1989	10/1993	0.5	1.7	615
H31621	CDB	Mt Possession	2367168	5726613	610	12.4	1/1971	11/1980	8.3	2.4	874
316310	WRA	Sth Ashburton at Mt Somers rain	2373675	5731337	807	12.4	2/1988	1/2001	12.6	2.8	1017
H31461	CDB	Bayfields	2399907	5747451	497	9.9	1/1971	7/1979	8.6	3.3	1222
315510	WRA	Pudding Hill Stm at Mt Hutt	2391622	5740256	1066	9.0	2/1988	1/2001	12.3	4.6	1678
H31463	CDB	Snowdon Ews	2402568	5747938	560	8.7	6/1999	12/2000	1.5	3.5	1282
315610	WRA	Rakaia at Fighting Hill rain	2399699	5743693	290	7.0	4/1988	8/2000	11.9	2.5	913
317210	WRA	Rangitata at Klondyke	2366600	5714900	400	3.3	6/1991	1/2001	9.5	2.7	971
H31733	CDB	Evandale	2376411	5721768	396	3.0	1/1971	12/2000	29.5	2.7	1004

Table A.2 (continued)

Network/ Site No.	Archive	Station Name	Easting (NZMG)	Northing (NZMG)	Elevation (m a.s.l.)	NW Dist (km)	Begin Date	End Date	Obs. Years	$\bar{p}$ Daily (mm dy^{-1})	$\bar{p}$ Annual (mm a^{-1})
H31642	CDB	Staveley, Birchlands	2385096	5727898	382	2.8	1/1971	12/2000	29.9	3.3	1220
H31721	CDB	Mayfield, Temora	2369416	5715751	468	2.3	5/1983	12/2000	17.6	2.6	953
H31641	CDB	Mt Somers, Somer Downs	2382045	5724912	372	2.2	4/2000	12/2000	0.8	3.6	1312
H31655	CDB	Methven,Alaska	2394016	5732351	402	1.2	1/1971	12/2000	30.0	3.2	1155
H31651	CDB	Alford Forest 1	2391162	5729301	390	0.4	1/1971	12/2000	29.6	3.0	1078
H31736	CDB	Mt Somers	2381146	5721339	383	-0.1	12/1980	12/2000	20.1	2.6	933
H31742	CDB	Mt Somers,Motels	2381002	5720447	366	-0.7	1/1971	7/1991	16.8	2.5	918
H31734	CDB	Mayfield,Brackley	2373886	5713640	396	-2.0	1/1971	4/1979	7.9	2.8	1024
H31643	CDB	Springburn	2387752	5723258	312	-2.5	1/1971	12/2000	30.0	2.5	915
H31572	CDB	Highbank Power Stn	2407922	5736354	230	-3.8	1/1971	12/2000	30.0	2.6	932
H31661	CDB	Methven	2400961	5729143	332	-5.5	1/1971	12/2000	30.0	2.6	956
H31743	CDB	Mt Somers,Buccleugh	2387490	5718235	296	-6.4	1/1971	9/1992	21.7	2.3	847
H31671	CDB	Rakaia, Greenfields	2407705	5732621	305	-6.7	1/1971	12/2000	30.0	2.4	894
H31771	CDB	Lyndhurst Limewood Farm	2406606	5722111	243	-14.5	1/1971	12/2000	30.0	2.1	781
H31681	CDB	Creeside	2415498	5726131	226	-16.5	1/1971	6/1983	12.5	2.3	825
H31851	CDB	Hackthorne	2395671	5710934	198	-17.1	1/1971	8/1998	26.8	2.1	758
H31943	CDB	Lismore,Midway	2383078	5700151	213	-18.3	1/1971	12/1982	12.0	2.2	800

Table A.3 Rain gauges in the Franz Josef transect of the Southern Alps from 1 Jan 1971 to 31 Dec 2000. Total gauges: 73; CliDB gauges: 51; WRA gauges: 22. Column headers as per Table A.1.

Network/ Site No.	Archive	Station Name	Easting (NZMG)	Northing (NZMG)	Elevation (m a.s.l.)	NW Dist (km)	Begin Date	End Date	Obs. Years	$\bar{p}$ Daily (mm dy^{-1})	$\bar{p}$ Annual (mm a^{-1})
F30212	CDB	Okarito	2279752	5772503	2	101.1	10/1981	12/2000	19.3	9.1	3323
F39481	CDB	Gillespies Beach	2252621	5749771	6	98.7	1/1971	6/1971	0.5	5.8	2108
301510	WRA	Poerua at Lower Gorge rain	2303838	5785590		97.4	3/1989	6/1990	1.2	10.0	3650
F30231	CDB	Lower Whataroa	2296539	5775540	30	93.6	1/1971	12/2000	30.0	10.4	3797
F39664	CDB	Bruce Bay Pt	2234722	5727710	5	91.5	1/1981	5/1986	4.4	12.5	4557
F30153	CDB	Harihari N.Z.F.S.	2310984	5782093	45	90.4	1/1971	2/1987	16.2	10.5	3848
F30152	CDB	Harihari M.W.D.	2311417	5781217	49	89.4	1/1971	7/1982	10.9	10.4	3797
F30233	CDB	Whataroa 2	2295877	5768183	64	88.1	1/1971	7/1999	26.7	12.5	4581
F30311	CDB	Franz Josef T.H.C.	2281374	5755034	122	86.0	1/1971	9/1983	12.7	13.4	4907
F30402	CDB	Fox Glacier,Main Rd	2268681	5744919	152	85.3	1/1971	2/1994	23.2	12.8	4669
F30401	CDB	Fox Glacier M.W.D.	2268689	5744697	91	85.2	1/1971	1/1987	15.1	12.7	4628
F30312	CDB	Franz Josef	2281674	5753377	155	84.5	1/1982	11/2000	18.4	16.1	5894
303411	WRA	Whataroa at SHB rain	2300007	5764762	90	82.9	6/1989	1/2001	10.9	14.7	5383
304110	WRA	Waiho at Alex Knob	2279436	5749303	1295	82.5	7/1991	12/1995	3.8	21.4	7799
304210	WRA	Waiho at Douglas Hut	2280888	5749969	250	82.2	12/1983	1/2001	12.3	18.7	6839
305210	WRA	Waiho at Luncheon Rock	2281800	5746100	680	78.5	8/1982	12/1986	3.7	27.9	10176
304211	WRA	Waiho at Almer Hut	2284283	5744269	1735	75.6	7/1991	2/1996	4.5	15.6	5692
304410	WRA	Godley at Panorama Ridge	2306330	5743752	1509	62.2	12/1993	1/2001	7.0	16.9	6164
305411	WRA	Godley at Eade Hut	2306490	5739915	975	59.0	12/1993	1/2001	7.1	15.3	5596
H30711	CDB	Mt Cook,The Hermitage	2275869	5715378	765	57.3	1/1971	2/2000	29.2	11.7	4290
307001	WRA	Hooker at Mt Cook(The Hermitage)	2276100	5715400	752	57.1	11/1989	1/2001	10.8	12.1	4431
H30706	CDB	Mt Cook Ews	2276118	5715164	765	56.9	3/2000	12/2000	0.8	13.9	5092
304610	WRA	Rangitata at Mistake Flat	2323437	5748450	790	55.9	3/1982	1/2001	14.3	10.9	3999
307110	WRA	Hooker at Ball Hut Rd Br rain	2278700	5714600	680	55.0	12/1993	1/2001	7.0	8.4	3080
H30811	CDB	Sealey Village	2278056	5708117	640	50.1	1/1971	4/1972	1.3	4.8	1749
H30581	CDB	Erewhon	2336583	5742343	594	43.2	1/1971	11/1996	25.9	4.3	1573
308217	WRA	Jollie at Jollie Hut	2284763	5702398	610	41.5	8/1972	12/1999	27.2	3.6	1307
H30751	CDB	Lilybank Station	2313388	5719475	686	38.4	1/1971	9/1992	21.7	3.0	1097
306610	WRA	Macaulay at Mt Gerald	2318100	5721900	823	37.6	7/1990	1/2001	10.3	3.1	1138
H30912	CDB	The Rest	2279670	5691719	515	35.9	1/1971	3/1976	5.2	3.1	1128
H30921	CDB	L Pukaki, Braemar	2285279	5687353	550	29.1	1/1971	12/2000	29.6	2.4	860
H30691	CDB	Mesopotamia	2340148	5727258	552	28.9	1/1971	12/2000	27.9	2.6	955
H30841	CDB	Godley Peaks, Tekapo	2306829	5701828	762	28.0	1/1971	4/1976	4.9	1.8	646
H40021	CDB	L Pukaki Tasman Downs	2285289	5684685	564	26.9	1/1973	12/2000	27.8	2.4	879
309211	WRA	Mary Burn at Coach Rd	2291504	5688529	838	26.4	9/1974	10/1994	19.8	2.3	832
H40022	CDB	L Pukaki, Guide Hill	2289262	5685818	745	25.5	1/1971	12/2000	30.0	2.4	876
308610	WRA	Coal Ck at Skifield	2321453	5706258	1364	23.0	11/1989	1/1997	7.1	2.4	880

Table A.3 (continued)

Network/ Site No.	Archive	Station Name	Easting (NZMG)	Northing (NZMG)	Elevation (m a.s.l.)	NW Dist (km)	Begin Date	End Date	Obs. Years	$\bar{p}$ Daily (mm dy^{-1})	$\bar{p}$ Annual (mm a^{-1})
H30941	CDB	Mt John	2306600	5688260	1027	17.2	1/1971	12/1987	17.0	1.6	588
H40041	CDB	Lake Tekapo, Air Safaris	2304806	5686537	762	16.9	1/1971	12/2000	30.0	1.6	600
H30951	CDB	L Tekapo,Mt Hay Stn	2312766	5690601	732	15.5	1/1973	12/2000	27.8	1.7	603
400410	WRA	Tekapo at Lake Tekapo	2307400	5686500	710	15.3	11/2000	1/2001	0.2	1.6	582
H31702	CDB	Rata Peaks	2353205	5719856	433	15.2	1/1971	12/1987	6.3	2.2	797
H40112	CDB	Lake Pukaki M.W.D.	2280725	5665851	556	14.4	1/1971	12/1984	14.0	1.8	653
H40031	CDB	Irishman Creek	2298003	5678431	664	14.4	11/1972	9/1976	3.4	1.7	603
H40111	CDB	Lake Pukaki No 1	2281238	5664869	506	13.3	1/1971	1/1972	1.1	1.4	509
H40121	CDB	Lake Pukaki East	2290538	5671519	634	13.2	1/1971	9/1972	1.7	1.3	478
H40132	CDB	The Wolds Station	2298666	5675229	610	11.4	1/1976	9/1983	5.7	1.6	586
309810	WRA	Opuha at Clayton	2337100	5701700	792	10.1	2/1988	1/2001	12.8	3.0	1101
H31711	CDB	White Rock	2361995	5716055	518	6.9	2/1971	9/1979	8.7	2.2	815
H30981	CDB	Deepburn	2336988	5695452	518	5.1	1/1971	12/2000	29.9	2.7	995
H31801	CDB	Lochaber	2354829	5705447	451	2.6	1/1971	8/1989	18.7	2.3	838
H40073	CDB	Cloudy Peaks	2326618	5684061	457	2.0	1/1971	9/1971	0.7	3.0	1102
H40074	CDB	Kimbell	2327911	5683651	427	0.9	10/1971	12/2000	29.3	3.0	1083
H40151	CDB	Burkes Pass,Glenrock	2313362	5672765	594	0.7	9/1976	12/2000	23.6	1.6	583
H40061	CDB	Burkes Pass,Airies	2323912	5680429	518	0.7	1/1971	12/2000	30.0	2.5	909
400710	WRA	Opihi at Kimbell	2327551	5682318	472	0.1	2/1988	1/2001	12.6	2.3	857
H31823	CDB	Mt Peel,Waikari Hills	2367664	5710843	396	-0.6	5/1975	7/1984	8.4	2.5	924
H31822	CDB	Mt Peel	2368887	5706202	305	-5.1	1/1971	4/1993	21.8	2.8	1016
H40321	CDB	Haldon Station	2291921	5646551	399	-7.8	3/1972	10/1976	2.6	1.1	407
419211	WRA	Orari at Mt Frances	2362678	5696939	640	-8.9	3/1988	1/2001	12.4	2.7	985
H40185	CDB	Fairlie	2335908	5676237	300	-9.8	11/1992	12/2000	6.7	2.3	842
H40182	CDB	Fairlie	2335810	5675971	306	-9.9	1/1971	7/1978	7.6	1.9	710
H40183	CDB	Fairlie,Riverview Tce	2336518	5676434	304	-10.0	8/1978	5/1990	11.8	1.9	682
H40331	CDB	Grays Hills Stn	2301138	5650184	479	-10.3	10/1976	5/1997	20.7	1.3	459
319211	WRA	Kowhai Stm at Blandswood	2367900	5699000	300	-10.3	12/1992	1/2001	7.9	3.7	1362
401610	WRA	Tengawai at Mackenzie Pass	2324000	5666500	690	-10.6	6/2000	1/2001	0.5	2.9	1047
H31927	CDB	Peel Forest	2370162	5698650	286	-11.9	1/1971	12/2000	30.0	2.8	1034
H31835	CDB	Ruapuna	2373998	5701155	283	-12.2	2/1986	12/2000	14.9	2.7	984
H31921	CDB	Peel Forest,Scotsburn	2367814	5696177	335	-12.5	1/1971	3/1983	11.7	3.5	1265
410010	WRA	Opuha at Geraldine Forest	2350800	5681088	792	-14.7	7/1985	1/2001	13.7	2.7	977
H31926	CDB	Orari Gorge	2365275	5691011	259	-15.2	1/1971	12/2000	30.0	3.2	1177
H40272	CDB	Te Ngawai	2328700	5663555	427	-15.8	1/1971	12/2000	29.6	2.3	855
H41011	CDB	Woodbury	2362751	5687922	305	-16.2	1/1971	12/2000	30.0	3.0	1083

Table A.4 Rain gauges in the Haast transect of the Southern Alps from 1 Jan 1971 to 31 Dec 2000. Total number of gauges: 49; CliDB gauges: 39; WRA gauges: 10. Column headers as per Table A.1.

Network/ Site No.	Archive	Station Name	Easting (NZMG)	Northing (NZMG)	Elevation (m a.s.l.)	NW Dist (km)	Begin Date	End Date	Obs. Years	$\bar{p}$ Daily (mm dy^{-1})	$\bar{p}$ Annual (mm a^{-1})
F39721	CDB	Lake Moeraki	2209374	5714494	9	95.8	5/1985	12/2000	15.6	12.3	4502
F39803	CDB	Haast Aws	2189128	5697641	5	94.2	1/1982	12/2000	16.6	10.4	3798
F39801	CDB	Haast	2189213	5697533	4	94.0	1/1971	8/1976	5.7	9.0	3275
F38981	CDB	Okuru,Carters	2178286	5689097	6	93.7	3/1971	3/1971	0.1	7.9	2900
F39802	CDB	Haast Township	2191889	5695437	11	90.8	1/1981	12/1989	8.8	10.8	3927
F39741	CDB	Paringa	2225036	5716071	43	87.8	1/1971	12/2000	29.7	15.2	5534
F39662	CDB	Mahitahi	2235630	5723299	30	87.4	1/1971	12/2000	29.1	12.9	4707
399210	WRA	Haast at Cron Ck	2202129	5686188	58	77.3	12/1991	1/2001	9.0	22.6	8249
399213	WRA	Haast at Roaring Billy rain	2212857	5689490	60	73.6	3/1989	1/2001	10.8	15.8	5766
F39932	CDB	Haast,Macpherson Camp	2214584	5688033	76	71.4	2/1971	3/1980	2.3	11.6	4230
399410	WRA	Haast at Moa Ck	2221639	5684164	105	64.1	11/1991	1/2001	9.1	10.8	3957
F49132	CDB	Haast Pass	2218661	5672086	524	56.1	1/1971	11/1988	17.9	12.3	4489
399811	WRA	Hopkins at Elcho Flats	2255937	5693559	701	51.4	12/1993	1/2001	7.0	9.9	3611
I49224	CDB	Mt Albert Stn	2207635	5657353	320	50.7	5/1972	5/1973	1.1	6.6	2400
492203	WRA	Makaroa at Makaroa Telemetry	2208500	5655500	280	48.7	11/1997	1/2001	3.1	7.1	2586
I49222	CDB	Makarora Station	2208534	5655170	320	48.4	1/1971	12/2000	30.0	6.6	2427
399710	WRA	Hopkins at Boanerges Ridge	2252512	5685726	1402	47.1	12/1993	1/2001	7.0	9.7	3544
491610	WRA	Ahuriri at Cassinia Moraine	2243162	5671844	980	41.4	1/1971	1/2001	29.5	7.1	2601
I49411	CDB	Minaret Bay	2200127	5636759	313	38.5	1/1971	12/2000	28.2	4.1	1490
490810	WRA	Hopkins at Huxley Lodge	2257052	5677304	555	37.6	5/1988	10/1994	6.4	5.2	1900
H49182	CDB	Lake Ohau Stn	2255917	5666392	533	29.5	1/1971	12/2000	30.0	3.2	1182
I49432	CDB	Hunter Valley 2	2216075	5634933	360	27.7	1/1971	12/2000	16.6	3.2	1178
I49602	CDB	West Wanaka Station	2192661	5613151	300	23.9	7/1987	1/1990	2.6	2.6	957
I4928A	CDB	Ahuriri Catchment	2255848	5657272	914	22.2	1/1971	7/1972	1.6	2.9	1051
I49621	CDB	Lake Hawea	2211714	5615160	350	14.3	1/1971	12/2000	29.2	2.2	798
494611	WRA	Ahuriri at Plains	2245132	5638418	747	13.3	9/1971	11/1994	23.0	2.5	907
I49613	CDB	Wanaka, Park Hq	2204301	5605474	305	10.8	9/1990	1/1994	3.4	1.8	648
I49381	CDB	Ribbonwood	2258028	5644123	634	10.3	1/1971	12/2000	27.0	2.3	834
H40211	CDB	Twizel	2277792	5658189	457	10.0	2/1972	5/1986	14.3	1.8	643
I49612	CDB	Albert Town	2208035	5607094	293	9.9	1/1971	8/1972	1.6	1.8	659
I49711	CDB	Wanaka	2204664	5604490	314	9.8	1/1971	8/1990	19.7	1.9	703
I49631	CDB	Hawea Flat	2217018	5612063	335	8.6	1/1971	12/2000	30.0	2.0	733
H40213	CDB	Twizel	2278729	5656554	457	8.1	6/1989	12/2000	10.8	1.7	633
H40212	CDB	Twizel Substation	2278381	5655097	451	7.1	4/1985	6/1993	8.2	1.6	573
I49712	CDB	Mt Barker	2207676	5602850	305	6.7	1/1971	9/2000	29.7	1.9	678
494711	WRA	Ahuriri at Sth Diadem rain	2249600	5632100	610	5.6	11/1992	1/2001	8.0	2.3	851
I49723	CDB	Wanaka Aero Aws	2212519	5602739	352	3.8	4/1992	12/2000	8.6	1.8	670

<div align="center">**Table A.4** (continued)</div>

Network/ Site No.	Archive	Station Name	Easting (NZMG)	Northing (NZMG)	Elevation (m a.s.l.)	NW Dist (km)	Begin Date	End Date	Obs. Years	$\bar{p}$ Daily (mm dy^{-1})	$\bar{p}$ Annual (mm a^{-1})
I49721	CDB	Luggate	2214631	5601611	295	1.6	1/1971	12/2000	24.3	1.7	614
I49651	CDB	Morven Hills	2232725	5612413	442	-0.4	1/1971	8/1996	21.9	2.0	714
I40401	CDB	Chain Hills	2271647	5633621	400	-6.2	1/1993	12/2000	8.0	1.3	477
I49592	CDB	Tara Hills Aws	2262833	5626625	488	-6.7	5/1985	12/2000	14.9	1.4	529
I49591	CDB	Omarama,Tara Hills	2262678	5626508	488	-6.7	1/1971	12/1985	15.0	1.5	534
I4975A	CDB	Geordie Hill	2235205	5606289	455	-6.8	5/1987	1/1990	2.3	1.5	559
I49822	CDB	Queensbury Ews	2217692	5586399	277	-12.5	11/1978	5/1992	13.6	1.8	652
H40421	CDB	Black Forest Stn	2291272	5639638	366	-13.0	11/1973	1/1990	10.7	1.3	462
I49841	CDB	Tarras	2227530	5591170	290	-14.4	1/1971	7/1986	15.4	1.3	487
I49931	CDB	Bendigo 1	2219014	5583343	202	-15.7	1/1971	6/1979	8.5	1.2	440
I49932	CDB	Bendigo 2	2218290	5579694	200	-18.2	5/1978	5/1992	14.1	1.1	416
I40501	CDB	Otamatapaio	2277769	5622610	411	-18.7	1/1971	1/1986	13.0	1.4	501

Table A.5 Rain gauges in the Milford transect of the Southern Alps from 1 Jan 1971 to 31 Dec 2000. Total number of gauges: 46; CliDB gauges: 38; WRA gauges: 8. Column headers as per Table A.1.

Network/ Site No.	Archive	Station Name	Easting (NZMG)	Northing (NZMG)	Elevation (m a.s.l.)	NW Dist (km)	Begin Date	End Date	Obs. Years	$\bar{p}$ Daily (mm dy^{-1})	$\bar{p}$ Annual (mm a^{-1})
F48301	CDB	Martins Bay	2111801	5635326		89.6	2/1971	11/1974	2.4	9.5	3471
F48302	CDB	Lake Mckerrow	2113817	5635003	6	88.1	3/1982	3/1984	1.1	14.7	5380
F48331	CDB	Big Bay,Pyke River	2136812	5640473	328	78.9	2/1971	4/1971	0.2	11.3	4128
F47691	CDB	Milford Sound	2107601	5602699	3	65.7	1/1971	12/2000	30.0	18.3	6699
F47693	CDB	Milford Sound Aws	2107695	5602341	3	65.4	7/2000	12/2000	0.4	18.3	6696
F47771	CDB	Dumpling Hut	2095771	5591235	120	63.4	1/1982	3/1987	1.7	31.4	11465
F48611	CDB	Hidden Falls Hut	2122830	5608269	50	61.2	4/1982	1/1986	1.4	17.6	6439
F47872	CDB	Mackinnon Pass	2096715	5587620	1150	60.0	12/1987	1/1988	0.2	15.3	5576
F47871	CDB	Lake Mintaro Hut	2097331	5586658	640	58.8	1/1982	2/1993	2.1	23.9	8718
477911	WRA	Cleddau at No 3A	2110191	5594696	457	57.7	1/1971	9/1994	11.5	16.7	6095
F47794	CDB	Homer Tunnel Western	2112322	5592939	823	55.0	11/1984	11/1988	4.0	14.1	5142
F47791	CDB	Homer Tunnel, Eastern	2113909	5592925	884	54.1	11/1984	11/1988	3.7	17.9	6552
I48711	CDB	Routeburn Falls Hut	2129797	5597582	914	48.7	12/1971	4/1973	0.9	11.4	4147
F47881	CDB	Clinton Forks Hut	2105968	5579074	250	47.6	1/1982	1/1993	2.7	13.2	4810
I48712	CDB	Lake Mckenzie Hut	2127594	5593523	914	46.5	3/1971	4/1973	1.1	11.0	4004
I48713	CDB	Lake Mckenzie Hut	2128081	5593328	910	46.1	12/1981	4/1990	3.8	15.6	5682
I48811	CDB	Lake Howden Hut	2125315	5587822	690	43.2	12/1981	5/1991	5.9	13.8	5032
I48581	CDB	Glenfinnan	2179130	5626166	341	42.4	1/1971	12/2000	30.0	5.8	2100
I48731	CDB	Routeburn Stn	2139104	5596082	381	41.8	3/1971	12/2000	27.3	6.2	2276
487302	WRA	Dart at "The Hillocks, Gelnorchy"	2140100	5593300	310	38.9	8/1997	1/2001	3.2	5.2	1899
I48741	CDB	Earnslaw	2146092	5595920	335	37.5	1/1971	12/2000	29.8	4.3	1575
486610	WRA	Shotover at 16 Mile rain	2165081	5606458	610	34.8	2/1977	4/1986	8.3	4.0	1467
I48833	CDB	Rees Valley Station	2145922	5590457	464	33.2	9/1987	1/1990	2.3	4.3	1559
I48901	CDB	Knobs Flat	2117333	5569197	375	32.9	1/1971	11/1988	17.3	6.4	2342
I48831	CDB	Glenorchy School	2145182	5585296	311	29.5	1/1971	5/1978	6.5	3.0	1085
I48771	CDB	Shotover Branches	2172205	5598440	503	24.1	6/1973	12/2000	27.6	2.8	1035
486920	WRA	Matutukituki at West Wanaka	2192000	5611400	280	22.9	1/1998	1/2001	2.9	3.0	1099
580110	WRA	Mararoa at Mavora Lakes	2124600	5557900	1433	19.5	3/1997	1/2001	3.8	4.2	1527
488701	WRA	Shotover at Peat's Hut	2171200	5588500	460	16.7	12/1996	1/2001	3.7	2.6	961
I48961	CDB	Arthurs Point	2168430	5570758	607	4.0	1/1971	12/2000	30.0	2.6	950
I4897A	CDB	Hunter Heights	2175738	5574477	488	2.7	4/1987	9/1989	2.1	2.2	804
I48973	CDB	Arrowtown, Zelkova	2178428	5575950	413	2.3	4/1992	4/2000	8.0	2.4	892
I48981	CDB	Arrowtown	2180185	5577153	360	2.2	1/1971	1/1991	20.1	2.1	749
489710	WRA	Shotover at Middletons	2172199	5571035	355	2.0	5/1985	11/1995	10.4	2.3	838
I49801	CDB	Cardrona	2195575	5585703	518	0.0	1/1971	12/2000	29.7	1.8	672
I58061	CDB	Queenstown	2168377	5565748	329	-0.0	1/1971	12/2000	30.0	2.5	913
I58074	CDB	Queenstown Aero	2173968	5567487	349	-1.9	1/1971	8/1993	21.8	1.9	695

Table A.5 (continued)

Network/ Site No.	Archive	Station Name	Easting (NZMG)	Northing (NZMG)	Elevation (m a.s.l.)	NW Dist (km)	Begin Date	End Date	Obs. Years	$\bar{p}$ Daily (mm dy^{-1})	$\bar{p}$ Annual (mm a^{-1})
I58075	CDB	Queenstown Aero Aws	2174125	5567495	354	-2.0	1/1982	12/2000	17.9	2.2	791
I58073	CDB	Kawarau Falls	2173536	5566686	320	-2.3	1/1971	2/1982	10.9	2.0	721
I58161	CDB	Cecil Peak	2163795	5558494	351	-3.2	1/1971	2/1979	5.5	2.0	725
I58311	CDB	Mavora Lakes Park	2131768	5530650	640	-6.7	11/1985	3/1989	3.4	4.0	1451
582210	WRA	Oreti at Gorge Ck	2138563	5535079	670	-7.1	10/1974	1/2001	26.2	3.2	1153
I49901	CDB	Upper Meg Power Stn	2199264	5573086	518	-12.3	1/1971	12/2000	29.8	2.1	770
I58091	CDB	Gibbston,Loop Rd	2191135	5566573	533	-12.8	1/1971	12/1984	14.0	1.8	666
I58171	CDB	Wye Creek	2176509	5554933	335	-13.5	1/1971	3/1981	9.8	2.0	715
I58092	CDB	Gibbston Nevis Bluff	2193265	5566566	366	-14.0	11/1984	5/1987	2.6	1.7	611

Appendix B

Simulated precipitation versus rain gauges

This appendix lists comparisons between precipitation simulated by the HadRM3P regional climate model and observations from rain gauges in the Southern Alps. Table B.1 lists comparisons during the 30-year period from 1 January 1971 to 31 December 2000, as described in Section 5.4. Table B.2 lists comparisons during the single day of 5 November 1994, as described in Section 5.5.

Table B.1   Observations from 28 long-term rain gauges in the Southern Alps, compared with precipitation simulated by HadRM3P, from 1 Jan 1971 to 31 Dec 2000. 'Period' is the number of years of observation at each rain gauge. 'Precip.' is the amount of observed or simulated mean annual precipitation. 'Diff.' is the simulated precipitation minus the observed precipitation. Rain gauges are listed in descending order of the absolute difference between observations and $\mathrm{Surf_{Rcm.A.Raw}}$.

Network/ Site No.	Station Name	Elevation (m a.s.l.)	Observed		$\mathrm{Surf_{Rcm.A.Raw}}$		$\mathrm{Surf_{Rcm.A.DsT}}$		$\mathrm{Surf_{Rcm.A.Ds}}$	
			Period (Years)	Precip. (mm a^{-1})	Precip. (mm a^{-1})	Diff. (mm a^{-1})	Precip. (mm a^{-1})	Diff. (mm a^{-1})	Precip. (mm a^{-1})	Diff. (mm a^{-1})
F30231	Lower Whataroa	30	30.0	3797	9504	5707	7947	4150	6320	2523
F30233	Whataroa 2	64	26.7	4581	9504	4923	7088	2507	6046	1465
F39662	Mahitahi	30	29.1	4707	8570	3863	7174	2467	6356	1649
F30401	Fox Glacier M.W.D.	91	15.1	4628	8133	3504	7815	3186	6682	2054
F30402	Fox Glacier,Main Rd	152	23.2	4669	8133	3464	7789	3121	6644	1975
F39741	Paringa	43	29.7	5534	8570	3036	5998	464	5731	196
H30711	Mt Cook,The Hermitage	765	29.2	4290	6781	2492	4862	572	5101	812
F30312	Franz Josef	155	18.4	5894	8133	2238	7004	1110	6406	512
H30581	Erewhon	594	25.9	1573	3786	2213	2507	934	2414	841
H30751	Lilybank Station	686	21.7	1097	2930	1834	1861	764	2028	931
F39803	Haast Aws	5	16.6	3798	5418	1620	4649	851	4556	758
F39721	Lake Moeraki	9	15.6	4502	3113	-1389	3858	-644	4085	-417
F30212	Okarito	2	19.3	3323	2363	-961	4518	1194	4613	1290
F49132	Haast Pass	524	17.9	4489	5356	867	5540	1051	5247	758
H49182	Lake Ohau Stn	533	30.0	1182	432	-750	1480	298	1952	770
308217	Jollie at Jollie Hut	610	27.2	1307	653	-654	2215	908	2572	1265
491610	Ahuriri at Cassinia Moraine	980	29.5	2601	3127	526	3389	788	3501	900
I49381	Ribbonwood	634	27.0	834	317	-517	629	-206	946	112
494611	Ahuriri at Plains	747	23.0	907	1143	236	1033	126	1204	297
H40021	L Pukaki Tasman Downs	564	27.8	879	653	-225	985	107	1387	509
H40022	L Pukaki, Guide Hill	745	30.0	876	653	-223	879	3	1286	410
I49591	Omarama,Tara Hills	488	15.0	534	317	-217	412	-121	550	16

Network/ Site No.	Station Name	Elevation (m a.s.l.)	Observed		Surf_{Rcm.Raw}		Surf_{Rcm.A.DsT}		Surf_{Rcm.A.Ds}	
			Period (years)	Precip. (mm a^{-1})	Precip. (mm a^{-1})	Diff. (mm a^{-1})	Precip. (mm a^{-1})	Diff. (mm a^{-1})	Precip. (mm a^{-1})	Diff. (mm a^{-1})
H30921	L Pukaki, Braemar	550	29.6	860	653	-207	1086	226	1468	607
309211	Mary Burn at Coach Rd	838	19.8	832	653	-178	880	48	1282	450
H30941	Mt John	1027	17.0	588	653	65	650	62	816	228
H30691	Mesopotamia	552	27.9	955	1011	57	1331	376	1463	508
H40041	Lake Tekapo, Air Safaris	762	30.0	600	653	53	608	8	781	181
H30951	L Tekapo,Mt Hay Stn	732	27.8	603	653	51	717	115	815	212

Table B.2 Observations from 19 rain gauges in the Southern Alps, compared with precipitation simulated by HadRM3P, on 5 Nov 1994 UTC. $\text{Surf}_{\text{Rcm.D.Raw}}$ is simulated precipitation at 30-km resolution; $\text{Surf}_{\text{Rcm.D.Ds}}$ is downscaled with the $\text{Surf}_{\text{Obs.D}}$ surface of observed mean daily precipitation; $\text{Surf}_{\text{Rcm.D.Ds.NW}}$ is downscaled with the $\text{Surf}_{\text{Obs.D.NW}}$ surface of observed mean daily precipitation on northwesterly days. 'Precip.' is the amount of observed or simulated precipitation. 'Diff.' is the simulated precipitation minus the observed precipitation.

Network/ Site No.	Station Name	Elevation (m a.s.l.)	Observed Precip. (mm)	$\text{Surf}_{\text{Rcm.D.Raw}}$ Precip. (mm)	Diff. (mm)	$\text{Surf}_{\text{Rcm.D.Ds}}$ Precip. (mm)	Diff. (mm)	$\text{Surf}_{\text{Rcm.D.Ds.NW}}$ Precip. (mm)	Diff. (mm)
304410	Godley at Panorama Ridge	1509	11	209	199	151	141	153	143
303411	Whataroa at SHB rain	90	79	210	131	170	91	172	93
399410	Haast at Moa Ck	105	44	163	119	105	61	124	80
399811	Hopkins at Elcho Flats	701	177	71	-106	58	-118	67	-109
399210	Haast at Cron Ck	58	68	163	96	175	108	172	104
304210	Waiho at Douglas Hut	250	100	180	81	167	67	167	67
399213	Haast at Roaring Billy rain	60	89	163	74	146	57	151	62
307110	Hooker at Ball Hut Rd Br rain	680	89	158	69	91	2	91	1
308217	Jollie at Jollie Hut	610	54	1	-53	46	-8	48	-6
399710	Hopkins at Boanerges Ridge	1402	114	158	44	55	-59	61	-52
306610	Macaulay at Mt Gerald	823	57	16	-41	36	-21	39	-18
309810	Opuha at Clayton	792	26	0	-25	15	-10	14	-11
308610	Coal Ck at Skifield	1364	33	16	-17	23	-10	25	-8
304610	Rangitata at Mistake Flat	790	130	114	-16	108	-22	114	-16
307001	Hooker at Mt Cook(The Hermitage)	752	173	158	-15	114	-59	110	-63
304110	Waiho at Alex Knob	1295	170	180	10	160	-10	160	-10
305411	Godley at Eade Hut	975	219	209	-10	133	-86	137	-82
491610	Ahuriri at Cassinia Moraine	980	64	73	9	60	-4	63	-1
494711	Ahuriri at Sth Diadem rain	610	17	18	2	15	-1	18	2